

Characterization of *Arabidopsis* microtubule-associated proteins

Wong Jeh Haur

Nara Institute of Science and Technology

Graduate School of Biological Sciences

Plant Cell Function

Supervisor Takashi Hashimoto

Abstract

Plant microtubule (MT) is a cytoskeleton that plays critical roles in establishing proper cell division patterns and directional cell expansion that ultimately generate organ and plant morphology. This dynamic polymer alternates stochastic phases of polymerization and shrinkage, and in interphase plasma membrane-bound MTs migrate cell cortex and interact each other, which facilitates organization of distinct arrays. MT-associated proteins (MAPs) regulate stability, dynamics, organization, and interactions with other cellular components, and are important for versatile functions of various MT arrays. Although a few dozens of plant MAPs have been discovered by biochemical, genetic, and homology-based approaches, only a fraction of these MAPs have been characterized. In my work, I characterized two novel plant-specific MAP families that have been recently discovered by proteomic analyses of cytosolic proteins that co-purified with MTs from cell suspension cultures of *Arabidopsis thaliana*.

The BASIC PROLINE-RICH PROTEIN (BPP) family of plant-specific MAPs contains central highly basic regions, which in BPP1 was shown to be responsible for MT binding, and in *Arabidopsis* consists of seven members (BPP1 to BPP7). All seven BPP proteins fused to GFP were localized to cortical MTs. RT-PCR and promoter-GUS assays showed that, among the members, *BPP1* and *BPP5* are expressed mostly strongly and *BPP2* is expressed relatively highly in several vegetative and reproductive organs. When several single and multiple mutant combinations were analyzed, the *bpp1 bpp5* double mutant and the *bpp1 bpp2 bpp5* triple mutant showed distinct morphological defects that include shorter petioles, rounder leaves, shorter siliques, and overall stunted growth. In wild-type cotyledons and true leaves, pavement cells are highly inter-digitated and display complex jigsaw puzzle-like shapes. However, pavement cells in the double and triple *bpp* mutants do not develop into such complex shapes; in early stages of cell shape determination, local undulations of cell walls (lobe formation) is impaired. In wild-type cotyledon pavement cells, the lobe formation is facilitated by restricting growth at the convex side, with a presumed role of radiating MT bundles in this region. In the *bpp* mutants, these cortical MT bundles are not efficiently established. These studies indicate that BPP-family MAPs, especially BPP1 and BPP5, are required for the formation of transient MT arrays that radiate from the convex side of the developing lobes, and therefore for the formation of the jigsaw puzzle-like shapes of cotyledon pavement cells.

MAP55 (named after its molecular weight of approximately 55 kD) and its Arabidopsis homolog MAP55-Like (MAP55L) do not contain any functionally known motifs or domains. Gene expression studies by reverse transcription-PCR (RT-PCR) and promoter-driven GUS expression revealed that both members are highly expressed in all vegetative organs, except that *MAP55L* is hardly expressed in flowers and young siliques. When expressed as fusion proteins to green fluorescent protein (GFP) in Arabidopsis plants, both MAP55 and MAP55L were found localized to interphase cortical MTs and mitotic MT arrays, such as mitotic spindles. Transient expression studies in onion epidermal cells revealed multiple MT-binding regions at the C-terminal regions of these proteins. *In vitro* MT co-sedimentation assay with recombinant proteins showed that MAP55 and MAP55L bind MT directly. GFP-MAP55 particles tracked the growing plus ends of cortical MTs in Arabidopsis cells, independently of known MT plus-end tracking proteins, END-BINDING 1 (EB1) and SPIRAL1 (SPR1). *map55* null mutants were phenotypically indistinguishable from wild type, indicating functional redundancy with MAP55L or other MAPs.

Contents

Chapter 1: BPP family

1.1 Introduction.....	2
1.2 Materials and methods.....	5
1.3 Results.....	9
1.4 Discussion.....	53

Chapter 2: MAP55 and MAP55L

2.1 Introduction.....	56
2.2 Materials and methods.....	58
2.3 Results.....	60
2.4 Discussion.....	79
Conclusion.....	80
Acknowledgement.....	81
References.....	83

Chapter 1: BPP family

Introduction

In most eukaryotic cells, microtubules (MTs) are hollow cylinders composed of 13 protofilaments aligned in parallel and held tightly by lateral interactions (Ledbetter and Porter, 1964). The building blocks of protofilaments are the heterodimers of longitudinally stacked α - and β -tubulins (**Fig. 1A**). The MT end with α -tubulin exposed is termed the minus end while the end with β -tubulin exposed is the more dynamic plus end. When tubulin heterodimers are preferentially incorporated into the plus end, they interact with E-site GTP of the terminal β -tubulin subunit and trigger guanosine-5'-triphosphate (GTP) hydrolysis (Nogales *et al.*, 1998) (**Fig. 2A**). The plus end alternates between periods of growth and shrinkage with a net activity of polymerization, while the minus end undergoes slow depolymerization or static state. The plus end undergoes four kind of events: growth, shrinkage, catastrophe and rescue (Mitchison and Kirschner, 1984) (**Fig. 2B**). Catastrophe is the abrupt conversion from MT polymerization to shrinkage. On the other hand, rescue event occurs when the plus end stops depolymerization suddenly and switches back to the polymerization state. Dynamic instability of the plus end is widely explained by the GTP-cap model. In this model, occupation of GTP-tubulins at the plus end facilitates MT growth whereas GTP hydrolysis and stochastic dissociation of GTP-tubulin lead to the loss of the GTP-cap, causing rapid depolymerization (Mitchison and Kirschner, 1984). This dynamic instability enables different MT organization to occur in response to internal developmental and external environmental cues. In plant interphase cells, organized MTs called cortical MTs are spread in a quasi-2D sheet near the inner plasma membrane region (Hashimoto, 2003). According to the MT-microfibril alignment hypothesis for anisotropic growth of plant cells, these cortical MTs determine the orientation of microfibrils that provide major mechanical resistance in the cell wall for internal turgor pressure and external stresses (Baskin, 2001).

Cortical MTs not only display random (basket) and transverse arrays, but also show longitudinal and oblique arrays (Vineyard *et al.*, 2013). Dynamic rearrangement of cortical MT arrays is regulated either by MT-dependent nucleation angles with roughly 40° producing less transverse arrays or parallel angles with existing MTs generating MT bundles (Nakamura *et al.*, 2010) (**Fig. 3A**). Besides nucleation patterns, MT-MT interactions and KATANIN (KTN)-dependent MT

severing also work together to produce daughter MTs forming bundles or severed MTs at crossover sites (Hashimoto, 2015) (**Fig. 3B**).

Rearrangement of cortical MTs is crucial for post-mitotic plant cells to expand locally and in directional ways to attain final cell shapes (Guerriero *et al.*, 2014) (**Fig. 4A**). Two main types of cell expansion are the global and directional growth. Transverse cortical MT arrays promote diffuse anisotropic growth whereas random array ensures isotropic growth. Mixed growth that occurs in many pavement cells combines tip-growth and anisotropic growth. In the pavement cells of cotyledons and true leaves, anisotropic growth is required for the elongation of a whole cell along the growth axis of leaf blade. However, the cell margin is inter-digitated due to alternating tip-growth (localized cell expansion) at the concave lobe, and due to growth restriction at the convex lobes (**Fig. 4B**). This inter-digitation eventually gives rise to the jigsaw-puzzle-like pattern to both adaxial and abaxial surfaces of Arabidopsis cotyledons and true leaves. The complex inter-digitation pattern is regulated by specific MT arrays at certain regions of young pavement cells. Radiating MTs form at the regions that later shape into convex lobes. From the radiating MTs, continuous MT bands grow out to connect opposite convex lobes of the same cell, which subsequently restrict the cell expansion (Armour *et al.*, 2015; Fu *et al.*, 2002) (**Fig. 5**). The MT bands interconnect MTs at the interfacial surfaces, forming a circular structure around the convex lobe at the neck region. The radiating MTs and the transverse MT arrays only appear during early stages of pavement cell development during the lobe formation. When the pavement cells mature, cortical MTs rearrange to form more random patterns.

The dynamic rearrangement of cortical MT arrays in the convex lobe is regulated by the Rho-of-Plants (ROP) signaling pathway (Lin *et al.*, 2013) (**Fig. 6**). The rearrangement of cortical MTs into the transverse array perpendicular to the axis of cell elongation requires the activation of ROP-INTERACTIVE CRIB MOTIF-CONTAINING PROTEIN1 (RIC1) by the ROP6 (Fu *et al.*, 2009). At the indentation region of pavement cells, ROP6 binds to RIC1 through the CRIB motif (Fu *et al.*, 2005; Wu *et al.*, 2001). The ROP6 and RIC1 complex is activated by the perception of auxin, which may control MT-severing activity of KTN. KTN-dependent MT-detachment releases newly formed MT branches. This working model is generally adopted by the researchers, but potential

involvement of a putative auxin receptor, AUXIN-BINDING PROTEIN 1 (ABP1), in this ROP6-RIC1 pathway has been recently questioned (Gao *et al.*, 2015).

Several plant MAPs have been identified so far by using three different approaches: (1) bioinformatics search of animal or yeast MAP homologues based on conserved amino acid sequences; (2) forward genetic screening of mutants with altered anisotropic growth with or without MT-interacting drugs; and (3) co-purification with MTs from crude plant cell extracts (Gardiner and Marc, 2003; Ishida *et al.*, 2007; Hamada *et al.*, 2006). Dozens of plant MAPs were discovered using the third approach by repeated polymerization/ depolymerization cycles.

For my study, I worked on two classes of plant-specific MAPs that were initially identified by the third MT-co-purification approach from Arabidopsis suspension culture cell (Hamada *et al.*, 2013) (**Table 1**). The first class is the BASIC PROLINE-RICH PROTEINs (BPPs) family. The BPP family consists of seven members designated as BPP1 (At2g40070), BPP2 (At3g09000), BPP3 (At5g01280), BPP4 (At2g38160), BPP5 (At1g27850), BPP6 (At3g08670) and BPP7 (At3g51540) (Hamada *et al.*, 2013). Among them, only BPP1 has been partially characterized (Hamada *et al.*, 2013). BPP1 was found to be expressed in most plant tissues. BPP1-GFP expressed under its own promoter decorated cortical MTs in epidermal cells of leaves, hypocotyls and roots. Mitotic MT structures during cell division were also decorated. Transient expression of truncated BPP1 with only the basic domain bound to cortical MTs in onion epidermal cells, indicating the basic domain is responsible for the MT-binding. Stable overexpression of BPP1-GFP induced highly transverse cortical MT arrays in the leaf pavement cells and in the upper region of light-grown hypocotyls. Overexpression of BPP1-GFP increased stability of cortical MTs when challenged by a MT-disrupting drug, oryzalin. This indicates that BPP1 may function as a MT-stabilizing MAP. However, no obvious phenotypic defects were detected in three independent T-DNA insertional *bpp1* mutants. Therefore, it is unknown how BPP1-regulated MT organization is important to the plant normal development. Hence, my studies of the BPP family shall provide insights into the physiological importance of the BPP family proteins in ensuring proper organ development, particularly the shape determination of cotyledon pavement cells.

Materials and methods

Plant materials, growth conditions and plant transformation

Arabidopsis thaliana ecotype Columbia was used throughout the experiments. T-DNA insertion lines were obtained from The Arabidopsis Biological Resource Center (ABRC) for screening of null mutants.

Sterilization of *Arabidopsis* seeds was done with the solution composed of 0.1% Tween-20 and 10% sodium hyper chlorite. After 15 minutes of sterilization, the solution was discarded and seeds were washed three times with sterilized water. The seeds were then sown on the *Arabidopsis* medium (2.5 mM KNO₃, 1.25 mM KPO₄, 1 mM Ca(NO₃)₂, 1 mM MgSO₄, 35 μM Fe-EDTA, 7μM MnCl₂, 5 μM NaCl, 0.5 μM ZnSO₄, 0.25 μM CuSO₄, 0.1 μM NaMoO₄, 0.005 μM CoCl₂, 1.5% [w/v] agar, 1% [w/v] sucrose) (Okada and Shimura 1992). After stratification of the seeds at 4°C in the dark for 4 days, the seeds were germinated and grew on the vertically placed agar medium at 23°C with a long photoperiod (16h light period, 8h dark period). If necessary, 7-day-old seedlings grown on media plate were transferred onto soil and grown at 23°C in long photoperiod conditions.

For screening of transgenic seedlings, ½ MS media (2.3 g/L (NIHON PHARMACEUTICAL CO.), 50 μg/mL myo-inositol, 0.2 μg/mL thiamine, 0.05% [w/v] MES-KOH pH5.7, 0.7% [w/v] agar, 1% [w/v] sucrose) was used with appropriate antibiotics. The seedlings were screened on the antibiotics-supplemented media plates for 14 days.

Arabidopsis transformation was done using a floral dip method (Clough *et al.* 1998). *Agrobacterium tumefaciens* GV3101 (pMP90) harboring the destination vector was selected on antibiotics- supplemented LB plates. Single colony was grown in pre-culture, and then inoculated into growth media. The bacteria was harvested and suspended in a transformation solution containing 5% [w/v] sucrose and 0.05% [v/v] Silwet L-77. After the floral part of plants was dipped into the transformation solution, they were allowed to grow normally until seeds were harvested. The seeds were screened on antibiotics-supplemented media.

Vector construction

Full-length cDNAs of all BPP members except BPP5 were expressed under the ubiquitin promoter (pUB10), which was constitutively active in various tissues, and fused to GFP at the N-terminus using appropriate restriction enzyme cleavage sites. The pUB10::GFP-BPP5 expression vector was not constructed due to technical difficulties. Instead, GFP was inserted at the N-terminus of ATG start codon in the *BPP5* genomic clone, and cloned into pBIN42. For dual color visualization of a fusion protein and a MT marker, a transgenic Arabidopsis plant harboring a desired GFP-tagged protein was crossed with either a plant harboring pUB10::mCherry-TUB6, AtML::mCherry-TUB6 or WRKY::mCherry-TUB6, depending on the specific tissue region for microscopic observation. For the promoter-GUS assay, a 2.6-kb promoter region 5' upstream of each BPP member's ATG start codon was cloned into pGWB3 vector using the Gateway Cloning system.

Promoter-GUS assay

GUS staining was done on different tissues with some modifications from Jefferson *et al.* (1987). Observation of GUS staining was conducted on several independent transgenic lines from each promoter constructs to ensure the data consistency. The tissues were incubated in cold 90% (v/v) acetone during the tissues harvest. Tissues suspended in 90% acetone were incubated at room temperature for 20 min before washed with GUS staining solution (0.1 M NaPO₄ pH7.0, 10 mM EDTA, 0.1% (v/v) Triton x-100, 1 mM K₃Fe(CN)₆ and 1 mM K₄Fe(CN)₆) without 5-bromo-4-chloro-3-indolyl β-D-Glucuronide (X-Gluc). The wash solution was discarded and replaced with GUS staining solution supplemented with 2 mM X-Gluc. The staining solution containing tissue samples were incubated on ice for 30 min before incubated at 37°C overnight. On the next day, staining solution was discarded and samples were hydrated by serial of ethanol (EtOH) solution, before fixed with FAA solution for 30 min and kept in 70% EtOH at 4°C for storage. Images of GUS-stained tissues were acquired using Olympus MVX10 stereo microscope.

RT-PCR analysis

Total RNA was extracted from different tissues using the RNaseasy Plant Mini kit (Qiagen), and 1 μg of total RNA was used for the first-strand cDNA synthesis by SuperScript II reverse

transcriptase (Life Technologies). *ACT8* gene expression was used as a control. PCR was performed under the standard conditions of 25 cycles, and 10- μ L of the PCR product was checked using agarose gel electrophoresis, then stained with ethidium bromide.

Drug treatment

WT and mutant plants were grown on the Arabidopsis media supplemented with 3 μ M propyzamide. The seedlings were incubated vertically at 25°C with long photoperiod for 7 days. The angle of root skewing (α) was measured relative to the axis of gravitational force whereas the angle of cell file rotation (β) was measured in the bending region between elongation and maturation zone of the root.

Microscopic analysis of cell shapes

To investigate the size and density of palisade cells, first true leaves of 24-day-old seedlings were harvested in FAA solution (5% acetic acid, 45% EtOH and 5% formaldehyde), dried under a vacuum for 20 min and washed twice with 90% EtOH for 30 min. The samples were then submerged in chloral hydrate clearing solution overnight. For light microscopic observation, cleared samples were mounted with chloral hydrate solution under a coverslip. Images of palisade cells were acquired at three regions between the leaf margin and mid-rib vein using Olympus DP70 epifluorescence microscope.

To analyze the shape of cotyledon pavement cells at 1DAG, 2DAG and 3DAG, 5 images of PI-stained cotyledon pavement cells from 5 different seedlings were acquired using spinning disk confocal microscope setup with a Nikon ECLIPSE Ti inverted microscope, and EM-CCD camera iXon3 DU897 (Andor). Excitation energy was supplied by a 561 nm laser and Nikon S Plan Fluor 20x/0.45 objective lens was used. The pavement cells from the base of each cotyledon were acquired at the paradermal cross-sectional area (**Fig. 31A**). Images processing of the pavement cells was performed using ImageJ (W. Rasband, National Institutes of Health, Bethesda, MD) (**Fig. 31B**). Area, perimeter, circularity and aspect ratio of the cells were determined automatically using plugin in ImageJ. Skeleton analysis was used to automatically count the number of concave lobe (**Fig. 31C**). The morphometrical analysis of cotyledon pavement cells was kindly conducted by Dr. Takumi Higaki (Tokyo University).

Visualization of MTs with confocal spinning-disc microscopy

Time-lapse imaging of fluorescent protein localization was performed on the same spinning disk confocal microscope with adaptive focus and a Nikon Apo TIRF 60x/1.49 numerical aperture oil-immersion objective. Excitation energy was supplied by either 488 nm laser or 561 nm laser (Andor).

The measurement of MT dynamics were made from time-series images acquired from cotyledon pavement cells of 2DAG or 3DAG seedlings expressing pUB10::GFP-TUB6. Images were acquired at 2-s intervals for 151 repeats which approximately equivalent to 5 min. Trajectories of individual MTs were traced on images and converted into kymographs using tools in ImageJ.

The z-stack images of cells were acquired with z-step of approximately 0.2 μm . The images started from the optical sections of anticlinal wall at the middle of the cell and proceeded with projections of serial sections of several focal planes of the cortical cytoplasm next to the outer periclinal wall. The number of cortical MTs was determined by measuring the fluorescence density of GFP-tagged MTs adjacent to the periclinal or anticlinal walls at the lobe tips, and longitudinal center of the cell. The measurement was done in ten cells with at least two concave and convex lobes per image. The image processing was performed by Dr. Takumi Higaki.

Phylogenetic tree construction

The relationship phylogenetic tree of BPP homologs was constructed using Phylogeny.fr (<http://phylogeny.lirmm.fr/phylo.cgi/index.cgi>). Sequences of plant proteins were retrieved from the GenBank/EMBL data libraries.

Results

BPP family MAPs

BPP1 is a 64-kDa protein rich in Pro (11.2%) and basic amino acids (15%), having six homologs in *Arabidopsis* (**Fig. 7A**). Every BPP member shares a conserved basic region. The BPP members are grouped into three clades based on the phylogenetic tree constructed from four model plants: *Arabidopsis thaliana* (thale cress), *Oryza sativa* (rice), *Populus trichocarpa* (black cotton wood), and *Vitis vinifera* (wine grape) (**Fig. 7B**). Clade I consisted of BPP1, BPP2, BPP3 and BPP4. BPP5 alone belongs to Clade II whereas BPP6 is in Clade III. BPP7 is the most distant member and does not fit into any of the clades.

Expression patterns

To investigate organ/tissue-specific expression patterns of *BPP* genes, RT-PCR analysis was done on cDNAs synthesized from total RNA isolated from different plant tissues (**Fig. 8**). *BPP1*, *BPP2*, and *BPP5* showed strong expression level in most plant tissues. Since more than one amplified signals were detected for *BPP4*, specific PCR primers may be necessary to be re-designed to correctly analyze the transcript levels of this gene. *BPP7* was expressed at low or moderate levels in young seedlings and other vegetative tissues whereas *BPP3* and *BPP6* were hardly expressed.

Promoter-GUS analysis was carried out to examine the expression patterns of *BPP* genes in more detail. Approximately 2.6-kb regions 5' upstream of the ATG start codons were fused with the GUS reporter gene, and were introduced into *Arabidopsis* plants. GUS staining assays showed that *BPP1*, *BPP2*, and *BPP5* are expressed at high levels compared to the other four *BPP* genes (**Fig. 9, 10**). GUS expression levels of *BPP4* were weak, showing inconsistency with the RT-PCR analysis. The PCR primers used in the RT-PCR assay may not have been specific to the *BPP4* transcripts. *BPP2* and *BPP5* had expression in the style of carpels and the filament of stamens, indicating possible functions in these reproductive tissues (**Fig. 10G, S**). GUS expression of *BPP2*, *BPP6* and *BPP7* was found in the pollen grains (**Fig. 10H, X, AB**). GUS staining in young siliques was found for *BPP1*, *BPP2* and *BPP5* (**Fig. 10D, I, U**).

Subcellular localization of BPP proteins

Subcellular localization of GFP-BPPs was investigated in Arabidopsis plants harboring mCherry-TUB6 as a MT marker. The cDNAs of BPP2, BPP3, BPP4, BPP6, and BPP7 were expressed under the CaMV 35S promoter, while BPP1 and BPP5 were expressed under its genomic regulatory elements. Since GFP-BPP1 and GFP-BPP5 expressed under the genomic contexts complemented the *bpp* mutant phenotypes (see below), these N-terminal GFP-fusion proteins should be functional. Microscopic observation of epidermal cells of etiolated seedlings revealed that all GFP-BPP fusion proteins were co-localized with mCherry-TUB6 labeled cortical MTs (**Fig. 11**). Time-lapse imaging by spinning confocal microscopy was used to investigate dynamic behavior of GFP-BPPs on cortical MTs *in vivo*. All BPP proteins labeled MTs lattice without any preference to MT ends or other particular MT locations.

Mutant phenotypes

To investigate *in vivo* functions of BPPs, several T-DNA insertion lines were obtained from Salk Institute Genomic Analysis Laboratory. The T-DNA insertion was checked by PCR genotyping using primers flanking the insertion site (**Fig. 12**). Several independent alleles were isolated for BPP1, BPP2, BPP3 and BPP5. For BPP1, T-DNA insertion was at 3rd intron, 4th exon, and 3rd exon for *bpp1-1*, *bpp1-3* and *bpp1-4*. T-DNA insertion was at 4th exon of *bpp2-5*. For BPP3, *bpp3-1* and *bpp3-2* had T-DNA insertion at 3rd exon and 2nd intron. For BPP5, both *bpp5-1* and *bpp5-2* had T-DNA insertion at 5th exon. For subsequent experiments, *bpp1-4*, *bpp2-5*, *bpp3-1*, and *bpp5-1* were used to generate several double and triple mutants. In 5-day-old seedlings, the *bpp1 bpp5* double and *bpp1 bpp2 bpp5* triple mutants had shorter petioles and rounder cotyledons (**Fig. 13A**). When grown on the Arabidopsis agar media placed vertically, the root length was slightly reduced in the mutants, especially in *bpp1 bpp2 bpp5* triple mutant (**Fig. 13B, C**). Growth was also retarded in the aerial parts of young seedlings and mature plants. The short petiole phenotype was even evident in the 3-week-old plants, where the petiole length of the first true leaf was reduced to nearly half in the triple mutant compared to wild type (**Fig. 14B, E**). The length and width of the leaf blade in the double and triple mutants were also 30% smaller, causing the area of first leaf to drop by approximately 30% (**Fig. 14B, C, D, F**). The cell size and the cell density of palisade cells of the first leaf were not different between wild type and the mutants (**Fig.**

15D, E). The smaller leaf phenotype in double and triple mutants was contributed by the decrease of the total palisade cell number per leaf, which showed roughly 30% reduction (**Fig. 15C**). Apart from that, shorter inflorescence stem was observed in some of the mutants, especially the triple mutant (**Fig. 16**). As clearly seen in the sepals, the floral organs in *bpp1 bpp5* double mutant and *bpp1 bpp2 bpp5* triple mutant were also smaller (**Fig. 17C**). The double and triple mutants had shorter siliques and produced less seeds (**Fig. 17A, B**).

I noticed an interesting phenotype in *bpp1 bpp5* and *bpp1 bpp2 bpp5* mutants. Cotyledon pavement cells in these mutants were round, compared to jigsaw puzzle-like shapes in wild-type cells (**Fig. 18P-U**). To examine cell shape development, time-point observation was conducted according to Armour *et al.* (2015) with some modifications. Lobe development was characterized by monitoring cells from the base of cotyledons on 1 day after germination (1DAG), 2DAG, and 3DAG (**Fig. 19A**). The number of concave lobes in a cell was automatically quantified by reducing the cell shape to a skeleton outline and by counting the number of skeleton branches (**Fig. 19C**). Ten pavement cells were selected from each of 5 cotyledons (total 50 cells). At 1DAG when the cotyledons had just unfurled, wild-type cells were small with few lobes. By 2DAG and 3DAG, the cells grew larger and became more complex in shape with multiple lobes. The cell size of double and triple mutants was indistinguishable from the wild-type cell size at all three time-points, showing similar progressive increment (**Fig. 20B**). The cell perimeter of the mutants was initially similar with that of wild type, but became significantly smaller by 3DAG (**Fig. 20D**). The circularity index of the mutant cells was larger than the wild-type index at 2DAG and 3DAG, indicating the mutant cell shape was more circular and less complex with shorter perimeter length (**Fig. 20F**). Furthermore, the ratio of major length to the minor length of a cell was smaller in the mutant than the wild-type ratio, as indicated by the aspect ratio (**Fig. 21B**). At 1DAG, wild-type and mutant cells had similar lobe numbers, but at 2DAG and 3DAG, the lobe number in the mutants did not increase as much as wild type (**Fig. 21F**). Besides these defects in horizontal anisotropic expansion, the pavement cells in *bpp1 bpp5* and *bpp1 bpp2 bpp5* mutants showed rounder and bulged outer cell walls, compared to flat cell surface in wild-type cells (**Fig. 23B, C**). These results indicate that the mutant pavement cells expand normally but do not develop the characteristic inter-digitated shapes with several lobe and neck regions.

Complementation studies

To validate the phenotypes exhibited by the *bpp1 bpp5* and *bpp1 bpp2 bpp5* mutants are caused by the loss-of-function of *BPP1* and *BPP5*. I transformed the mutants with either the genomic fragment of *BPP1* or *BPP5* in which GFP had been inserted at the N-terminus of the coding region (designated as *gGFP-BPP1* and *gGFP-BPP5*). The *gGFP-BPP1* and *gGFP-BPP5* constructs successfully rescued all the phenotypic defects observed in these *bpp* mutants (**Fig. 14B, 16A, 17, 22**). The morphologies of petioles, leaf blades, inflorescence stems, flowers and siliques of the complemented mutants were indistinguishable from those of wild type. Abnormal shapes of cotyledon pavement cells in the *bpp* mutants were also rescue by the transgenes. Hence, these results indicate that the observed phenotypes are indeed caused by the functional loss of *BPP1* and *BPP5*, and these two *BPP* genes are highly redundant in controlling anisotropic cell expansion in many cell types. Also, I conclude that *GFP-BPP1* and *GFP-BPP5* are functional fusion proteins.

MT arrays

GFP-BPP1 expressed under its genomic regulatory elements preferentially labeled radiating MTs on the outer periclinal wall and the extending anticlinal MTs at the convex side of the emerging lobes at 1DAG (**Fig. 24**). This preferential localization of *BPP* on particular MT arrays appeared to be more evident for *GFP-BPP1* than for *GFP-BPP5*, although we should note that the former was expressed in the *bpp* triple mutant background whereas the latter was expressed in the wild-type background. This preferential localization of *BPP1* on the radiating MT arrays underscores its functions on the formation of the lobe formation.

To understand whether organization of MTs is associated with the abnormal lobe development in the *bpp* mutants, cortical MTs of cotyledon pavement cells were imaged on 1DAG, 2DAG, and 3DAG using Arabidopsis plants expressing *GFP-TUB6* which decorated cortical MTs. Firstly, cortical MTs in wild-type cells were characterized during the lobe formation (**Fig. 25**). At 1DAG when pavement cells still had few lobes, cortical MTs were randomly distributed beneath the outer periclinal wall. Later in 2DAG and 3DAG, MTs were enriched at the anticlinal side of the developing convex lobe (**Fig. 25A**). In the outer periclinal wall, MTs were seen persistently

enriched at the convex side of the lobes, forming radiating arrays at the neck region with distinct MT bundles.

However, *bpp1 bpp5* and *bpp1 bpp2 bpp5* mutants exhibited abnormal MT organization. On 1DAG, 2DAG, and 3DAG, MTs did not show any preferred enrichment at the anticlinal walls of concave or convex lobes (**Fig. 25B, C**). At the outer periclinal walls, MTs were essentially randomly distributed with no transverse MT arrays connecting the neck region (**Fig. 26C-F**). The growth and shrinkage velocities of the MT plus end were similar between wild-type and triple mutant cells (**Fig. 27**). This indicates that BPPs do not regulate the reorientation of MT arrays by modulating the growth and shrinkage velocities of cortical MTs.

By using EB1b-GFP as a growing plus-end marker and mCherry TUB6 as a general MT label, the parallel MT arrays that bridge between two opposing neck regions in 3DAG wild-type cells are composed of cortical MTs that direct their plus ends toward both directions, forming bi-polar arrays (**Fig. 28C**). These MTs at the outer periclinal wall often extended down the anticlinal wall of the convex lobe. In contrast, the corresponding concave lobe consisted of less MTs, compared with the opposing convex lobe. This observation is consistent with previous findings (Armour *et al.*, 2015).

To quantify the MT phenotypes, MT densities were measured. For each genotype at different time-points, 10 cells were selected with three regions measured for periclinal walls and with two regions for anticlinal walls. At 2DAG and 3DAG, the MT density at the convex side was significantly larger than the density at the concave side of the same lobes in wild-type cells (**Fig. 29C**), whereas the MT densities at both sides were not statistically different in the double and triple mutants (**Fig. 29D, E**). For the anticlinal walls, the ratio of the MT density at convex lobe to that at the neighboring region was measured (**Fig. 30A**). Wild-type cells showed significantly higher MT density at the lobe region, compared to the neighboring regions at 3DAG (**Fig. 30C**). However, the mutant cells had similar values at 2DAG and 3DAG (**Fig. 30D, E**). To see whether average densities of cortical MTs are different between wild-type and mutant cells, MT density spanning the cell center line corresponding to the major growth axis was measured (**Fig. 31A**). Total of 20 cells were measured for each genotype at 2DAG and 3DAG. The results revealed that there are no significant differences in MT density in wild-type cells, and double and triple mutant cells (**Fig.**

31B). These findings showed that the locally biased enrichment and reorganization of particular MT arrays do not occur during early lobe development in the *bpp* mutant cells, which results in failure to form complex, inter-digitating cell shapes.

Chemical treatment

To investigate the sensitivity of MT to MT-disrupting drugs, Arabidopsis seedlings were grown on the agar media containing different concentrations of propyzamide. Propyzamide is a benzamide class of herbicides that binds β -tubulin, destabilizes MTs and induces left-handed helical growth in elongating Arabidopsis epidermal cells (Young and Lewandowski, 2000; Nakamura et al., 2004). After seven days of the propyzamide treatment, the angles of root skewing (α) and the cell file rotation (CFR) (β) of the root epidermis between the elongation and maturation zones of the root were measured. Single *bpp* mutants were indistinguishable from wild-type plants in their sensitivity toward the MT drug. In contrast, the *bpp1 bpp5* and *bpp1 bpp2 bpp5* mutants showed decreased leftward root skewing and right-handed CFR in the presence of 3 μ M propyzamide (**Fig. 32**). This suggested that the double and triple mutants are less sensitive to propyzamide.

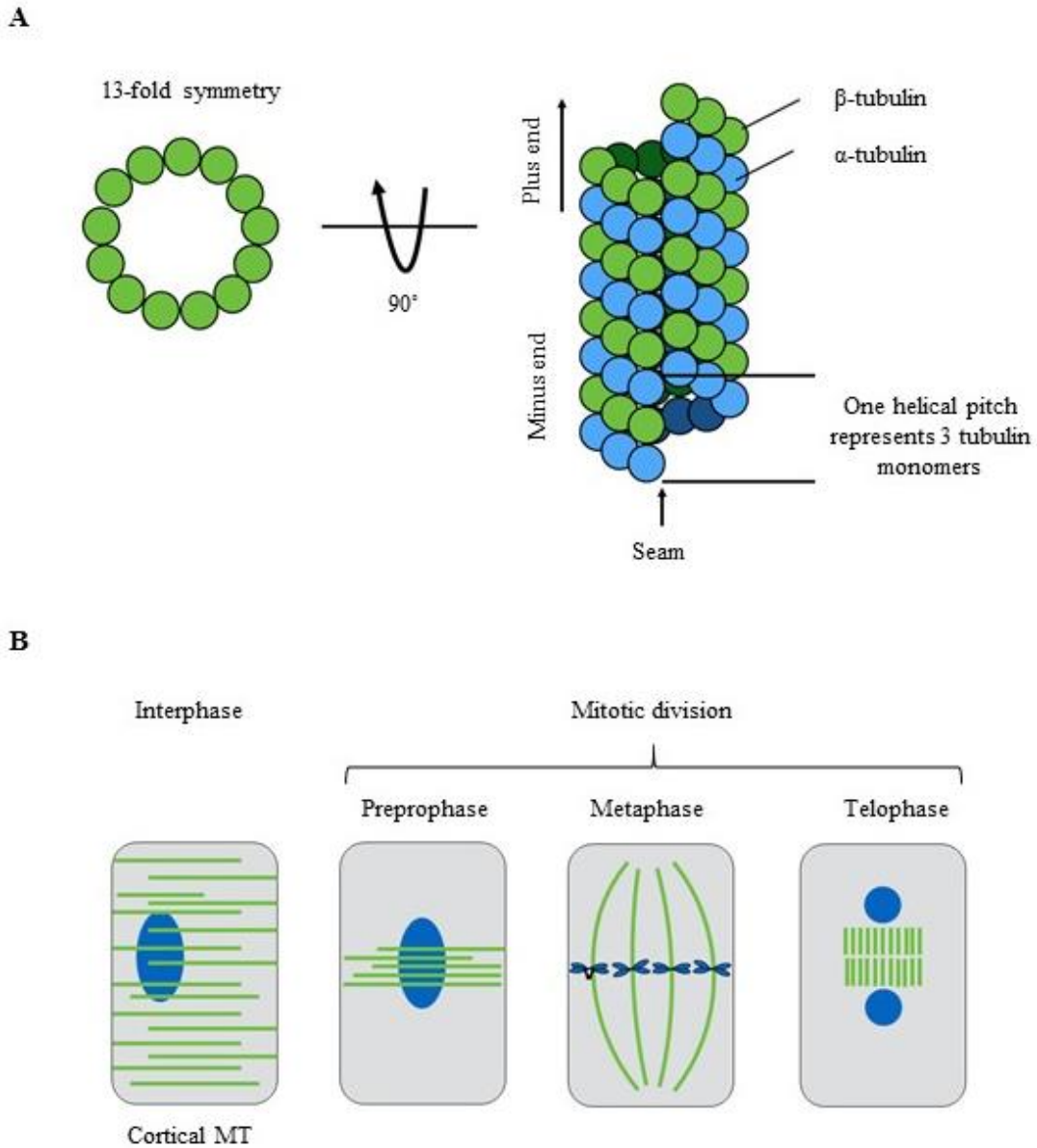


Fig. 1. Schematic illustrations of MT arrays through plant cell cycle and MT structure.

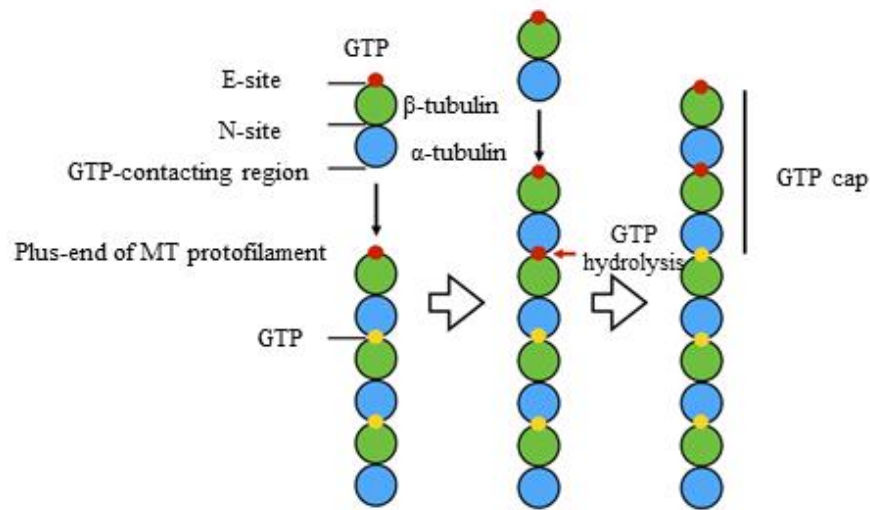
(A) MT is a 13-protofilament polymer composed of multiple α -tubulin and β -tubulin heterodimers stacked longitudinally.

(Modified from Hashimoto, 2015)

(B) Green color indicates cortical MTs during interphase and spindle bundles during mitotic division.

(Modified from Wasteneys, 2002)

A



B

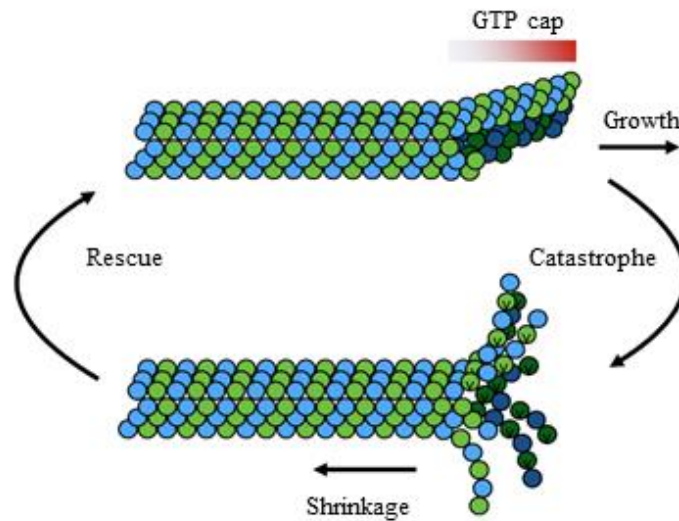


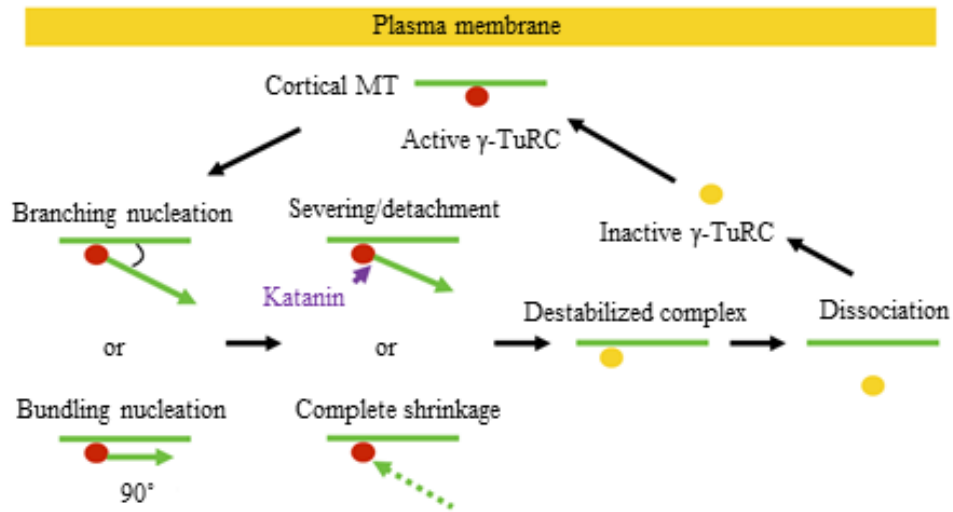
Fig. 2. Dynamic instability of MTs

(A) The addition of $\alpha\beta$ -tubulin heterodimer to the MT growing plus end through GTP hydrolysis.

(B) Steady MT growth is stabilized by the GTP cap whereas catastrophe event occurs when the GTP cap is lost, resulting in rapid shrinkage. Rescue event takes place when the GTP cap is restored, promoting MT growth again.

(Modified from Hashimoto, 2015)

A



B

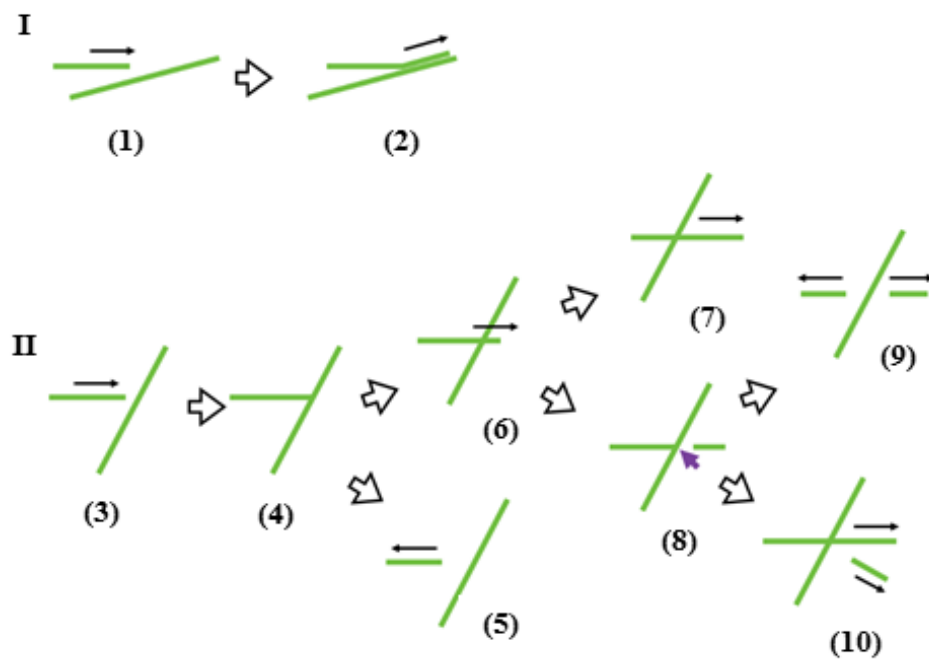


Fig. 3. Arrangement of cortical MT array through MT nucleation and MT-MT interactions.

(A) Model of MT-dependent nucleation in plant cortical arrays. MT nucleation is initiated by active γ -TuRC binding to preexisting cortical MT at plasma membrane. Daughter MT nucleates either at approximately 40° or in parallel to mother MT.

(B) Models of MT-MT interactions and their outcomes.

(Modified from Hashimoto, 2015)

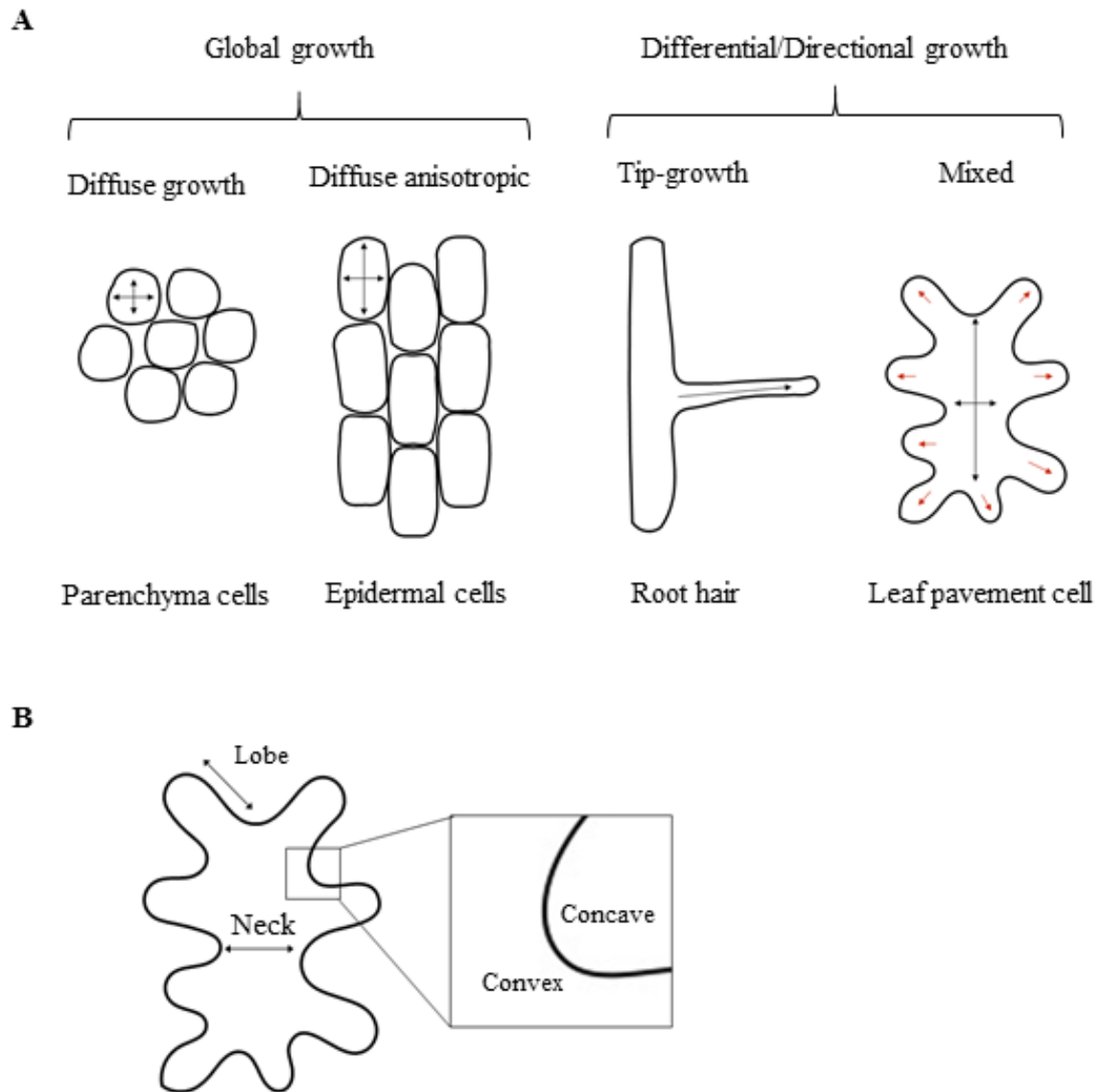


Fig. 4. Schematic representation of two main plant cell growth and leaf pavement cell shape.

(A) Two main plant cell growths: global and differential/directional growth. Anisotropic and localized cell expansion occur simultaneously in mixed growth. Black arrow indicates diffuse growth whereas red arrow indicates localized cell expansion.

(Modified from Guerriero *et al.*, 2014)

(B) Mixed growth of leaf pavement cell contributes to lobe and neck development.

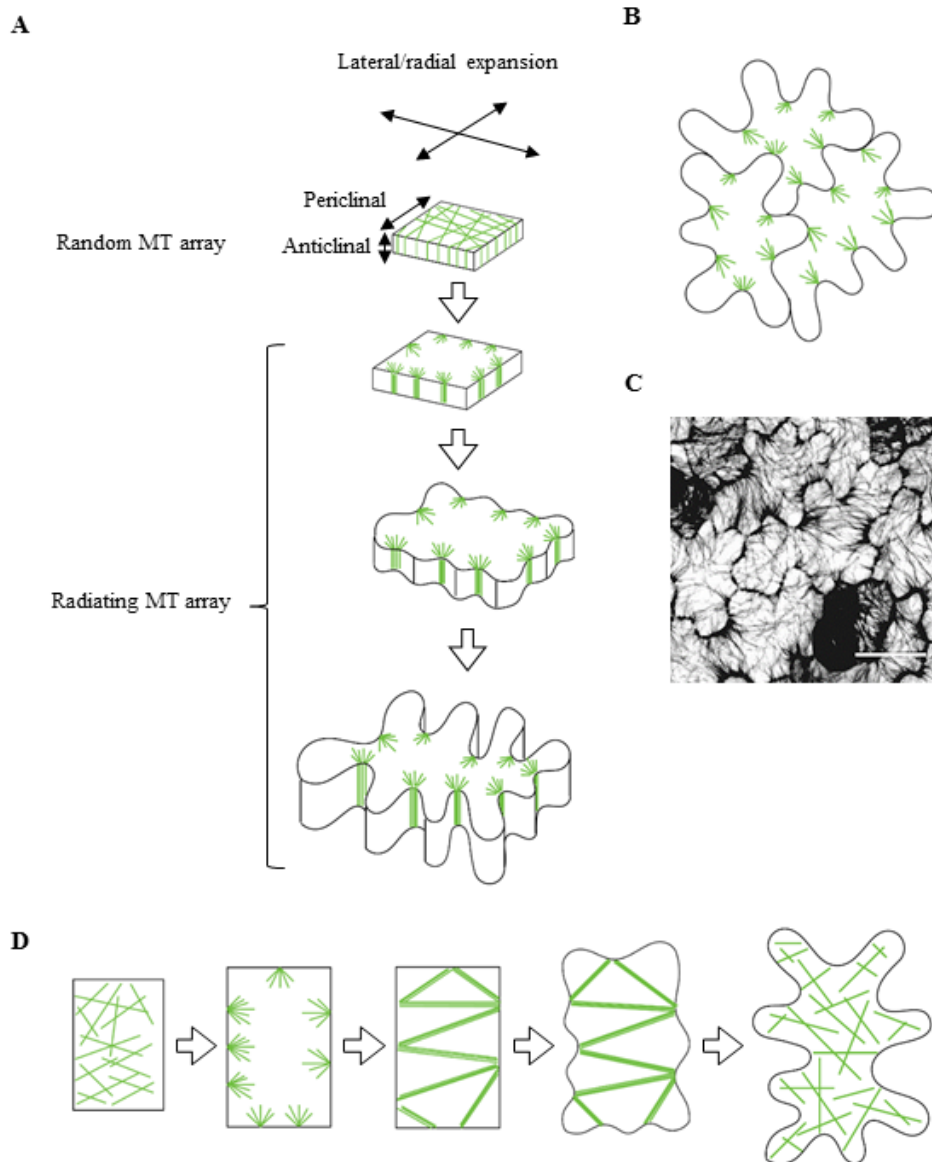


Fig. 5. Cortical MT arrays during pavement cell morphogenesis.

(A) Changes of random cortical MT array to organized radiating MT array that predict the position of necks. Green color indicates MTs. (Modified from Panteris and Galatis, 2005)

(B) Radiating MT arrays alternate between neighboring pavement cells, resulting in ‘jigsaw-puzzle’-like patterns.

(C) Confocal microscopic imaging of GFP-TUB6 labeled in 2DAG cotyledon pavement cell. Scale bar: 10 μm .

(D) Radiating MT arrays promotes the transverse MT arrays that constrict cell expansion, resulting in neck formation. (Modified from Fu *et al.*, 2005)

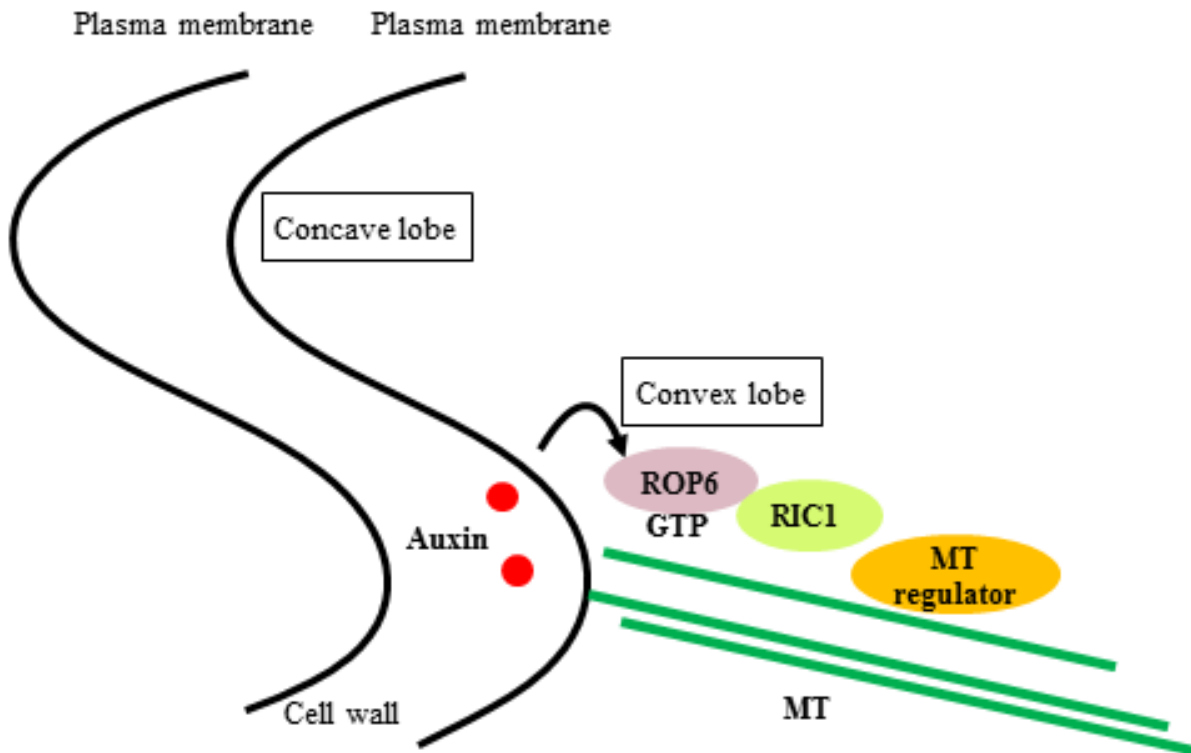


Fig. 6. Working model of convex lobe formation in pavement cell.

The convex lobe is formed through the ROP6-RIC1 signaling pathway that regulates MT arrangement. The ROP6 is activated by auxin perception. Activated ROP6 subsequently binds to RIC1. The ROP6-RIC1 complex then activates unknown MT regulator to control WT array at the convex lobe.

(Modified from Lin *et al.*, 2013).

Arabidopsis Genome Initiative Code	emPAI Scores	Predicted Domains/ Protein Features	Subcellular localization
AT3G53320 (MAP55L)	0.28	No	MT
ATG5G57410	3.52	Afadin/alpha-actinin-binding domain	MT
AT5G07590	2.89	WD40 (Trp-Asp REPEATINGDOMAIN40) repeat	Cytosol
AT5G16730	0.35	Sepctrin/alpha	MT
AT1G15200	1.60	Pinin/Ser-Asp-Lys/memA domain	Cytosol
AT4G17620	1.91	Gly-ruch protein	Cytosol
AT2G40070 (BPP1)	1.32	Basic Pro-rich protein (BPP1)	MT
AT5G24710	1.13	WD40 (Trp-Asp REPEATINGDOMAIN40) repeat	Cytosol
AT3G13990	0.08	DUF1296 (kinase related)	Cytosol
AT2G07360	1.01	SH3 (SRC HOMOLOGY3) domain and Armadillo-type fold	Cytosol
AT1G14380	0.16	IQD28; IQ calmodulin-binding domain	MT
AT1G19870	0.18	IQD32; IQ calmodulin-binding domain	MT

Table 1. Candidates of MAPs purified from Arabidopsis suspension culture cell

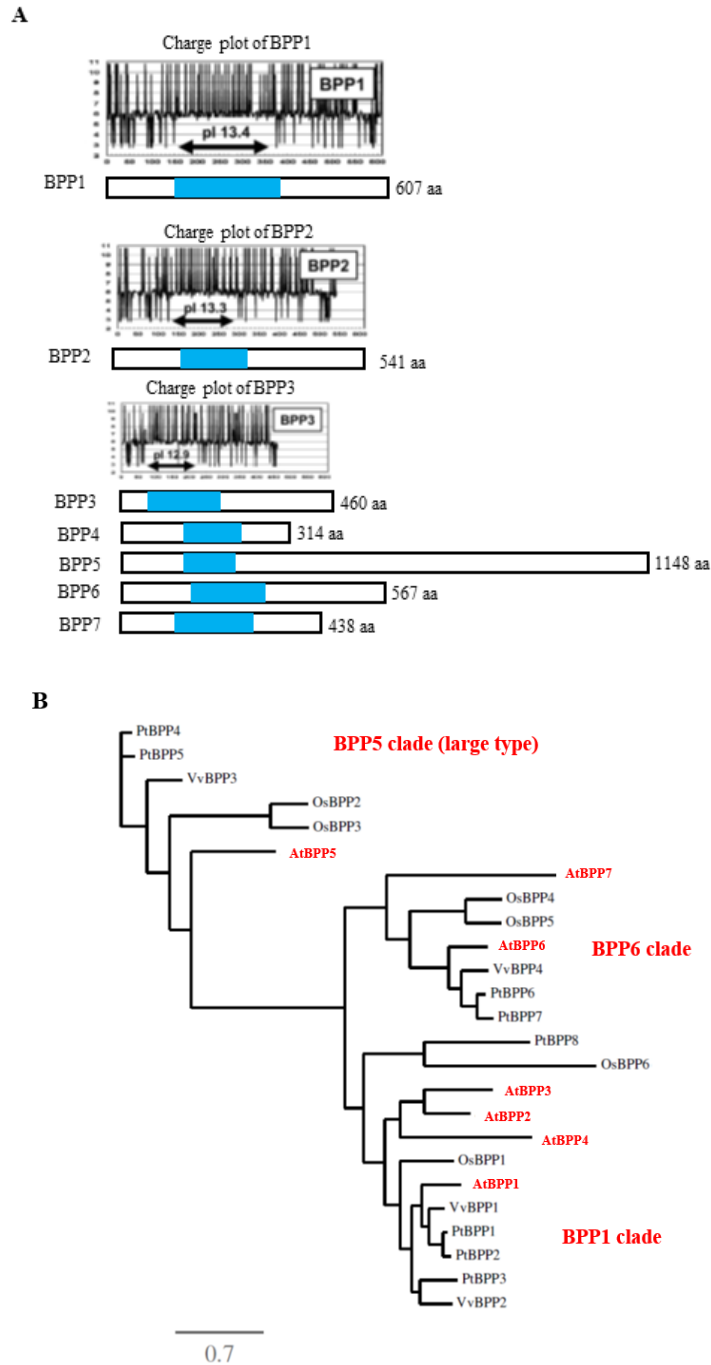


Fig. 7. Protein structure of BPP family and phylogenetic tree.

(A) The seven Arabidopsis BPPs contain a conserved basic domain indicated by blue box.

(B) Phylogenetic relationships of BPP1 homologs from *Arabidopsis thaliana* (thale cress), *Oryza sativa* (rice), *Populus trichocarpa* (black cottonwood), and *Vitis vinifera* (wine grape).

(Modified from Hamada *et al.*, 2013)

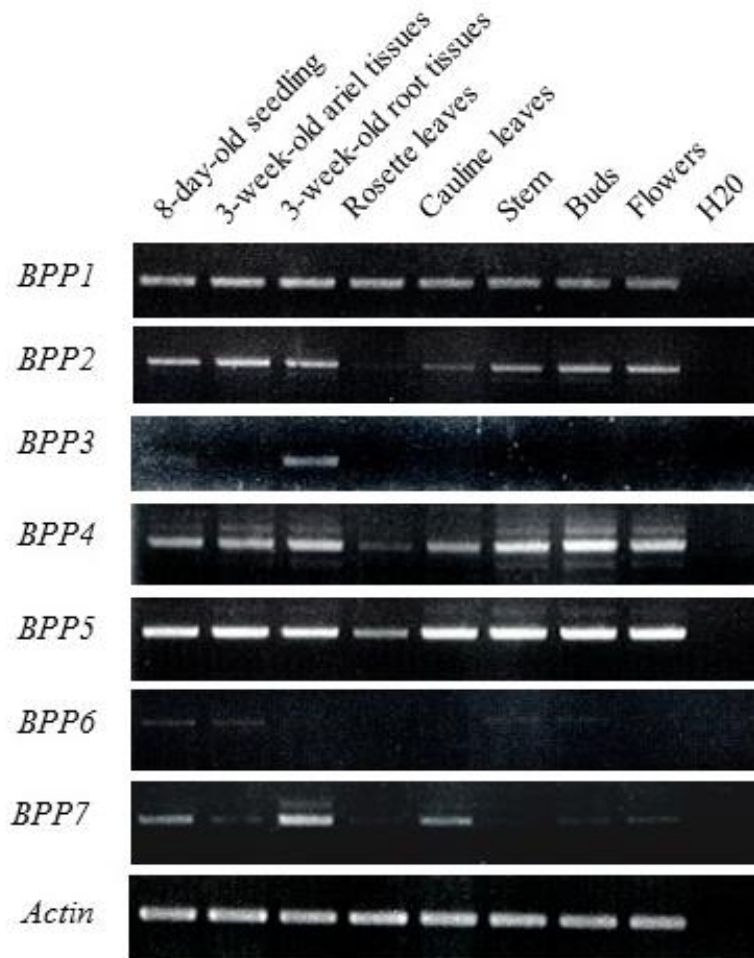


Fig. 8. RT-PCR analysis of BPPs expression pattern

RT-PCR of seven Arabidopsis BPPs in different tissues during specific developmental stages. Actin was used as control.

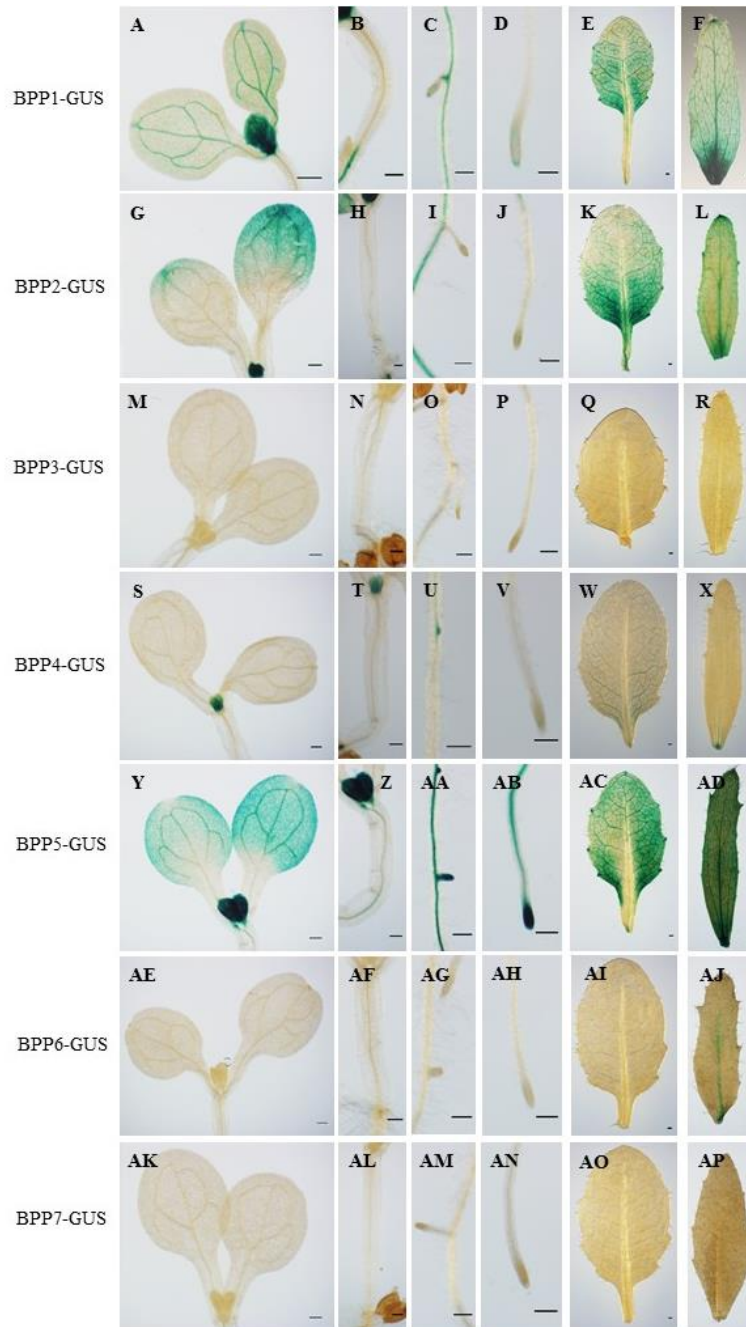


Fig. 9. Promoter-GUS analysis of BPPs in vegetative tissues

Promoter-GUS staining of BPP1 (A-F), BPP2 (G-L), BPP3 (M-R), BPP4 (S-X), BPP5 (Y-AD), BPP6 (AE-AJ), and BPP7 (AK-AP). Different tissues: 7-day-old cotyledons (A, G, M, S, Y, AE, AK); hypocotyl (B, H, N, T, Z, AF, AL); lateral root (C, I, O, U, AA, AG, AM); root tip (D, J, P, V, AB, AH, AN); rosette leaf (E, K, Q, W, AC, AI, AO), and cauline leaf (F, L, R, X, AD, AJ, AP) were stained. Scale bar: 0.2 mm.

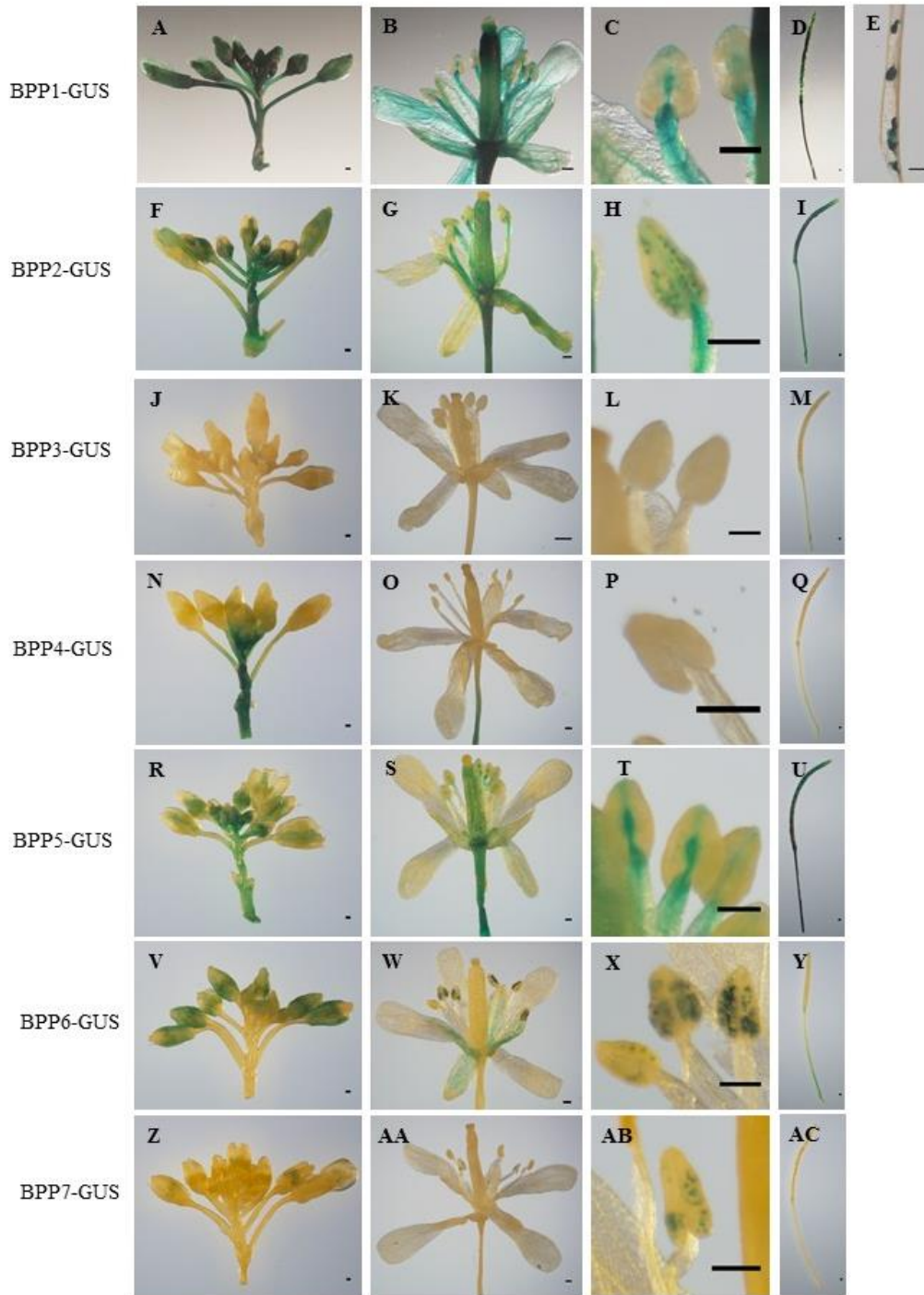


Fig. 10. Promoter-GUS analysis of BPPs in reproductive tissues.

Promoter-GUS staining of BPP1 (A-E), BPP2 (F-I), BPP3 (J-M), BPP4 (N-Q), BPP5 (R-U), BPP6 (V-Y), and BPP7 (Z-AC). Different tissues: buds (A-Z); flowers (B-AA), stamen (C-AB), siliques (D-AC), and seeds (E) were stained. Scale bar: 0.2 mm.

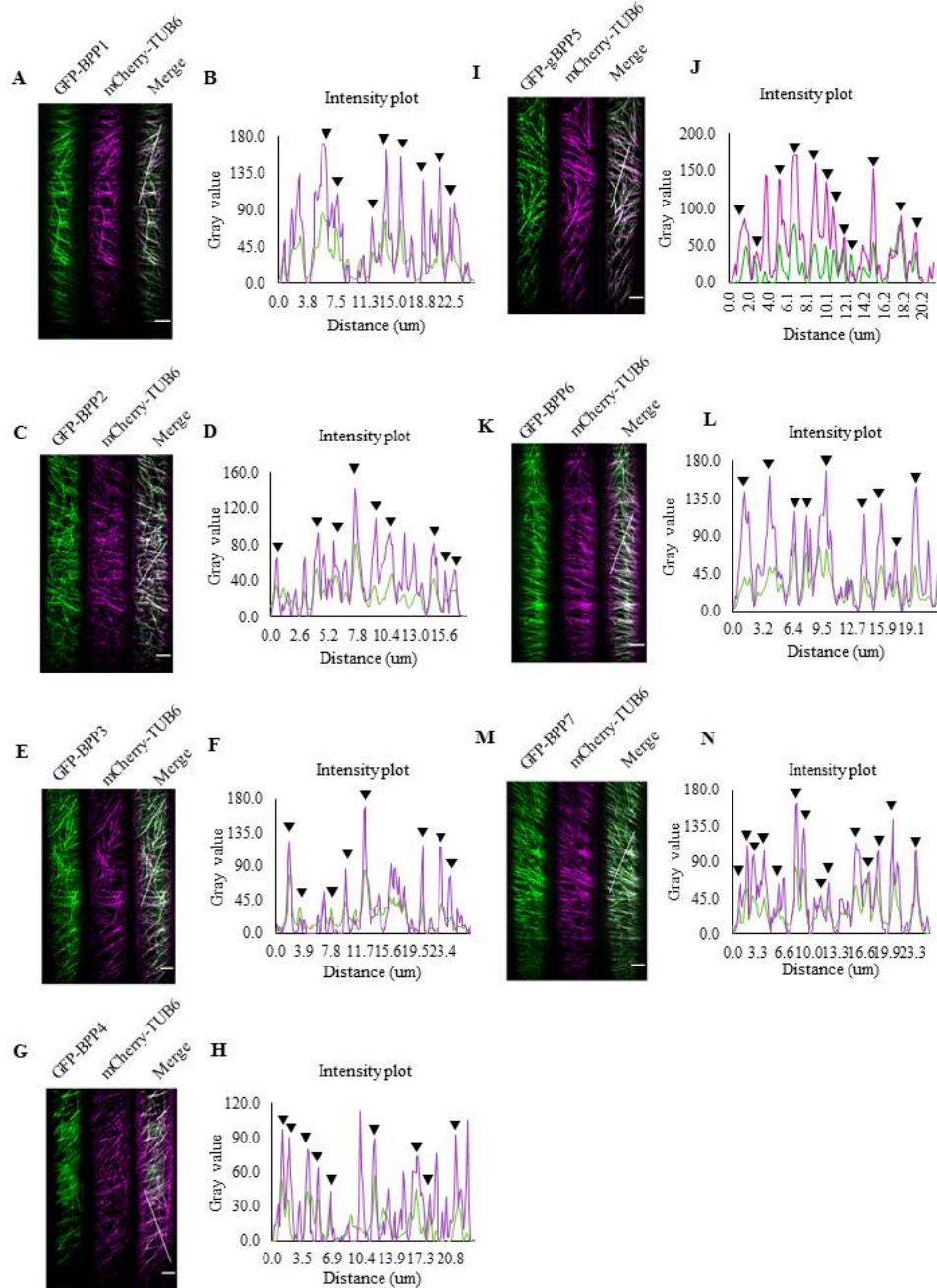
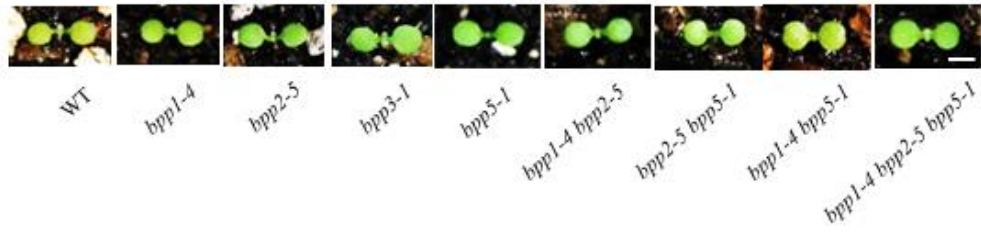


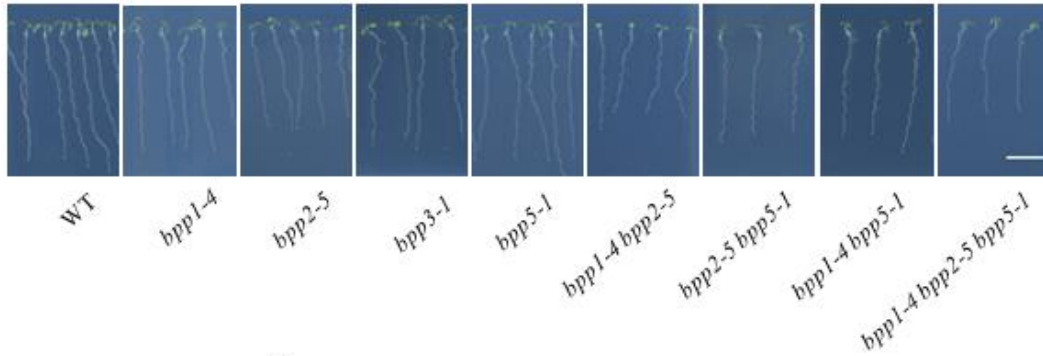
Fig. 11. Subcellular localization of BPPs onto cortical MTs.

Confocal microscopic imaging of overexpressed GFP-BPP1 (A), GFP-BPP2 (C), GFP-BPP3 (E), GFP-BPP4 (G), GFP-BPP6 (K), and GFP-BPP7 (M), whereas genomic expression of GFP-gBPP5 (I) in 8-day-old root epidermal cells. Intensity plot of GFP-BPP1 (B), GFP-BPP2 (D), GFP-BPP3 (F), GFP-BPP4 (H), GFP-gBPP5 (J), GFP-BPP6 (L) or GFP-BPP7 (N) in green line with mCherry-TUB6 in magenta line. Arrowhead indicates overlapping peaks. Scale bar: 5 μm .

A



B



C

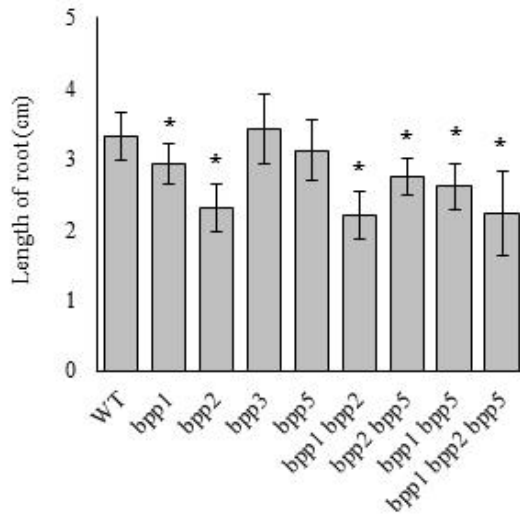


Fig. 13. Phenotype of *bpp* mutant seedlings.

(A) 5-day-old seedlings grown directly on soil. Scale bar: 2mm.

(B) 7-day-old seedlings grown on Arabidopsis media placed vertically. Scale bar: 1cm.

(C) Root length measurement of seedlings shown in (B). Statistical significant differences between WT and each mutant are denoted by an asterisk ($P < 0.05$, Student's t-test). $n = 20$ seedlings. Scale bar: 1cm.

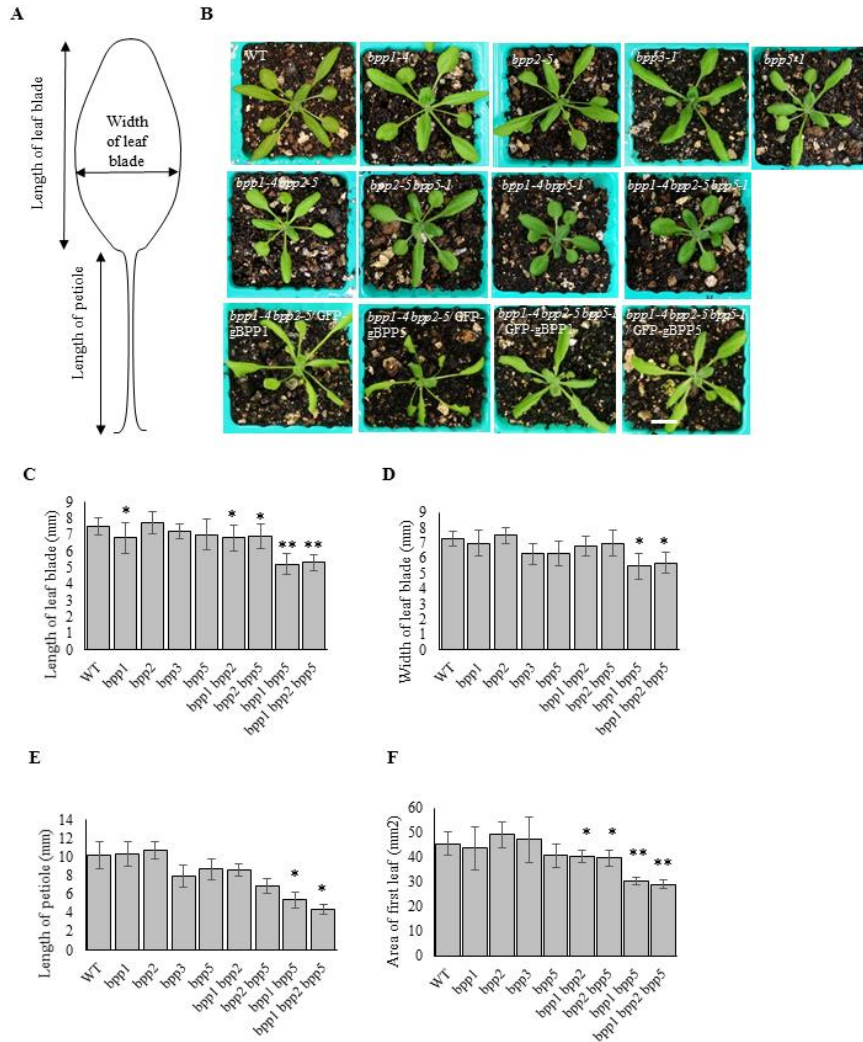


Fig. 14. Phenotypic defects of *bpp* mutants in leaf development.

(A) Schematic diagram of first true leaf.

(B) 21-day-old plants grown on soil. Scale bar: 1 cm.

(C) Length of leaf blade of first leaf. Statistical significant differences between WT and each different genotype are denoted with asterisk (* $P < 0.05$; ** $P < 0.001$, Student's t-test). $n = 10$.

(D) Width of leaf blade of first leaf. Statistical significant differences between WT and each different genotype are denoted with asterisk ($P < 0.05$, Student's t-test). $n = 10$.

(E) Length of petiole of first leaf. Statistical significant differences between WT and each genotype are denoted with asterisk ($P < 0.05$, Student's t-test). $n = 10$.

(F) Area of first leaf. Statistical significant differences between WT and each genotype are denoted with asterisk (* $P < 0.05$; ** $P < 0.001$, Student's t-test). $n = 6$ leaves.

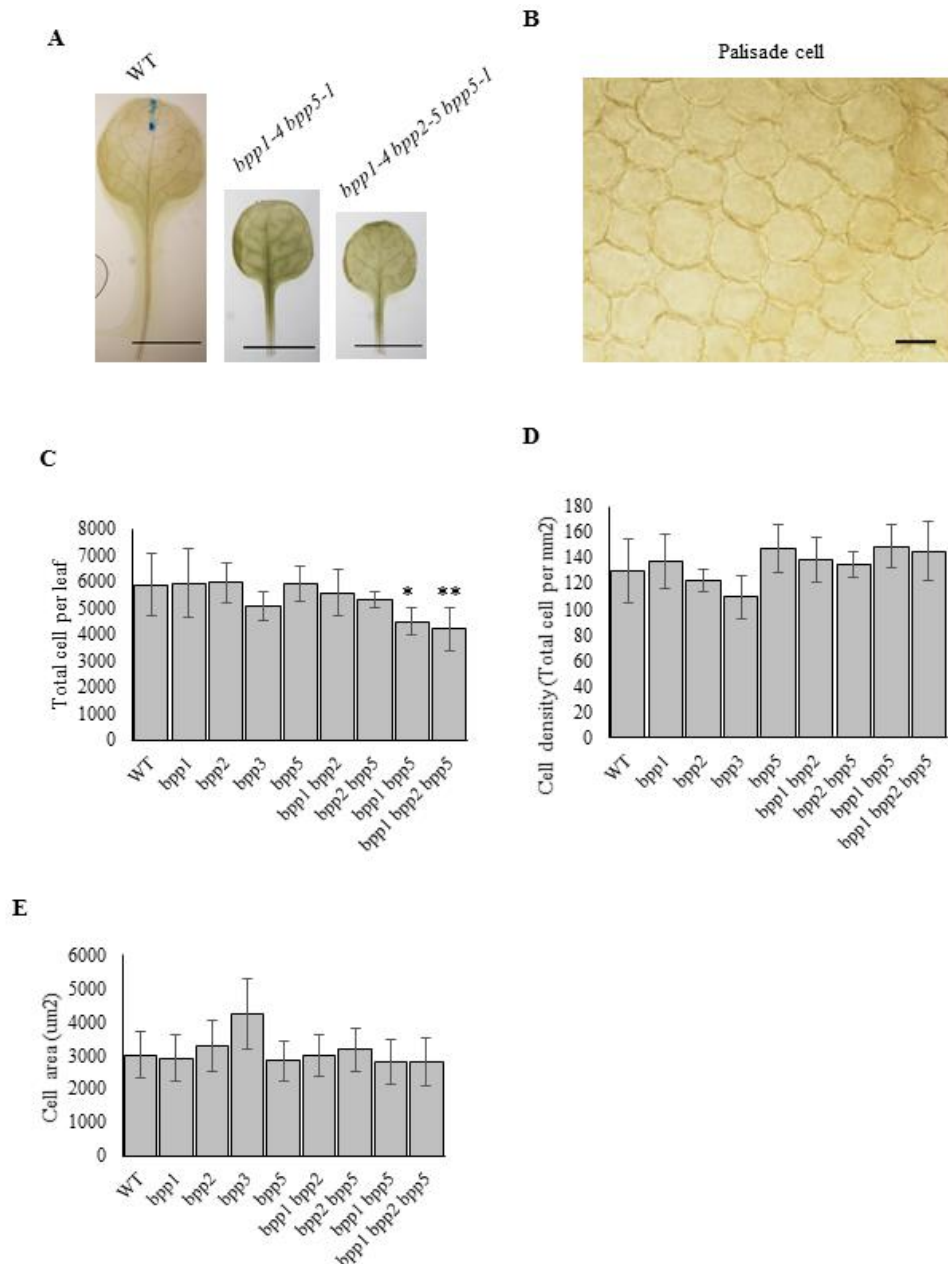


Fig. 15. Measurement of palisade cell in first leaf.

(A) First true leaf of WT, *bpp1-4 bpp5-1* and *bpp1-4 bpp2-5 bpp5-1*. Scale bar: 5mm.

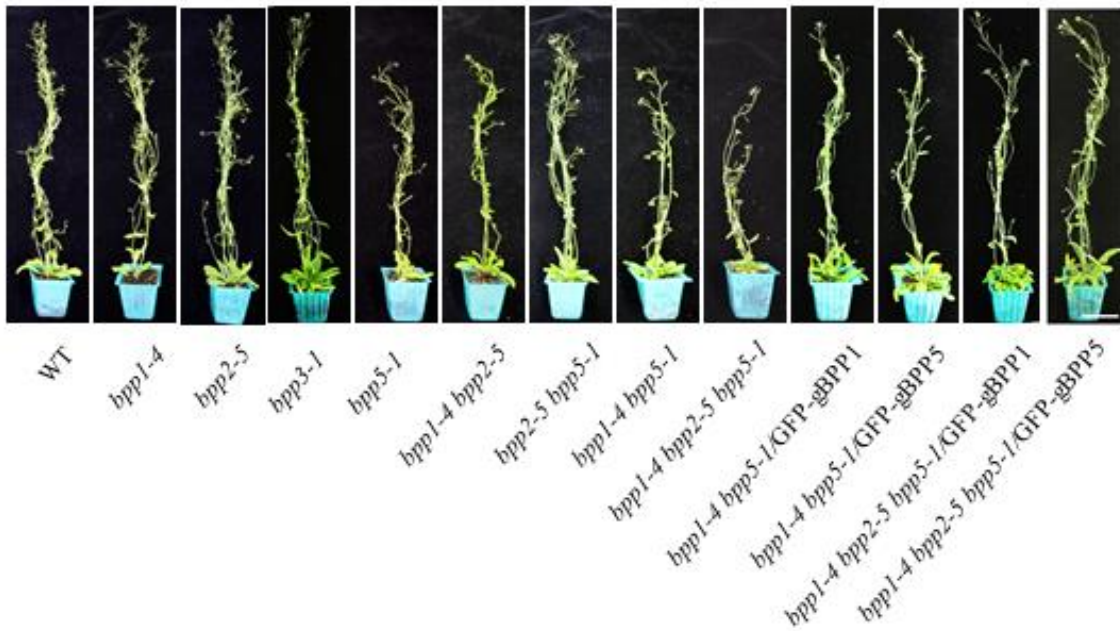
(B) Representative photo of palisade cell in first true leaf of 24-day-old plant. Scale bar: 50 μm.

(C) Total palisade cell per leaf. Statistical significant differences between WT and mutants are denoted with asterisk (* $P < 0.05$; ** $P < 0.001$, Student's t-test). $n = 6$ leaves.

(D) Cell density in first true leaf. $n = 6$ leaves.

(E) Mean value of palisade cell area in first true leaf. $n = 30$ cells per leaf

A



B

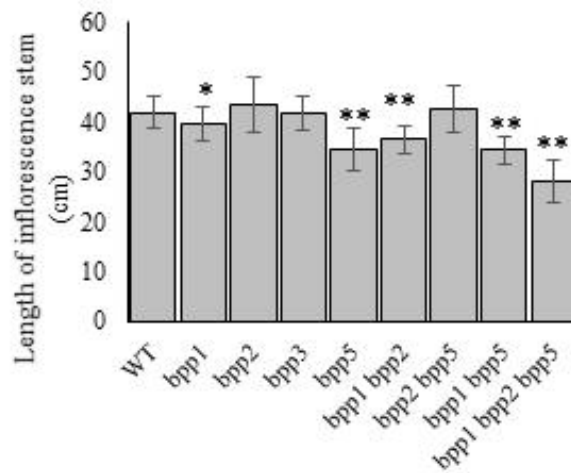


Fig. 16. Inflorescence stem of *bpp* mutants.

(A) 38-day-old plants grown on soil. Scale bar: 5 cm.

(B) Length of inflorescence stem of different genotypes. Statistical significant differences between WT and each mutant are denoted with asterisk (* $P < 0.05$; ** $P < 0.001$, Student's t-test). $n = 13$ plants.

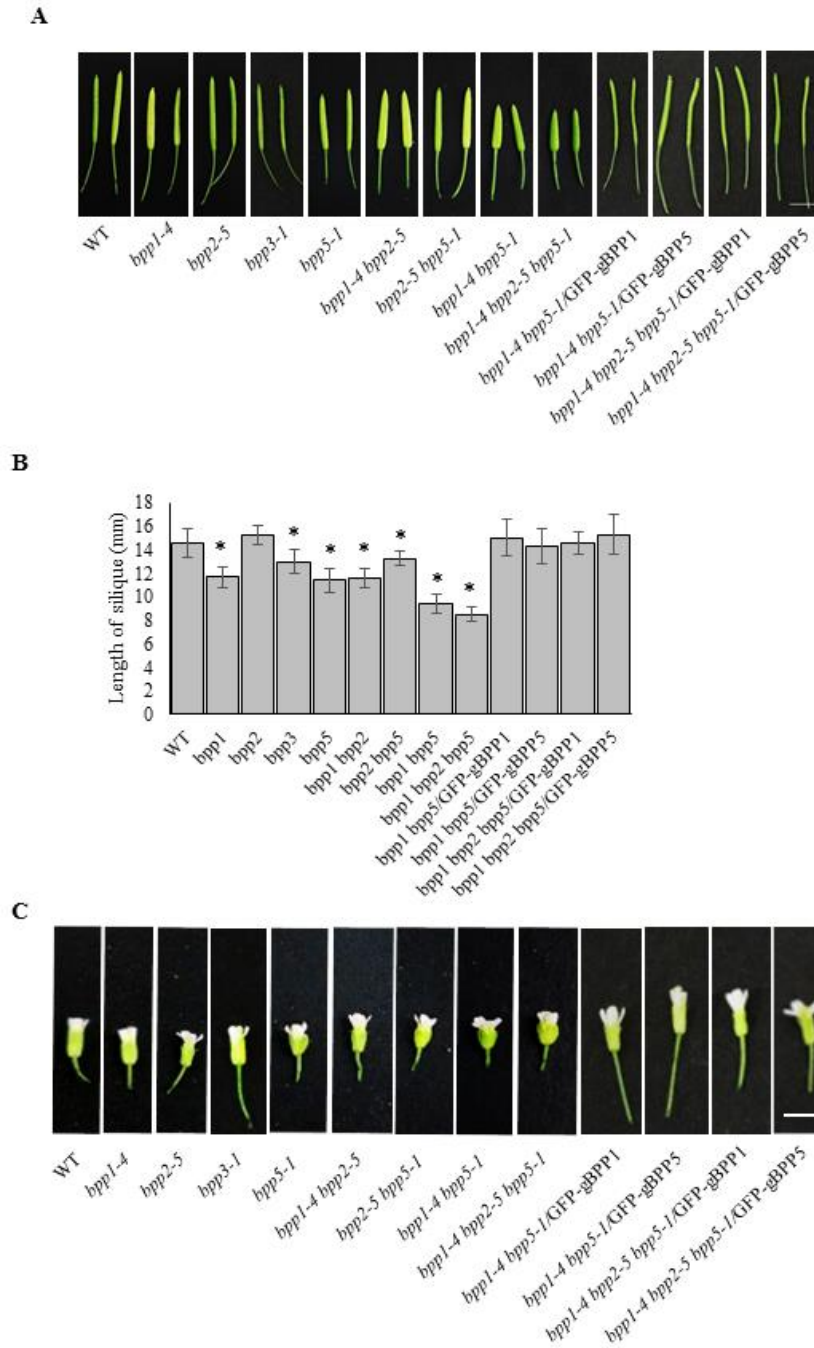


Fig. 17. Phenotypic defects in reproductive organs.

(A) Mature siliques of different genotypes. Scale bar: 0.5 cm.

(B) Length of mature siliques of different genotypes. Statistical significant differences between

WT and other genotypes are denoted with asterisk ($P < 0.05$, Student's t-test). $n = 30$ siliques.

(C) Flower of different genotypes. Scale bar: 2.5 mm.

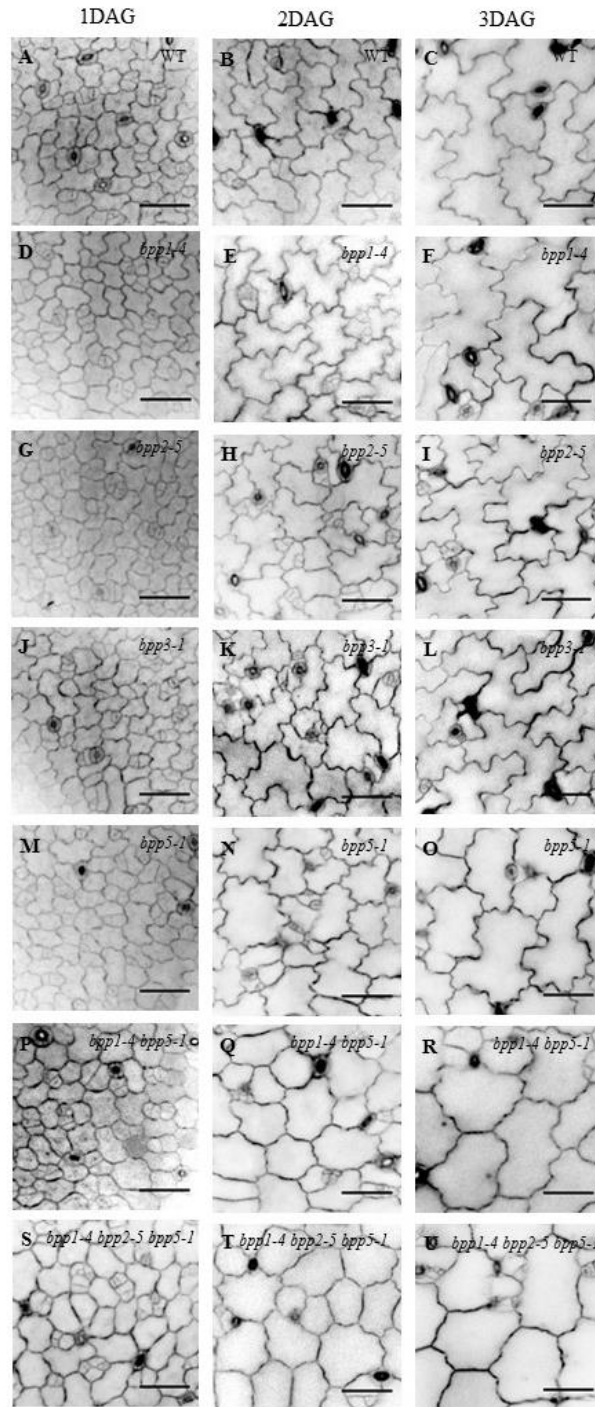


Fig. 18. Phenotypic defects of *bpp* cotyledon pavement cell shape.

Confocal microscopic imaging of PI-stained cotyledon pavement cells of WT (A-C), *bpp1-4* (D-F), *bpp2-5* (G-I), *bpp3-1* (J-L), *bpp5-1* (M-O), *bpp1-4 bpp5-1* (P-R), and *bpp1-4 bpp2-5 bpp5-1* (S-U) at 1day after germination (1DAG), 2DAG, and 3DAG. Scale bar: 10 μ m.

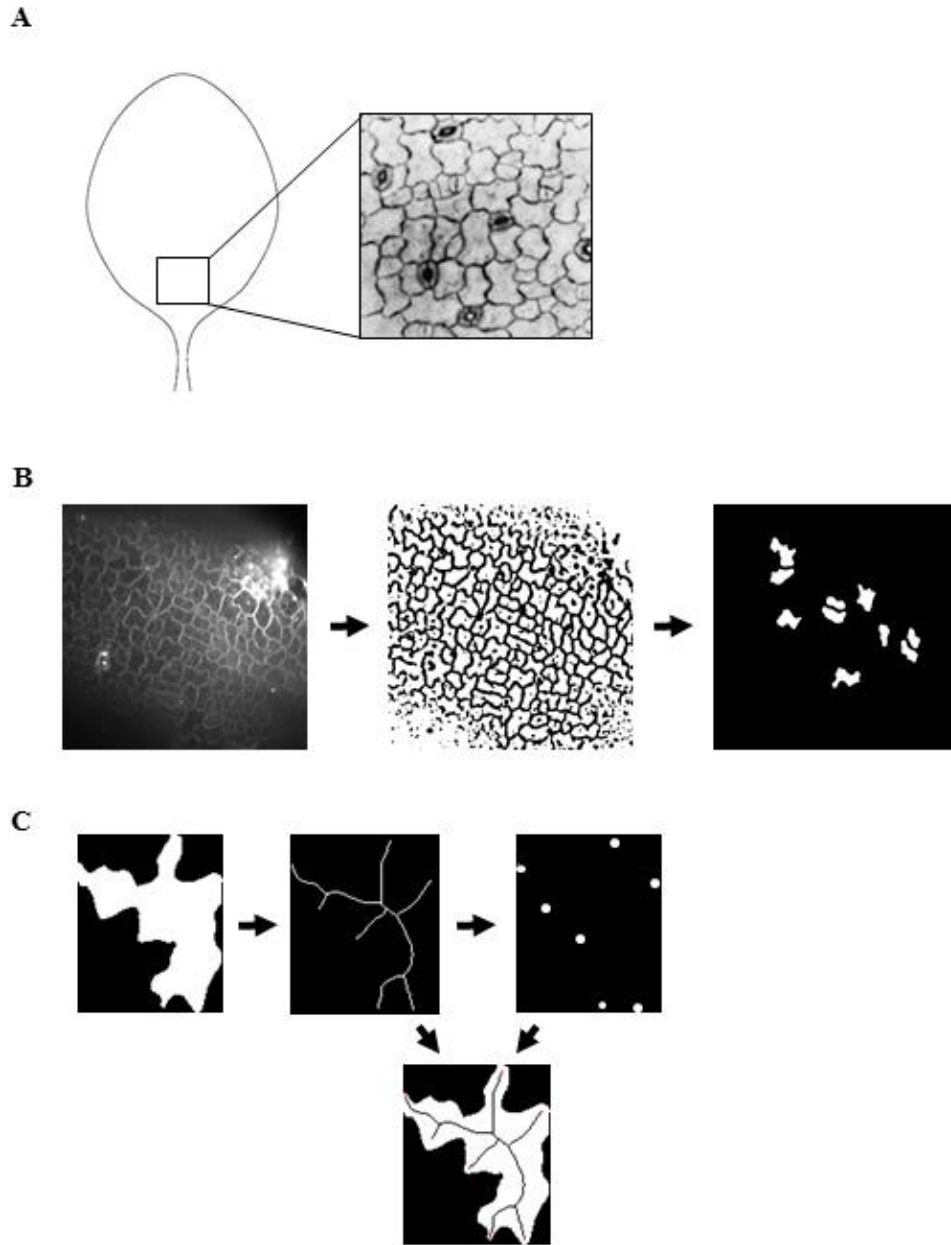


Fig. 19. Schematic representation showing procedure of cotyledon pavement cell.

(A) PI-stained pavement cells at the base of a cotyledon on day 1, 2, and 3 after germination.

(B) Imaged pavement cells were filtered through segmentation, digital outline drawing, and selection of 10 pavement cells per image.

(C) Measurement of lobe number using skeleton analysis. Outline of pavement cell was digitally drawn, then skeleton was applied to determine the ends, and finally merged image is constructed.

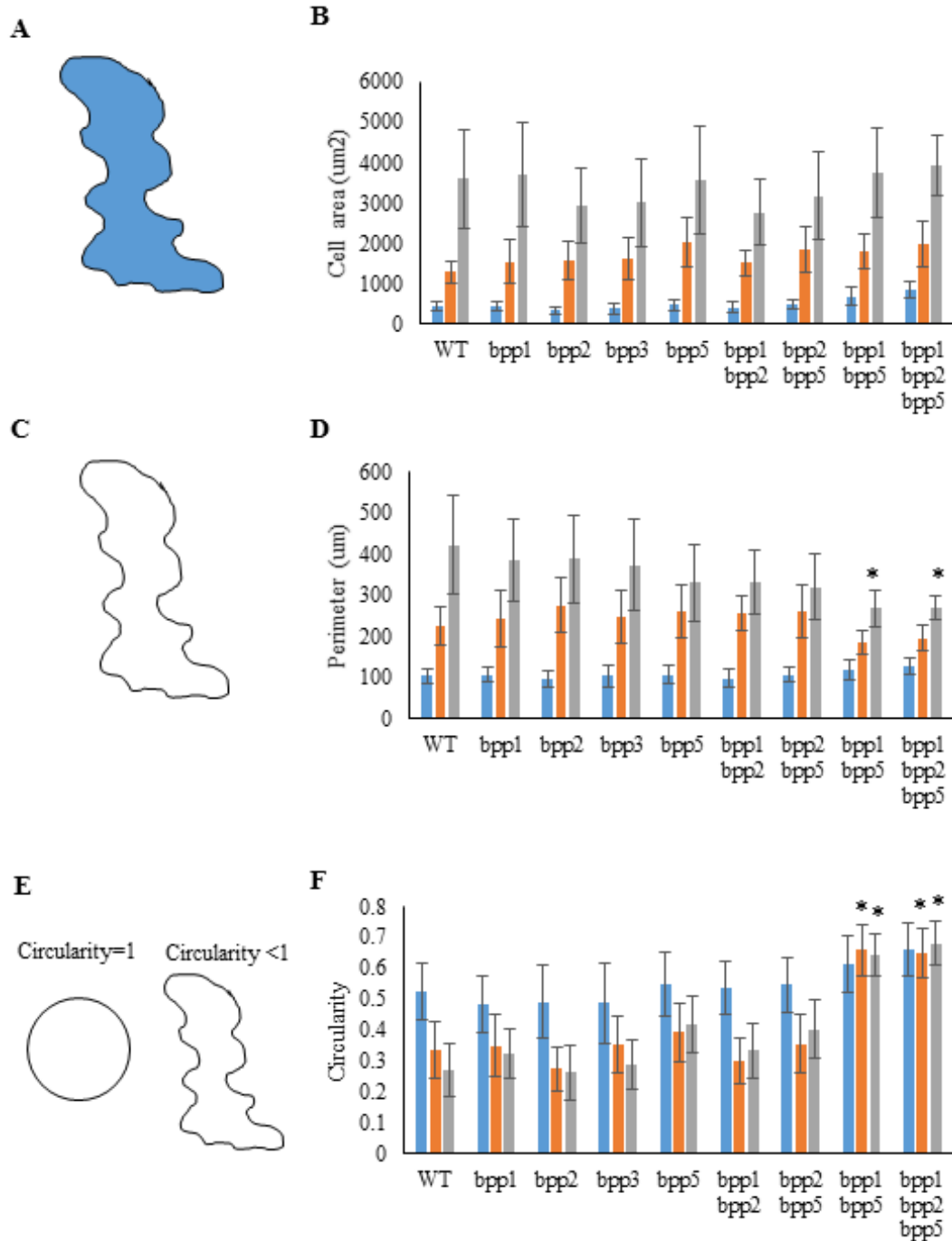


Fig. 20. Quantitative measurement of cotyledon pavement cell development.

Schematic representation of cell area (A), cell perimeter (C), and circularity (E). The mean cell area (B), perimeter (D), and circularity (F) at 1DAG (blue), 2DAG (orange), and 3DAG (grey). Statistical significant differences between WT and mutants at different time-point are denoted with asterisk (* $P < 0.05$; ** $P < 0.001$, Student's t-test). $n = 50$ cells (10 per cotyledon).

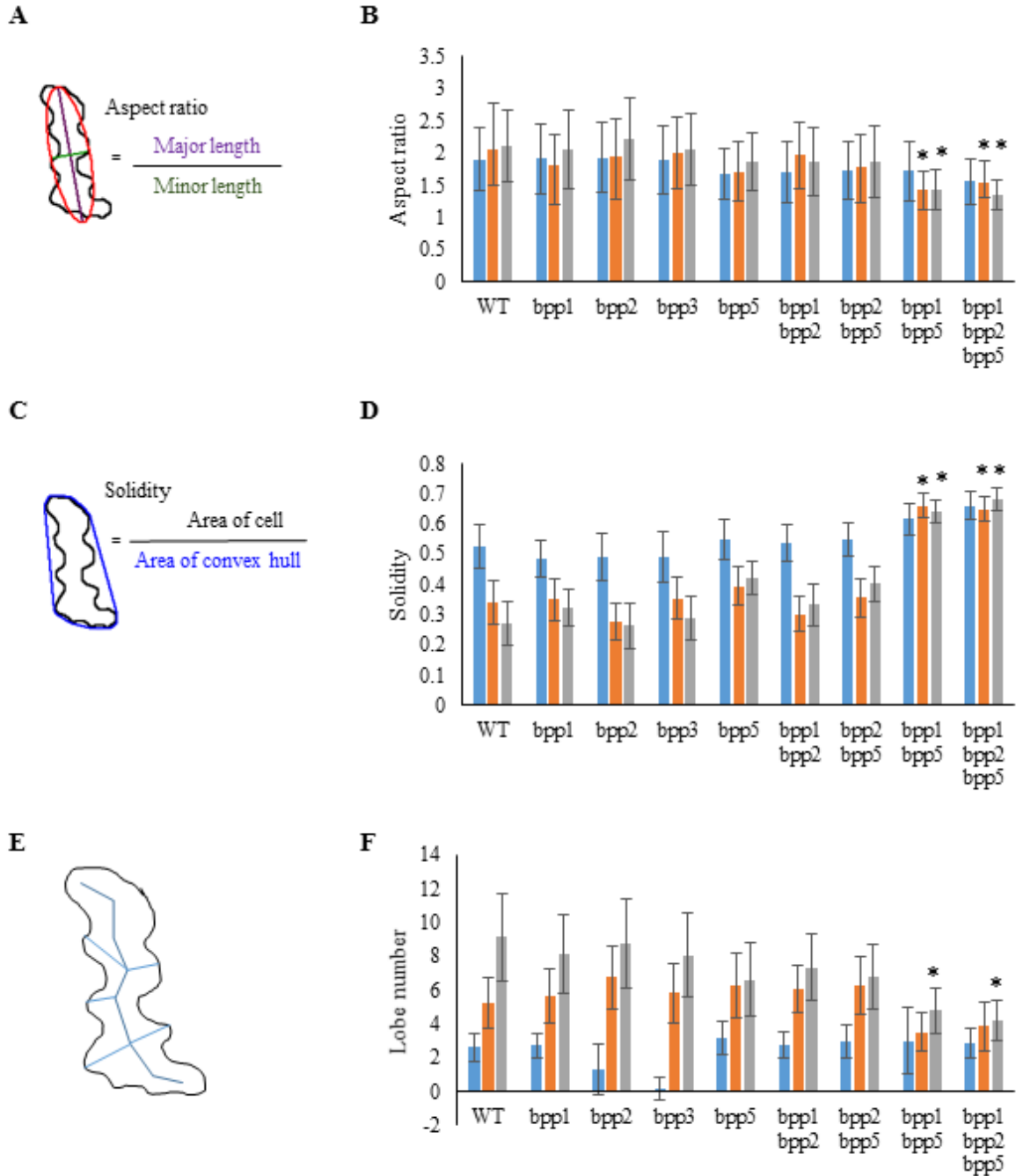


Fig. 21. Quantitative measurement of cotyledon pavement cell development.

Schematic representation of aspect ratio (A), solidity (C), and lobe number (E). The aspect ratio (B), solidity (D), and lobe number (F) at 1DAG (blue), 2DAG (orange), and 3DAG (grey). Statistical significant differences between WT and mutants at different time-point are denoted with asterisk (* $P < 0.05$; ** $P < 0.001$, Student's t-test). $n = 50$ cells (10 per cotyledon).

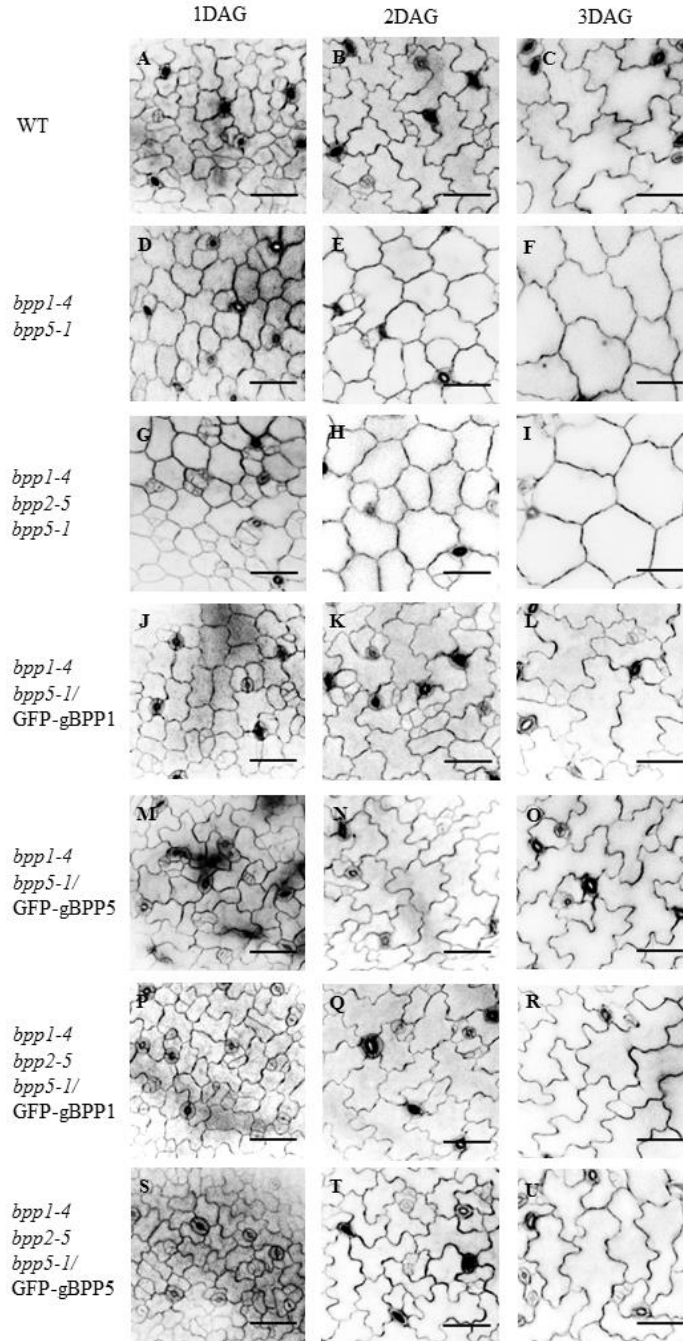


Fig. 22. Complementation of *bpp* cotyledon pavement cell shape.

Confocal microscopic imaging of PI-stained cotyledon pavement cells of WT (A-C), *bpp1-4 bpp5-1* (D-F), *bpp1-4 bpp2-5 bpp5-1* (G-I), *bpp1-4 bpp5-1*/GFP-gBPP1 (J-L), *bpp1-4 bpp5-1*/GFP-gBPP5 (M-O), *bpp1-4 bpp2-5 bpp5-1*/GFP-gBPP1 (P-R), and *bpp1-4 bpp2-5 bpp5-1*/GFP-gBPP5 (S-U) at 1DAG, 2DAG, and 3DAG. Scale bar: 10 μ m.

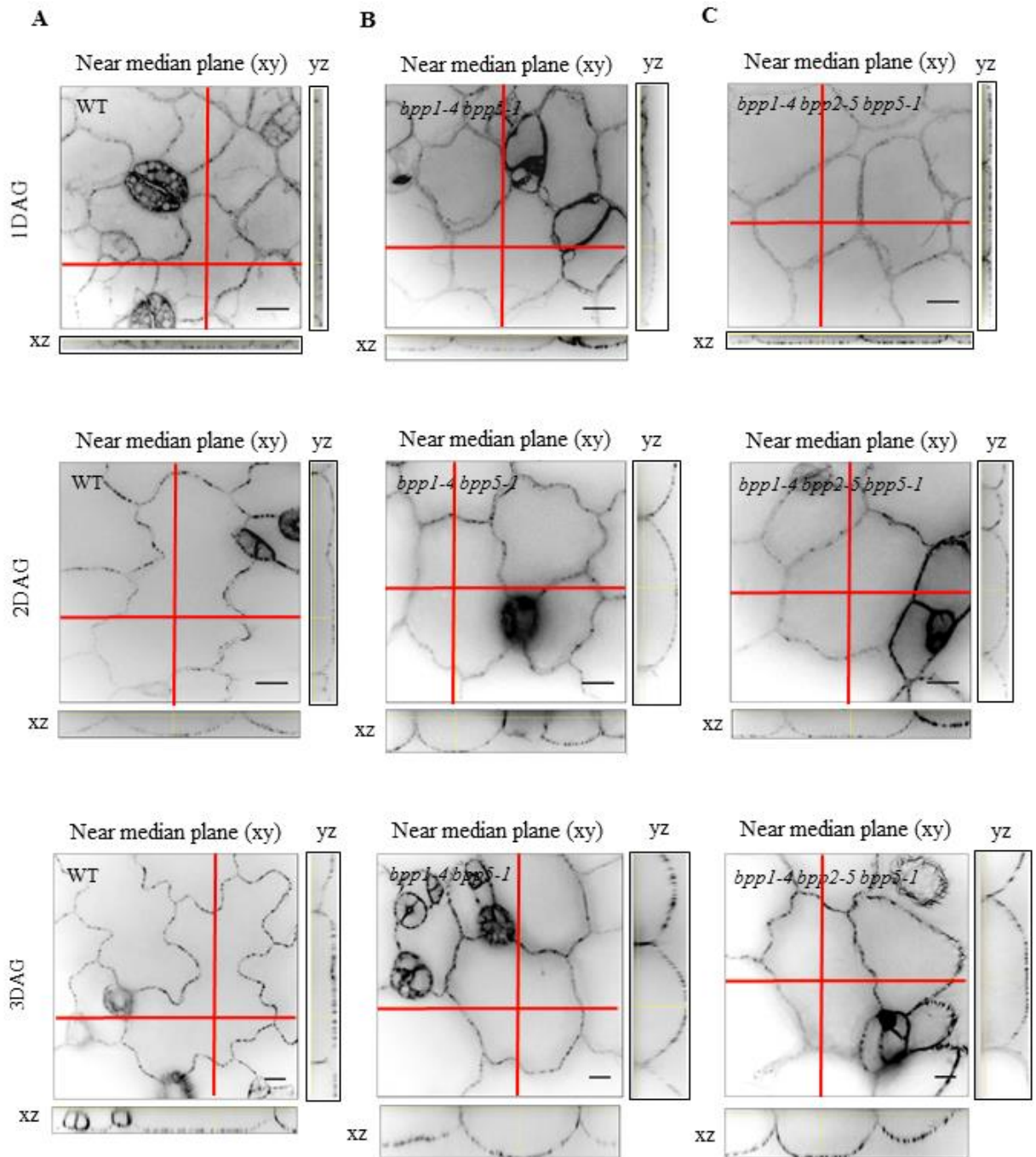


Fig. 23. Phenotypic defects in anticlinal cell expansion.

Confocal microscopic imaging of WT (A), *bpp1-4 bpp5-1* (B), and *bpp1-4 bpp2-5 bpp5-1* (C) expressing GFP-TUB6 at 1DAG, 2DAG, and 3DAG. Image of pavement cell at near median plane is shown in large box whereas orthogonal views of yz and xz are shown besides the large box respectively. Scale bar: 5 μ m.

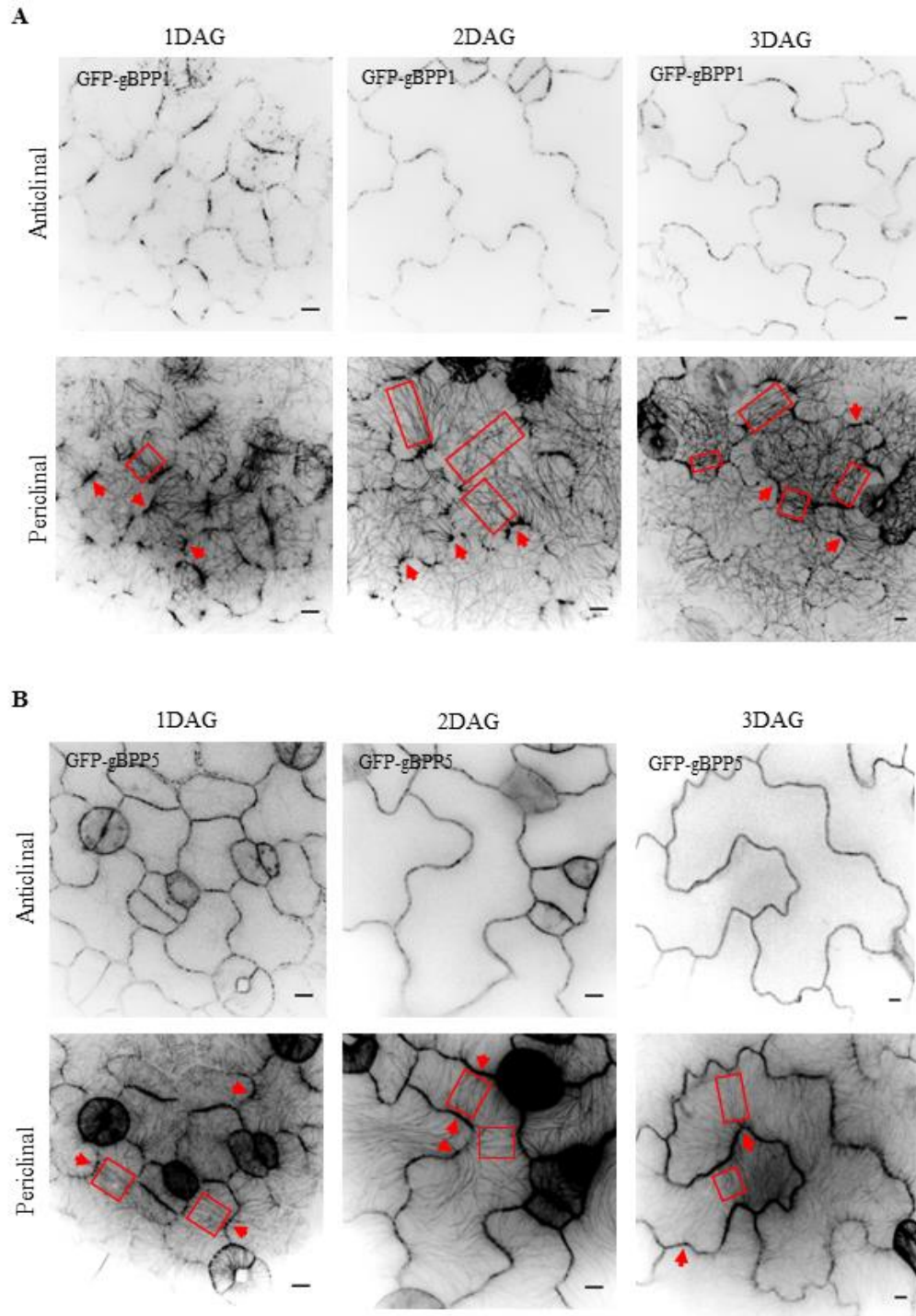


Fig. 24. GFP-gBPP1 and GFP-gBPP5 bind to cortical MTs in cotyledon pavement cells.

Z-stack projections of GFP-gBPP1 (A) in triple *bpp* mutant and GFP-gBPP5 (B) in WT binding to cortical MTs in cotyledon pavements cells at 1DAG, 2DAG and 3DAG. Red arrow indicates radiating MTs whereas red box indicates transverse MT arrays. Scale bar: 5 μm.-

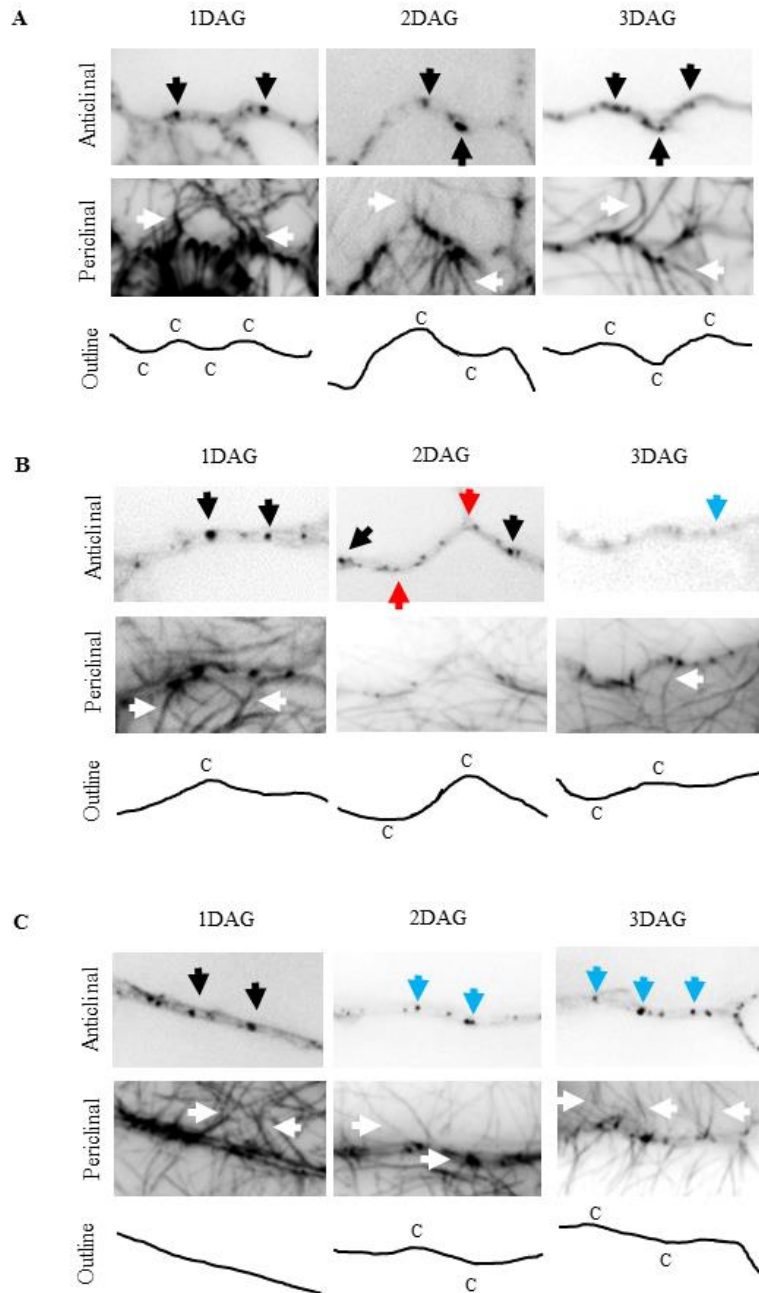


Fig. 25. Defective MT banding at convex lobes of *bpp* mutants.

MT arrays during convex lobe development of WT (A), *bpp1-4 bpp5-1* (B) and *bpp1-4 bpp2-5 bpp5-1* (C) pavement cells expressing GFP-TUB6 at 1DAG, 2DAG, and 3DAG. MTs were present as bands at the anticlinal wall surface (black arrow) and were continuous with MTs at the outer periclinal cortex region (white arrow). Lobes without MT bands (red arrow) and MT bands at flat surface (blue arrow) were present in mutants. Convex lobe is indicated by 'C' in Outline.

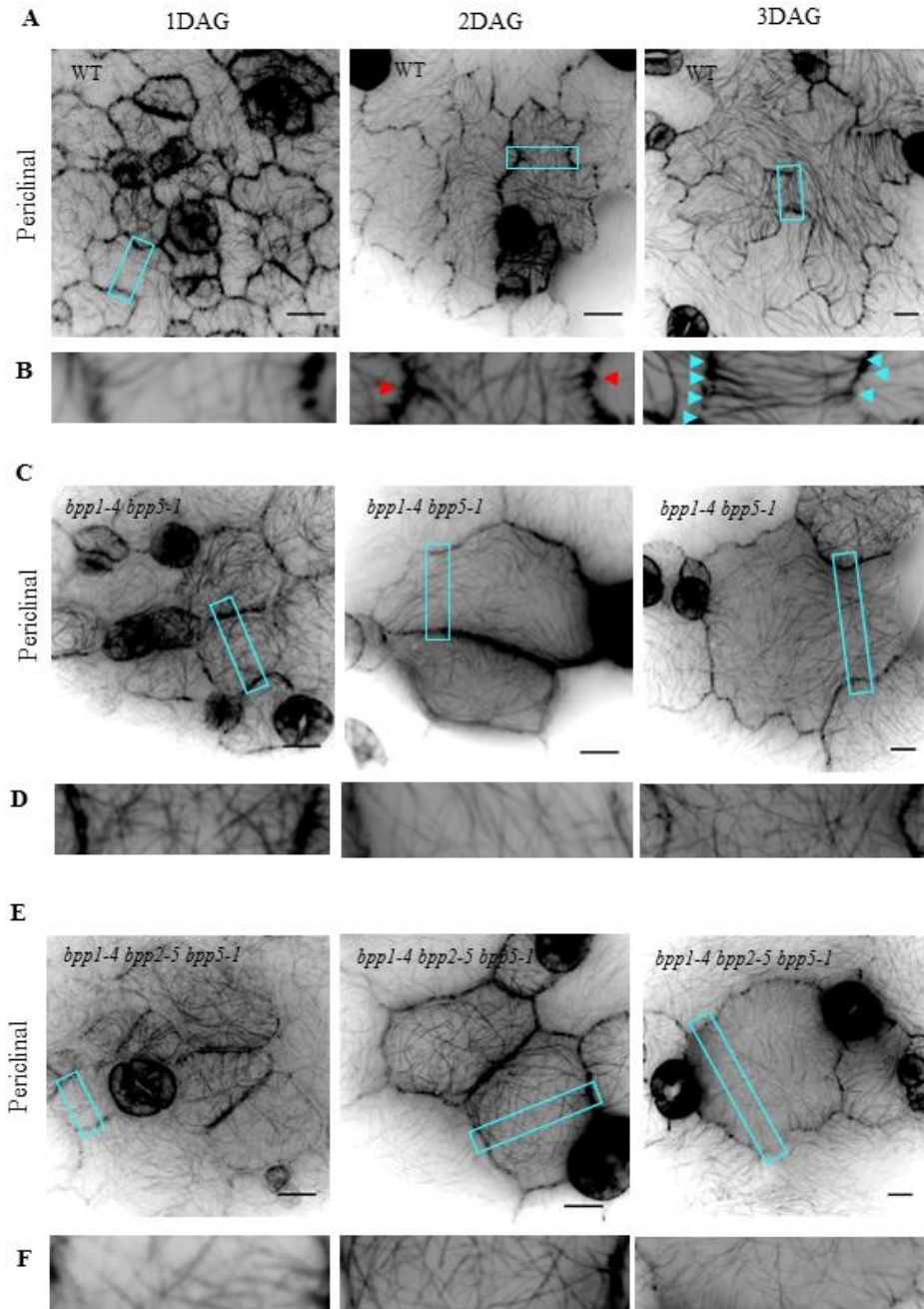


Fig. 26. Defective transverse MT array formation in *bpp* mutants between convex lobes.

Z-stack projections of WT (A), *bpp1-4 bpp5-1* (C), and *bpp1-4 bpp2-5 bpp5-1* (E) expressing GFP-TUB6 at 1DAG, 2DAG, and 3DAG are constructed from mid-plane to top plane. Enlarged region of cyan box in WT (A), *bpp1-5 bpp5-1* (C), and *bpp1-4 bpp2-5 bpp5-1* (E) is shown in (B), (D) and (F) respectively. Red arrowhead indicates radiating MT; cyan arrowhead indicates transverse MT. Scale bar: 5 μ m.

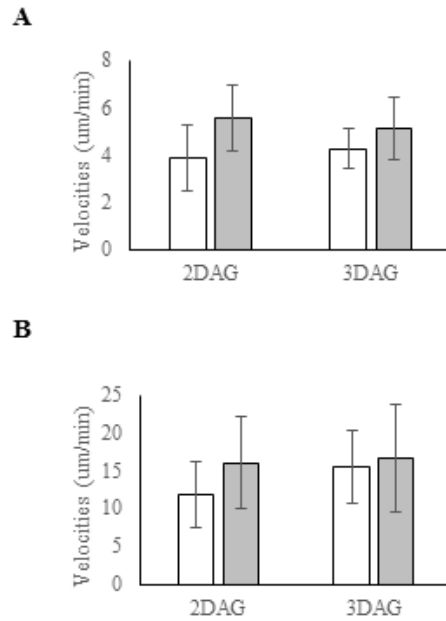


Fig. 27. Velocities of growth and shrinkage of leading end of cortical MT

(A) Mean growth velocity value of leading end at 2DAG and 3DAG. White bar indicates WT whereas grey bar indicates *bpp1-4 bpp2-5 bpp5-1*. Sample number of each bar is n = 202, n = 201, n = 246, and n = 221.

(B) Mean shrinkage velocity value of leading end at 2DAG and 3DAG. White bar indicates WT whereas grey bar indicates *bpp1-4 bpp2-5 bpp5-1*. Sample number for each bar is n = 212, n = 206, n = 206, and n = 223.

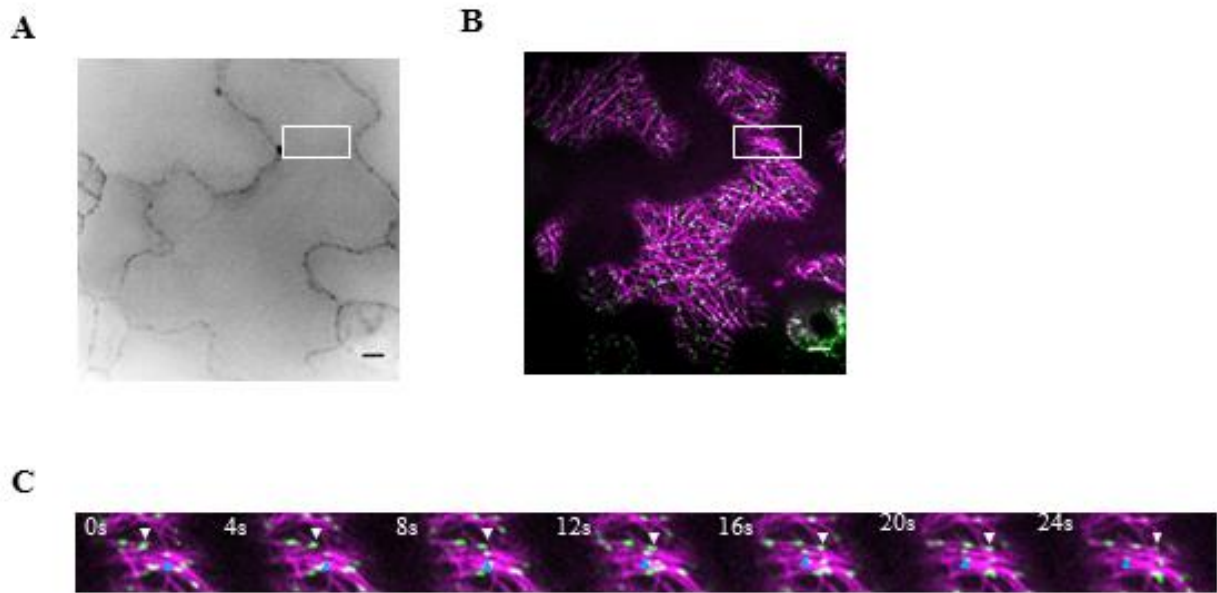


Fig. 28. Bipolarity of growing MT at the transverse array between convex lobes.

(A) Mid-plane view of pavement cells expressing mCherry-TUB6 at 2 DAG. Scale bar: 5 μ m.

(B) Top view of same cells shown in (A) expressing EB1b-GFP (green color) and mCherry-TUB6 (magenta color). Scale bar: 5 μ m.

(C) Montage of particles cropped from white box drawn in (B). White arrowhead tracks EB1b-GFP that migrates from left to right whereas cyan arrowhead tracks EB1b-GFP which migrates from right to left.

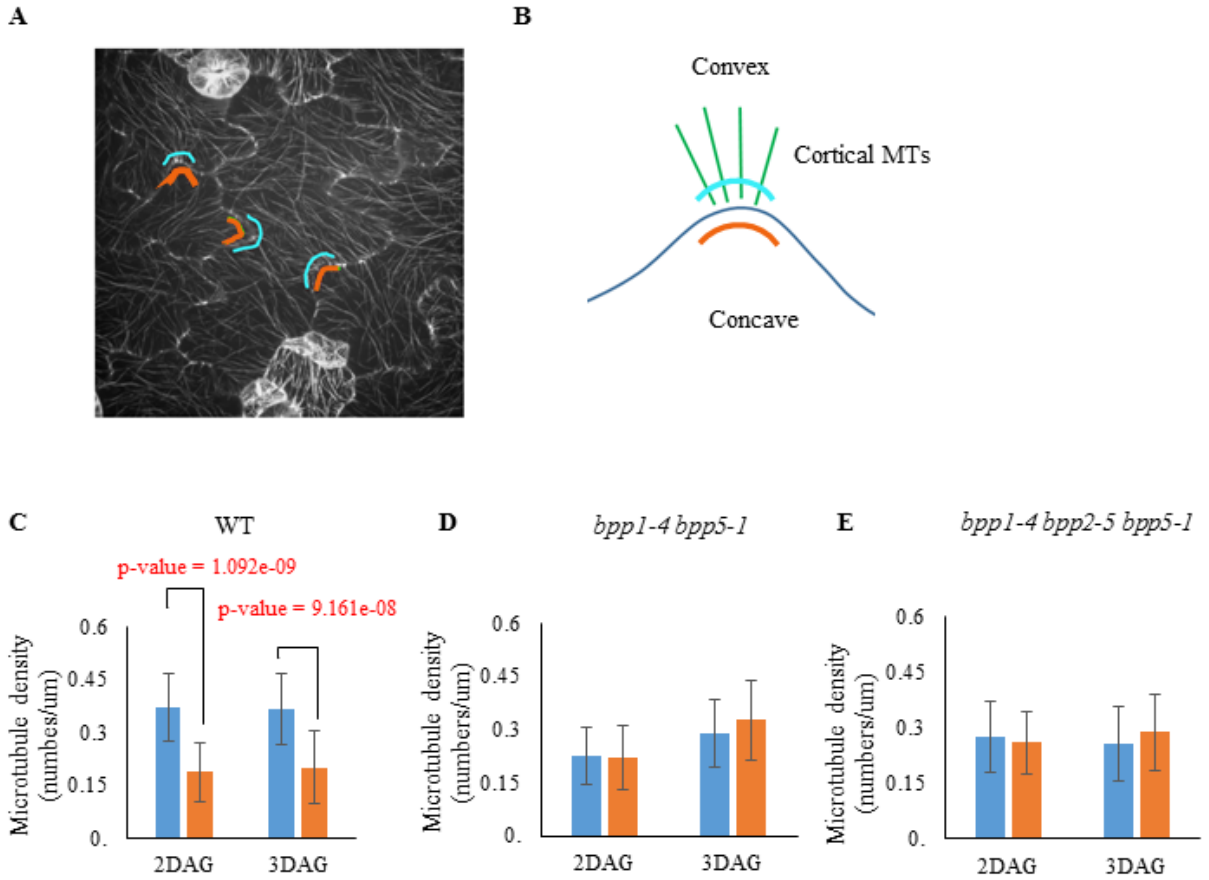


Fig. 29. MT density at periclinal surfaces of convex and concave lobes.

Representation of MT density measurement at periclinal (A), anticlinal (B), and cell center (C). Quantitative measurement of MT density at periclinal (D-F) ($n = 30$ lines from 10 cells), anticlinal (G-I) ($n = 20$ lines from 10 cells), and cell center (J) ($n = 20$ lines from 10 cells) are done at 2DAG and 3DAG respectively. White, grey and black bars indicate WT, *bpp1-4 bpp5-1*, and *bpp1-4 bpp2-5 bpp5-1* respectively.

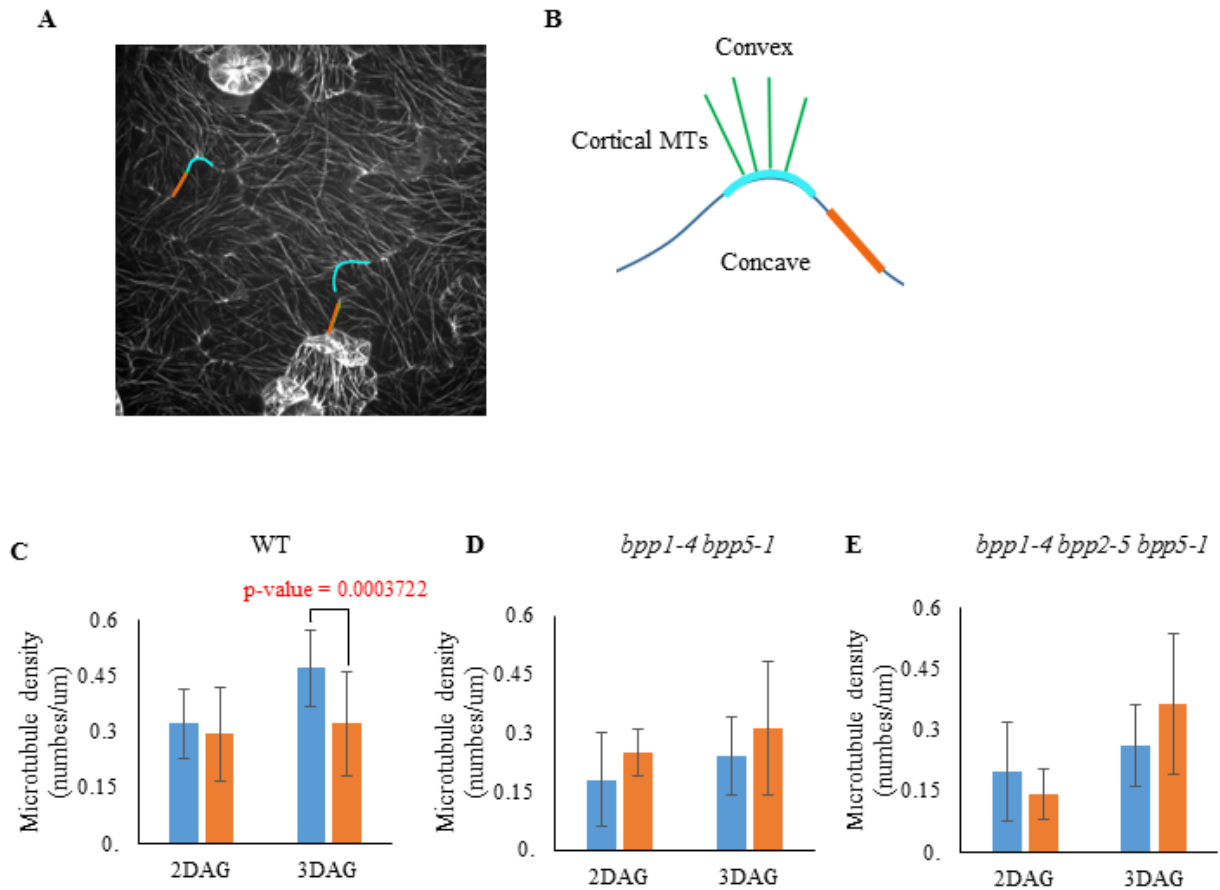
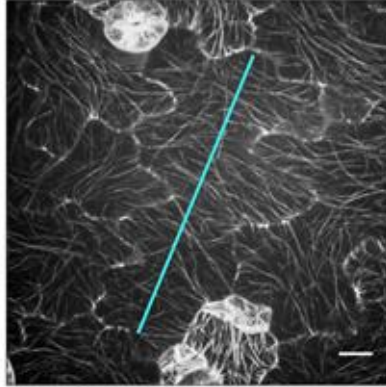


Fig. 30. MT density at anticlinal surfaces of convex lobes.

Representation of MT density measurement at periclinal (A), anticlinal (B), and cell center (C). Quantitative measurement of MT density at periclinal (D-F) (n = 30 lines from 10 cells), anticlinal (G-I) (n = 20 lines from 10 cells), and cell center (J) (n = 20 lines from 10 cells) are done at 2DAG and 3DAG respectively. White, grey and black bars indicate WT, *bpp1-4 bpp5-1*, and *bpp1-4 bpp2-5 bpp5-1* respectively.

A



B

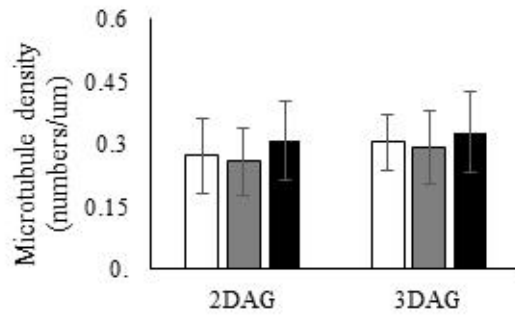


Fig. 31. Total MT at center periclinal surface.

Representation of MT density measurement at periclinal (A), anticlinal (B), and cell center (C). Quantitative measurement of MT density at periclinal (D-F) (n = 30 lines from 10 cells), anticlinal (G-I) (n = 20 lines from 10 cells), and cell center (J) (n = 20 lines from 10 cells) are done at 2DAG and 3DAG respectively. White, grey and black bars indicate WT, *bpp1-4 bpp5-1*, and *bpp1-4 bpp2-5 bpp5-1* respectively.

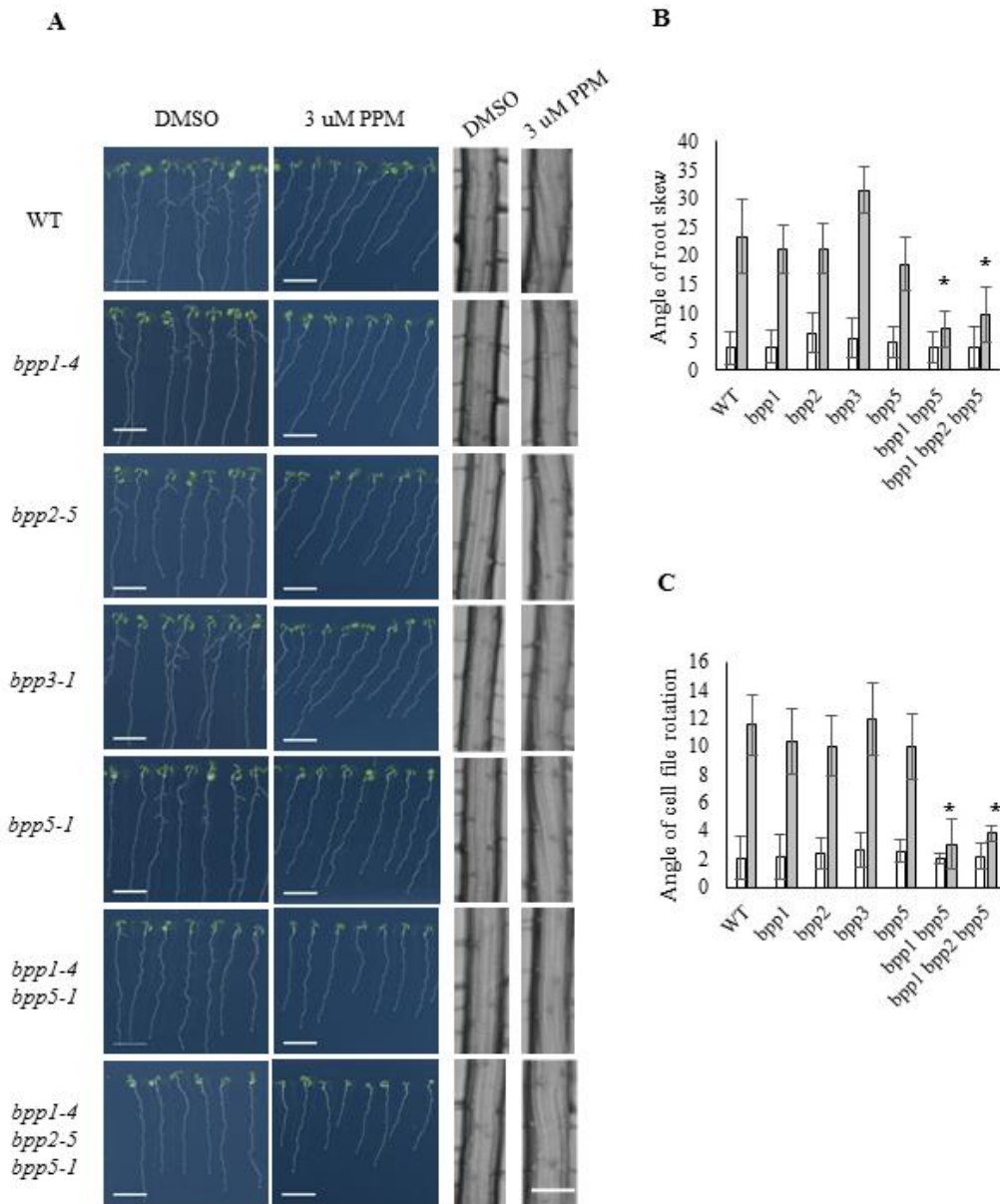


Fig. 32. Propyzamide treatment of *bpp* mutants.

(A) 7-day-old seedlings grown on Arabi media supplemented with DMSO or 3 μ M PPM and placed vertically. Images were taken from bottom and inverted. Scale bar: 1cm for seedlings; 0.1mm for enlarged root.

(B) Angle of root skew. Statistical significant differences between WT and each mutant are denoted with an asterisk ($P < 0.05$). $n = 30$ seedlings.

(C) Angle of cell file rotation. Statistical significant differences between WT and each mutant are denoted with an asterisk ($P < 0.05$). $n = 10$ seedlings.

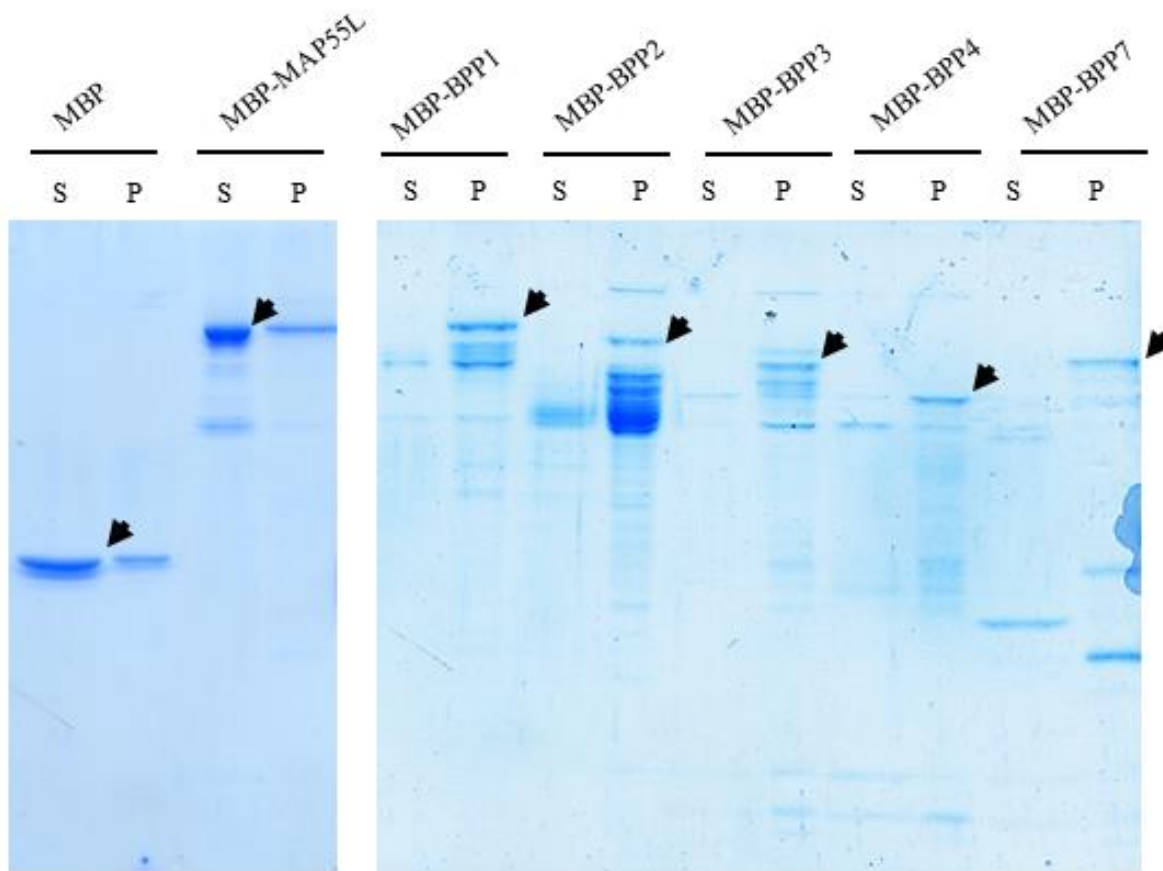


Fig. 33. Purification of recombinant BPP

SDS-PAGE of supernatant fraction (S) and pellet fraction (P) after ultracentrifugation.

MBP and MBP-MAP55L are controls which mainly do not form aggregates that precipitated in pellet fraction after ultracentrifugation. Black arrow indicates the position of major portion of each recombinant protein.

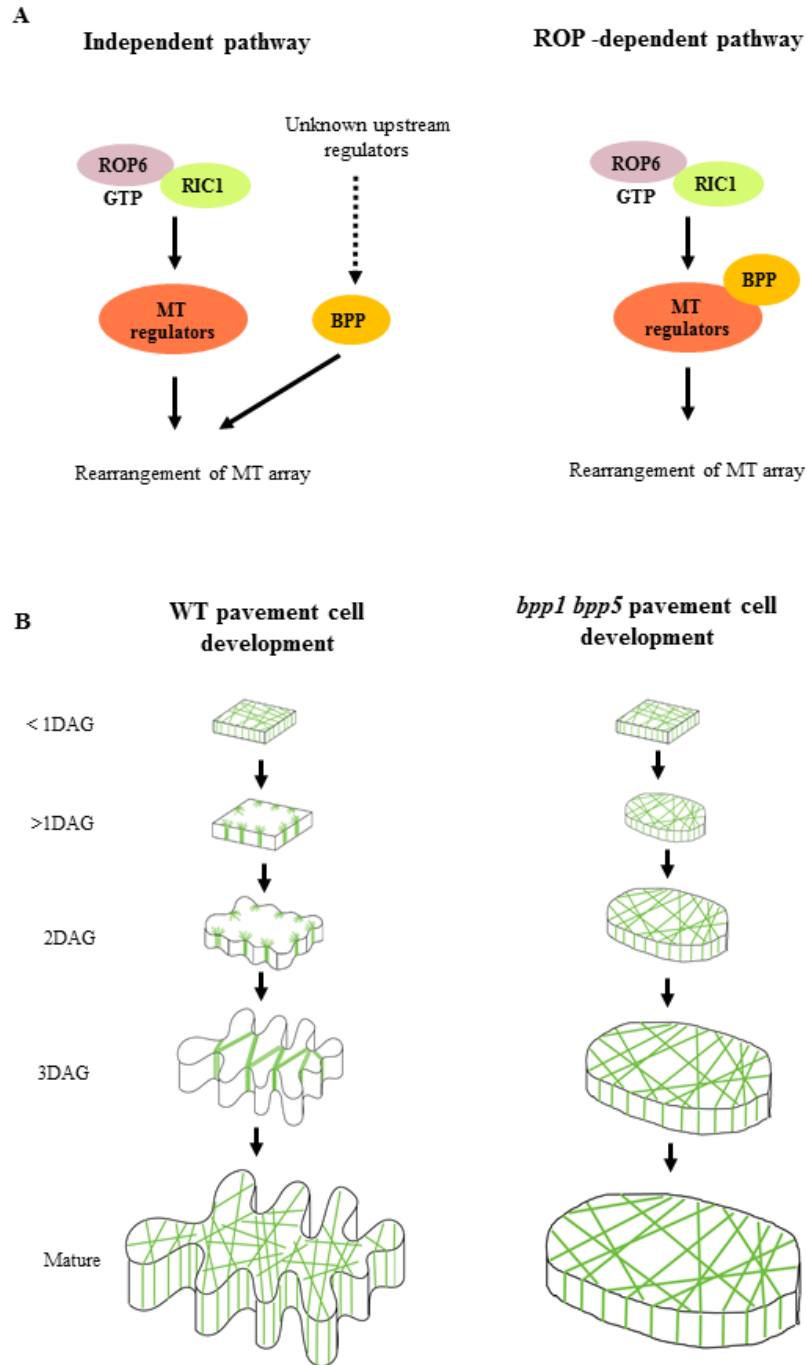


Fig. 34. Summary of BPP physiological function

(A) Physiological function of BPP might be regulated by either ROP-independent or ROP-dependent signaling pathway.

(B) BPP1 and BPP5 proteins are required for radiating and transverse MT array at specific developmental stages. Loss of these proteins results in abnormal pavement cell shape.

Table 2. List of primers used in this study

Name	Sequence (5'-3')	Experiment
BPP1_1D	GGATCCATGAATCGAAGTTTTAGGGC	Amplifying cDNA of BPP1 with restriction site
BPP1_2780U	GGCTCTCCCTTGTAAGCTTGCAG	Amplifying cDNA of BPP1
BPP2_1D	GGATCCATGTTGACCCACGACAGAGATG	Amplifying cDNA of BPP2 with restriction site
BPP2_2310U	GGCAGATGTGAACTTGGGGTACTG	Amplifying cDNA of BPP2
BPP3_1D	GGATCCATGTTGACCCAAAACAAAGATG	Amplifying cDNA of BPP3 with restriction site
BPP3_2244U	GGCAGAGCAACTCATGTCGCTG	Amplifying cDNA of BPP3
BPP4_1D	GGATCCATGGAGAATGTGGTGGTGGTTC	Amplifying cDNA of BPP4 with restriction site
BPP4_1819U	GGCCGATGACTCGTTTTTGTC	Amplifying cDNA of BPP4
BPP5_1D	GGATCCATGCCTCCTTCCCCTGGCA	Amplifying cDNA of BPP5 with restriction site
BPP5_4434U	GGCCATTATTGAGCAATTGCATTTGG	Amplifying cDNA of BPP5
BPP6_1D	GGATCCATGAATAGGAATCTCAGAGAATC	Amplifying cDNA of BPP6 with restriction site
BPP6_2588U	GGCTAGTGGGGCAAATGGCTCTG	Amplifying cDNA of BPP6
BPP7_1D	GGATCCATGAGTGATCGGAGTCTGAAAAAG	Amplifying cDNA of BPP7 with restriction site
BPP7_1866U	GGCGAGAGGAGAGAATAGATCAGG	Amplifying cDNA of BPP7
BPP1_proF	CAAAAAAGCAGGCTTCTTGTAACCTTCTGTACCTTATATT	Amplifying BPP1 promoter with attB1
BPP1_proR	CAAGAAAGCTGGGTCTGCTCACCAAACCTTACAACAGATC	Amplifying BPP1 promoter with attB2
BPP2_proF	CAAAAAAGCAGGCTTCAGTGTGGTTTATTTCTCTGTTCAAT	Amplifying BPP2 promoter with attB1
BPP2_proR	CAAGAAAGCTGGGTCTGACGAAAGCTGAGATTGAAATTTT	Amplifying BPP2 promoter with attB2
BPP3_proF	CAAAAAAGCAGGCTTCTTTATTTTCGTGATAAAAAGTGTATA	Amplifying BPP3 promoter with attB1
BPP3_proR	CAAGAAAGCTGGGTCCGCCGTCGTACTIONACTAGTATTATCA	Amplifying BPP3 promoter with attB2
BPP4_proF	CAAAAAAGCAGGCTTCGTATGATGACGATGTGGAGCAAGAA	Amplifying BPP4 promoter with attB1

Table 2. (cont.)

Name	Sequence (5'-3')	Experiment
BPP4_proR	CAAGAAAGCTGGGTCTTCTCAAAACCTCTTCGTTGTAATA	Amplifying BPP4 promoter with attB2
BPP5_proF	CAAAAAAGCAGGCTTCTGGAACATACATTTGTCAACTAACA	Amplifying BPP5 promoter with attB1
BPP5_proR	CAAGAAAGCTGGGTCTCTACTGTCCTAACTACTGAAGAC	Amplifying BPP5 promoter with attB2
BPP6_proF	CAAAAAAGCAGGCTTCTGTTGCGGGTGACTCATTGTTGTT	Amplifying BPP6 promoter with attB1
BPP6_proR	CAAGAAAGCTGGGTCTGTCTCGGAGGAAAGAGAGAGAGAGCA	Amplifying BPP6 promoter with attB2
BPP7_proF	CAAAAAAGCAGGCTTCTACTAGTTAAATTTTCCTTGACTT	Amplifying BPP7 promoter with attB1
BPP7_proR	CAAGAAAGCTGGGTCCGACGGTTTTAAAAACACACGATCAA	Amplifying BPP7 promoter with attB2
attB1 adapter	GGGGACAAGTTTGTACAAAAAGCAGGCT	Amplifying attB1 site
attB2 adapter	GGGGACCACTTTGTACAAGAAAGCTGGGT	Amplifying attB2 site
BP	CCCGTCTCACTGGTGAAAAG	Amplifying left border of T-DNA
LP	GGTGTTTCATCATTCCAGCATC	Genotyping of <i>bpp1-1</i>
RP	TGCAGCAGACTCTGTTGAGG	Genotyping of <i>bpp1-1</i>
LP2	CGTCAGACATGCCTGGTTTC	Genotyping of <i>bpp1-3</i>
RP2	TCTCCCTTGTAAGCTTGCAG	Genotyping of <i>bpp1-3</i>
LP3	CTTTGTTTGTGAGGTGTGC	Genotyping of <i>bpp1-4</i>
RP3	GCAATAACATTCTTACTCTGG	Genotyping of <i>bpp1-4</i>
LP4	GAATCTGAGGACGACTTTAGC	Genotyping of <i>bpp2-5</i>
RP4	GTTTCCTCATGTTCACTC	Genotyping of <i>bpp2-5</i>
LP5	CACTTTTATTGATGTTACATATCTC	Genotyping of <i>bpp3-1</i>
RP5	CTCGGACTCTTCTTTGCTATAG	Genotyping of <i>bpp3-1</i>
LP6	ATGTTGACCCAAAACAAAGATG	Genotyping of <i>bpp3-2</i>
RP6	CAGACTTTTAGAGAGCATGATC	Genotyping of <i>bpp3-2</i>
LP7	CTGTATTCCAGTCTGAAGTTG	Genotyping of <i>bpp5-1</i>
RP7	CCCTGGAAATAGAACTCTCG	Genotyping of <i>bpp5-1</i>
LP8	GATCTGGCAGAGCATAATCC	Genotyping of <i>bpp5-2</i>
RP9	CTCTGGAATCTCATCATGAAC	Genotyping of <i>bpp5-2</i>
BPP1_1974D	CAGTGAGGTCAAGACCATGG	RT-PCR of <i>BPP1</i>
BPP1_2783U	TCATCTCCCTTGTAAGCTTGC	RT-PCR of <i>BPP1</i>

Table 2. (cont.)

Name	Sequence (5'-3')	Experiment
BPP2_3D	GTTGACCCACGACAGAGATG	RT-PCR of <i>BPP2</i>
BPP2_2310U	AGATGTGAACTTGGGGTACTG	RT-PCR of <i>BPP2</i>
BPP3_1063D	CTCCACGCCAACCAGAAAG	RT-PCR of <i>BPP3</i>
BPP3_858R	TTCTGTGGACGCTGATCTTG	RT-PCR of <i>BPP3</i>
BPP4_4D	GAGAATGTGGTGGTGGTTCG	RT-PCR of <i>BPP4</i>
BPP4_1819U	CGATGACTCGTTTTTGTC	RT-PCR of <i>BPP4</i>
BPP5_1006D	GCAGCAGATAAGGGGAAGAC	RT-PCR of <i>BPP5</i>
BPP5_2354U	CCATATCACCAAGCTGATCAC	RT-PCR of <i>BPP5</i>
BPP6_1D	ATGAATAGGAATCTCAGAGAATC	RT-PCR of <i>BPP6</i>
BPP6_1502U	GGATGAACTAGATGACCCTGG	RT-PCR of <i>BPP6</i>
BPP7_1151D	GTCACTCTAGCGTTTGGTAG	RT-PCR of <i>BPP7</i>
BPP7_1866U	GAGAGGAGAGAATAGATCAGG	RT-PCR of <i>BPP7</i>
RTActin8F	ACATTGTGCTCAGTGGTGGT	RT-PCR of <i>Actin</i>
RTActin8R	CCTGGACCTGCTTCATCATA	RT-PCR of <i>Actin</i>

Discussion

In this study, direct binding of BPP proteins to MTs and the effects of such association on MT behaviors *in vitro* have not been examined. Although recombinant proteins of BPP1, BPP2, BPP3, BPP4, and BPP7 could be expressed in *E. coli* and purified to some extent, these proteins were highly degradable and tended to form aggregates that precipitated under high-speed centrifugation (**Fig. 33**). Preparation of soluble and pure recombinant BPP proteins is essential for characterization of their biochemical functions.

Based on the phenotypic studies of *bpp* mutants, BPP1 and BPP5 are the most important members of all whereas BPP2 has a moderate role. Different combinations of double mutants and triple mutants of these three members resulted in plants with stunted organ development, where overall aerial parts are shorter. Apart from the role of BPPs in anisotropic growth of axial organs, BPP1 and BPP5 are also important for the lobe formation of pavement cells. In the simultaneous absence of BPP1 and BPP5, the mutant pavement cells lose the proper orchestration of alternating protrusions and growth restriction sites along the anticlinal walls, leading to more spherical cell expansion. This abnormal anticlinal cell expansion causes mutant pavement cells to develop smaller or no lobes, hence reducing the jigsaw puzzle-like pattern. The interlocking anticlinal walls is important as it increases contact area between neighboring cells which in turn provide additional adhesive strength and stability.

The lack of inter-digitation in *bpp1 bpp5* and *bpp1 bpp2 bpp5* pavement cells is due to abnormal MT arrays in early lobe development (**Fig. 34B**). MT polymerization still occurs at the anticlinal walls, but the density of MT bands at convex lobe is obviously lower, leading to smaller lobe formation. Alternating MT-rich regions on the convex lobe and MT-free region on the concave lobe which persists during growth have been observed by time-lapse imaging of early lobe development (Panteris and Galatis, 2005; Armour *et al.*, 2015). The CLASP MAP is reported to facilitate the spanning of MTs between the outer periclinal and anticlinal faces of a cell (Ambrose *et al.*, 2011). As the spanning of MTs between different cell surfaces was not compromised in *bpp* mutants, it is unlikely that BPP1 and BPP5 work with CLASP. One possible role of BPP1 and BPP5 is promoting the cross-linking of MTs at both anticlinal and periclinal walls at the convex lobes through the association with MT-bundling MAPs. They might not be directly responsible in

cross-linking of MTs, but rather marking the site where the MAPs should concentrate for high MT-bundling activity. Known MAPs responsible for bundling MTs include the MAP65 family proteins, which are the homologs of ANAPHASE SPINDLE ELONGATION (Ase1) from fission yeast and PROTEIN REQUIRED FOR CYTOKINESIS 1 (PRC1) in mammals (Chang-Jie and Sonobe, 1993; Daga *et al.*, 2006; Lucas *et al.*, 2011). Arabidopsis MAP65-3 is known to bind antiparallel MTs in the phragmoplast structure during mitotic division (Ho *et al.*, 2011). It is not known whether MT bundling is important for the lobe formation and whether MAP65 family proteins are involved in this process. Another possible role of BPP1 and BPP5 is the facilitation of localized transverse MT array at the outer periclinal wall of convex lobes. This is proposed as the MT angle between WT convex lobes favors the angle perpendicular to the major growth axis of the pavement cell.

Given the localization of BPP1 and BPP5 on whole cortical MTs, they may regulate MT dynamics. They might have redundancy with other MAPs in regulating MT dynamics as growth and shrinkage velocities were insignificant between WT and *bpp* triple mutant. MT dynamics is essential for pavement cell development as it is a prerequisite for direct cortical MT array initiation and extension. Alternatively, BPP1 and BPP5 might be associated with other MAPs with specific MT regulating functions. Severing of MT from the nucleation site (Nakamura *et al.*, 2010) and at the MT-MT intersection is catalyzed by KATANIN, and may be important for the complex cell shape of pavement cells (Burk *et al.*, 2001). Arabidopsis MAP18 (MICROTUBULE-ASSOCIATED PROTEIN 18), which functions in destabilizing cortical MTs, has underdeveloped lobes in the pavement cells (Wang *et al.*, 2007). Other MAPs with unknown functions, such as ANGUSTIFULIA (AN), may have some roles in the proper formation of the inter-digitated cell shape of the pavement cells, as their mutant phenotype imply (Kim *et al.*, 2002).

Chapter 2: MAP55 and MAP55L

Introduction

Dynamics of single MTs and assembly of MTs into complex organization are regulated by various microtubule-associated proteins (MAPs). Classically, the terminology of MAPs referred to proteins co-purified with MTs from cell extracts (Lloyd and Hussey, 2001). Nowadays, MAPs generally refer to proteins with ability to bind MTs directly or indirectly. Particular MAPs that track the growing plus end of MTs are designated as the plus tip- tracking proteins (+TIPs). These +TIPs either have intrinsic properties to accumulate at the growing plus-end directly or associate with other bona fide +TIPs that carry them to the MT end (Akhmanova and Steinmetz, 2008). One famous example of the former type is the evolutionarily conserved END-BINDING 1 (EB1), which tracks the growing MT plus end by recognizing the GTP cap through its calponin-homology domain (Maurer *et al.*, 2012; Alushin *et al.*, 2014). In animal cells, EB1 functions as a central adaptor that pulls various +TIPs of the latter group to the MT plus end through the conserved Ser-x-Ile-Pro (SxIP) interaction motif (Kumar and Wittmann, 2012; Jiang *et al.*, 2012). Knock down or deletion of EB1s severely impairs MT functions and is lethal in some non-plant eukaryotes (Duelberg *et al.*, 2013). However, such severe phenotypic defect is not detected in plants. For example, *Arabidopsis ebl* mutants in which all three EB1 genes were mutated only mildly-affected alignment of spindle and phragmoplast MTs, which recovered to wild-type alignment later in the mitosis (Komaki *et al.*, 2009). Hence, EB1 may not serve as a central hub in recruiting various +TIPs in plants, and other plant-specific +TIPS may play more important roles in plant cells.

SPIRAL1 (SPR1) is a founding plant-specific +TIP and constitutes a family of six members in *Arabidopsis* (Nakajima *et al.*, 2004; Nakajima *et al.*, 2006; Sedbrook *et al.*, 2004). In vivo, *Arabidopsis* SPR1 binds to the MT lattice and also accumulates at the growing MT plus end. It has been reported that SPR1 binds MTs directly and interacts with EB1 in *Arabidopsis* cells (Galva *et al.*, 2014). Single *Arabidopsis spr1* mutant exhibited right-handed helical growth in rapidly elongating axial organs, and this phenotype was further enhanced in the *spr1 eblb* double mutant. The MT dynamics of hypocotyl cells in the *spr1 eblb* mutant were also severely affected. The association of SPR1 and EB1b is proposed to be important for the MT dynamics in response to directional cues, ensuring proper directional cell expansion and organ development. However, it

is still not known how their association at the growing plus end is correlated to directional cell growth.

In this chapter, I studied the MAP55 and its homolog MAP55L, which both share approximately 40% of protein similarity. MAP55L has been shown to bind cortical MTs when expressed transiently in onion epidermal cells (Hamada *et al.*, 2013), but detailed characterization of MAP55 and its homologs has not been reported. Therefore, my work focused on characterization of this MAP family.

Materials and methods

Vector construction

For visualization of GFP-tagged protein in Arabidopsis, *MAP55* cDNA and *MAP55L* gene were cloned into pGWB5 and pGWB4 respectively using the Gateway Cloning system (Invitrogen). For dual color visualization of fusion proteins and a MT marker, transgenic Arabidopsis harboring a desired GFP-tagged protein was crossed with either the plant harboring pUB10::mCherry-TUB6, AtML::mCherry-TUB6 or WRKY::mCherry-TUB6, depending on the specific tissue regions for microscopic observation. To visualize GFP-MAP55 overlapping with EB1b-mCherry, a plant expressing GFP-MAP55 was crossed with a plant expressing EB1b-mCherry. For promoter-GUS assays, a 2.5-kb promoter region and a *MAP55L* gene region just before the stop codon were cloned into pGWB3 using the Gateway Cloning system.

Transient expression vectors for the particle bombardment assay was constructed by fusing a desired cDNA fragment with GFP at the C-terminus using the Gateway Cloning system. MT binding regions were investigated by expressing truncated *MAP55* or *MAP55L* cDNAs with or without basic regions. The ATG start codon was included before the N-terminus of a truncated cDNA.

Recombinant protein purification and MT co-sedimentation assay

To produce maltose binding protein (MBP) fused *MAP55* and MBP-*MAP55L* respectively, the full-length cDNA of each protein were cloned into pCold-MBP vector by utilizing appropriate restriction enzyme cleavage sites (Hayashi and Kojima, 2010). The recombinant proteins were produced in the Rosetta (DE3) strain. The fusion proteins were harvested and purified using an amylose resin column according to the manufacturer's instructions (New England BioLabs). Purified fusion proteins were concentrated and the buffer was changed with BRB80 (80 mM Pipes, 1 mM MgCl₂, 1 mM EGTA, pH 6.8). Final protein preparations were frozen with liquid nitrogen and stored at -80°C.

For MT co-sedimentation assay, thawed fusion proteins were centrifuged at 100,000 x g for 15 min at 4°C to remove protein aggregates. MTs were polymerized using bovine brain tubulins in

1x BRB80 supplemented with 1 mM GTP and with gradual concentrations of taxol. The tubulin were incubated at 37°C for 35 min to induce MT polymerization. Polymerized MTs were separated from free tubulin by centrifugation at 100,000 x g for 30 min at 30°C. Precipitated MTs were suspended in 1x BRB80 supplemented with 10 µM taxol. 1 µM of MBP-MAP55 or MBP-MAP55L was mixed with 1 µM MTs in a 50-µL reaction volume containing 1xBRB80 buffer and 10 µM taxol and incubated at room temperature for 1h. Negative controls were MBP, MBP-MAP55 and MBP-MAP55L in each reaction without the presence of MTs. After 1h incubation, the samples were centrifuged at 100,000 x g for 30 min at 30°C. The pellet and supernatant fractions were mixed with SDS-PAGE sample buffer and analyzed by SDS-PAGE, followed by Coomassie Blue Staining.

Particle bombardment-mediated transient transformation

A plasmid harboring a desired region of MAP55 or MAP55L (2 µg) and the tagRFP-MAP4 MT marker plasmid (2 µg) were mixed with 1.5 mg of 1.0 µm gold particles suspended in 19.2% glycerol, 962 mM CaCl₂ and 1.5% spermidine for 30 min, washed with 70% ethanol then 100% ethanol, and finally co-bombarded into onion (*Allium cepa*) epidermal peels using PDS-1000/ He Biolistic Particle Delivery System (Bio-Rad) equipped with 1,100-p.s.i rupture disks. After 16h dark incubation on a moist petri dish, the cells were observed with a Nikon D-ECLIPSE C2 confocal microscope. GFP signal was excited at 488 nm while tagRFP signal at 543 nm using an ET514/30 and ET585/65 band-pass emission filter respectively.

Visualization of MTs with confocal spinning-disc microscopy

Time-lapse imaging of fluorescent protein localization onto MTs was performed on spinning disk confocal microscope with adaptive focus and a Nikon Apo TIRF 60x/1.49 numerical aperture oil-immersion objective. Excitation energy was supplied by either 488 nm laser or 561 nm laser (Andor). Images were acquired at 2-s intervals for 151 repeats during interphase or 30-s intervals for 151 repeats during mitotic division. Trajectories of individual MTs were traced on images and converted into kymographs using tools in ImageJ.

Results

Determination of MT-binding regions

The Arabidopsis MAP55 has its homolog MAP55L share approximately 40% protein similarity. Both proteins have several regions rich in basic amino acids, especially at the C-terminal parts (**Fig. 35A, B**). Phylogenetic tree construction of MAP55 and its homolog from different plant species categorizes this MAP family into the MAP55 clade, the MAP55L clade and the distant clade (**Fig. 35C**).

To identify MT binding regions, full-length and truncated versions of MAP55 and MAP55L proteins were fused to GFP, and were transiently expressed in onion epidermal cells, together with the red fluorescent MT marker tagRFP-MAP4. Dual color visualization of MAP55-GFP and tagRFP-MAP4 was difficult possibly because both proteins competed for common MT binding sites. Therefore, MT binding ability of MAP55-GFP was determined by the presence of fine filaments (presumably representing cortical MTs) decorated by MAP55-GFP. Overlapping of the GFP and RFP signals confirmed localization of full-length MAP55L on cortical MTs. N-terminal truncated regions of MAP55 and MAP55L showed no MT localization, whereas C-terminal fragments showed MT-localization. MT localization of C-terminal MAP55 fragments appeared to be moderate compared to that of C-terminal MAP55L fragments. These results demonstrate that more than one region at the C-terminal parts of MAP55 and MAP55L contribute to MT binding in vivo (**Fig. 36, 37**).

MT co-sedimentation assay

To test whether MAP55 family proteins can bind directly to MTs, MBP-MAP55 or MBP-MAP55L recombinant proteins were expressed in bacteria and highly purified by affinity purification with amylose resins. Some degradation products were observed in the final purification preparations. The principle of MT co-sedimentation is that MT-binding protein will precipitate together with MTs in the pellet fraction after ultracentrifugation. Protein that does not bind MTs will be separated in the supernatant fraction. As a negative control, MBP protein alone was also tested to verify that it does not bind MTs and remain in the supernatant fraction after ultracentrifugation. When 1 μ M of purified proteins were incubated with MTs assembled from bovine brain tubulins

and pelleted by ultracentrifugation, intact MBP-MAP55 and MBP-MAP55L, together with their degradation products showed efficient co-sedimentation with MTs in the pellet fraction (**Fig. 38B**). In the absence of MTs, the fusion proteins remained in the supernatant. This demonstrates that MAP55 and MAP55L bind to MTs directly.

Expression patterns

To investigate the spatial gene expression patterns in Arabidopsis plants, RT-PCR analysis was first conducted on cDNAs synthesized from total RNA isolated from different plant tissues (**Fig. 39A**). Both *MAP55* and *MAP55L* were constitutively expressed in whole vegetative tissues. However, while *MAP55* showed strong expression in buds, flowers and young developing siliques, *MAP55L* gave strong expression in buds only, but not in the other reproductive tissues.

Promoter-GUS analysis was carried out to examine the tissue-specific expression patterns of *MAP55L*. Since the 5'-upstream region of *MAP55* could not be cloned even after several attempts in my study, similar analysis was not done for *MAP55*. Since 2.5-kb promoter region of *MAP55L* fused to the GUS reporter gene did not give any detectable expression in transgenic Arabidopsis plants, a genomic fragment containing the 2.5-kb 5'-upstream regulatory region, intron, and the coding region was used to translationally express GUS inserted before the stop codon. Strong GUS staining was detected in the leaf and at the root meristem. The GUS staining pattern is consistent with the RT-PCR results, showing strong expression in all vegetative tissues, but not the reproductive organs (**Fig. 39B-K**).

Mutational studies

To understand in vivo functions of MAP55 and MAP55L, several T-DNA insertion lines were obtained from Salk Institute Genomic Analysis Laboratory. The T-DNA insertion was verified by PCR genome-typing using the primers flanking expected the insertion sites (**Fig. 40C**). Four independent *MAP55* alleles were obtained and were designated as *map55-1*, *map55-2*, *map55-3* and *map55-4* (**Fig. 40B**). The *map55-1* had T-DNA insertion at the seventh intron, which was before the last exon. The T-DNA insertion of *map55-2* was at the first exon whereas *map55-3* was at the seventh exon. The T-DNA insertion of *map55-4* was at the eighth exon. All these alleles only had partial cDNA, no full-length cDNA could be produced. Without the full-length cDNA,

these alleles might be null mutant or partial loss-of function alleles. The presence of MAP55 protein in the different alleles could not be determined using Western Blot due to the lack of MAP55 antibodies. Distinguishable phenotypic differences from wild-type plants were not detected for *map55-1*, *map55-2* and *map55-4* (**Fig. 40D**). *map55-3* plants showed slightly shorter siliques, but this possible phenotype was not complemented with overexpression of GFP-MAP55 (**Fig. 41**). One null MAP55L allele had a T-DNA insertion in the second and showed stunted growth and pale green leaves. These phenotypes were observed after backcrossing to wild type four times, but were not complemented with genomic MAP55L fragment fused with GFP (data not shown). I speculate that an unrelated linked mutation (or mutations) is responsible for the observed phenotypes. I also screened a Targeting Induced Local Lesions in Genomes (TILLING) mutant collections (C24 ecotype) established in the Takayama Lab (NAIST), but could not recover any loss-of-function alleles from this screening. Finally, the CRISPR/Cas9 system with a guide RNA (gRNA) targeting the first exon of *MAP55L* was used to generate *map55l* mutants (**Fig. 42A**). Several independent F1 mutant alleles were isolated and one deletion allele with no T-DNA insertion was successfully recovered in the F2 progeny. Molecular analyses with HaeIII digestion and with sequencing analysis revealed that this *map55l* is heterozygous (**Fig. 42C, D**). When homozygous *map55l* plants are recovered, it will be examined whether this *map55l* allele is a null allele, and what phenotypes it will exhibit. Double mutant of *map55* and *map55l* will be generated to see whether MAP55 and MAP55L function redundantly.

Subcellular localization

To examine detailed subcellular localization and dynamics *in vivo*, MAP55 and MAP55L were fused to GFP, and expressed under the constitutive cauliflower mosaic virus 35S promoter (MAP55) or under its own regulatory elements (MAP55L) in the Arabidopsis MT marker line expressing mCherry fluorescent protein fused to β -tubulin 6 (mCherry-TUB6). GFP-MAP55 and MAP55L-GFP showed strong overlapping localizations with mCherry-TUB6-labeled cortical MTs in the interphase root epidermal cells (**Fig. 43**). In dividing cells, both proteins decorated mitotic MT structures; preprophase bands (PPBs), spindles, and phragmoplasts (**Fig. 44**). MAP55 and MAP55L thus do not prefer particular MT structures, and appear to bind all MTs with similar affinities.

Time-lapse imaging by spinning confocal microscopy revealed that MAP55 and MAP55L tend to accumulate at the MT ends, and this end-labeling feature is more prominent for GFP-MAP55 than for MAP55L-GFP (**Fig. 45**). It is not known whether this difference is caused by intrinsic property of these proteins or by the location of the GFP-tag. Time-lapse montages and kymographs indicated that GFP-MAP55 accumulated the plus end during the growth phase. Dual-color observation of GFP-MAP55 and EB1b-mCherry as +TIP marker showed strong overlapping at the growing plus-end (**Fig. 45B, C, D**). The intensity of MAP55 suddenly decreased when the plus-end experienced catastrophe shift to shrinkage, but returned to label the end when it resumed to growth by the rescue event (**Fig. 45E, F**). To test this plus-end tracking behavior depends on well-known plant +TIPs, GFP-MAP55 was expressed in the *Arabidopsis spr1* mutant and in the *eb1a eb1b eb1c* triple mutant (**Fig. 46, 47**). GFP-MAP55 still retained the ability to track the growing plus-end without functions of SPR1 and EB1s, demonstrating that EB1 and SPR1 are not required for the end-tracking function of MAP55.

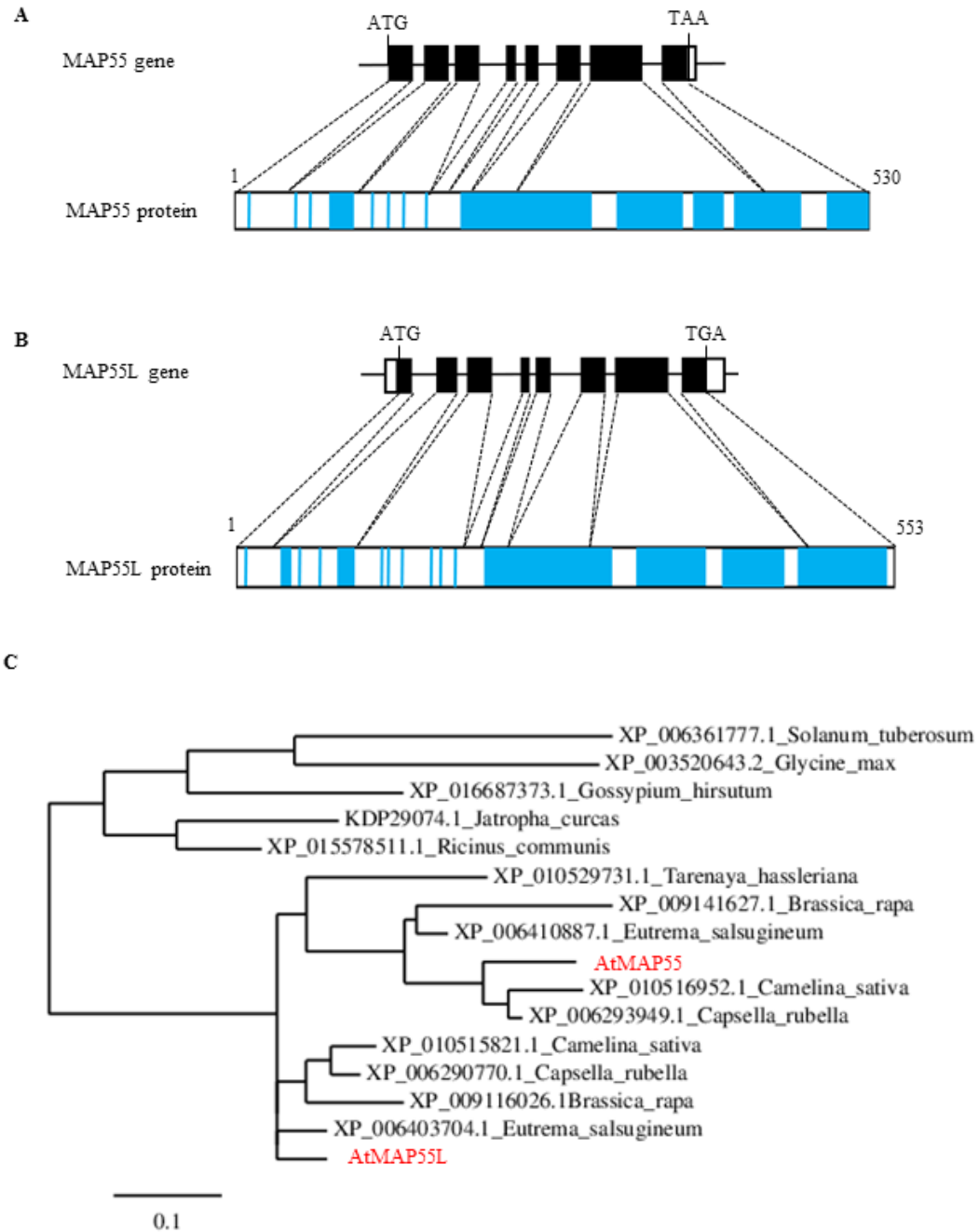


Fig. 35. Gene structure and phylogenetic relationships of MAP55 and its homologs

(A) Gene and protein structure of MAP55. Blue box indicates basic amino acid.

(B) Gene and protein structure of MAP55L. Blue box indicates basic amino acid.

(C) Phylogenetic tree of MAP55 and its homologs from different plant species.

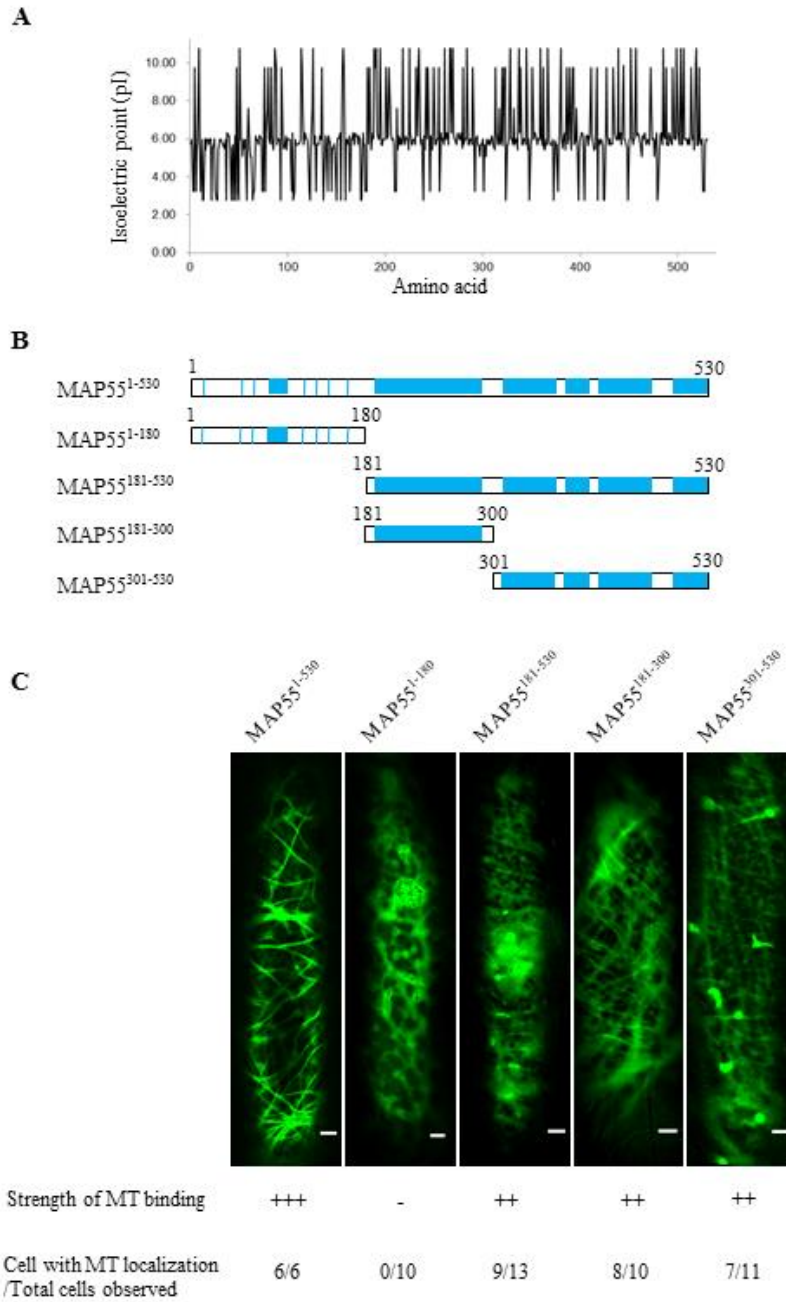


Fig. 36. MT-binding domain of MAP55

(A) Charge plot of MAP55 showing the isoelectric point (pI) of individual amino acid.

(B) Schematic diagram of full-length or truncated MAP55 with basic domains (blue color).

(C) Transient subcellular localization of different variants of MAP55-GFP in onion pavement cells.

Scale bar: 10 μ m.

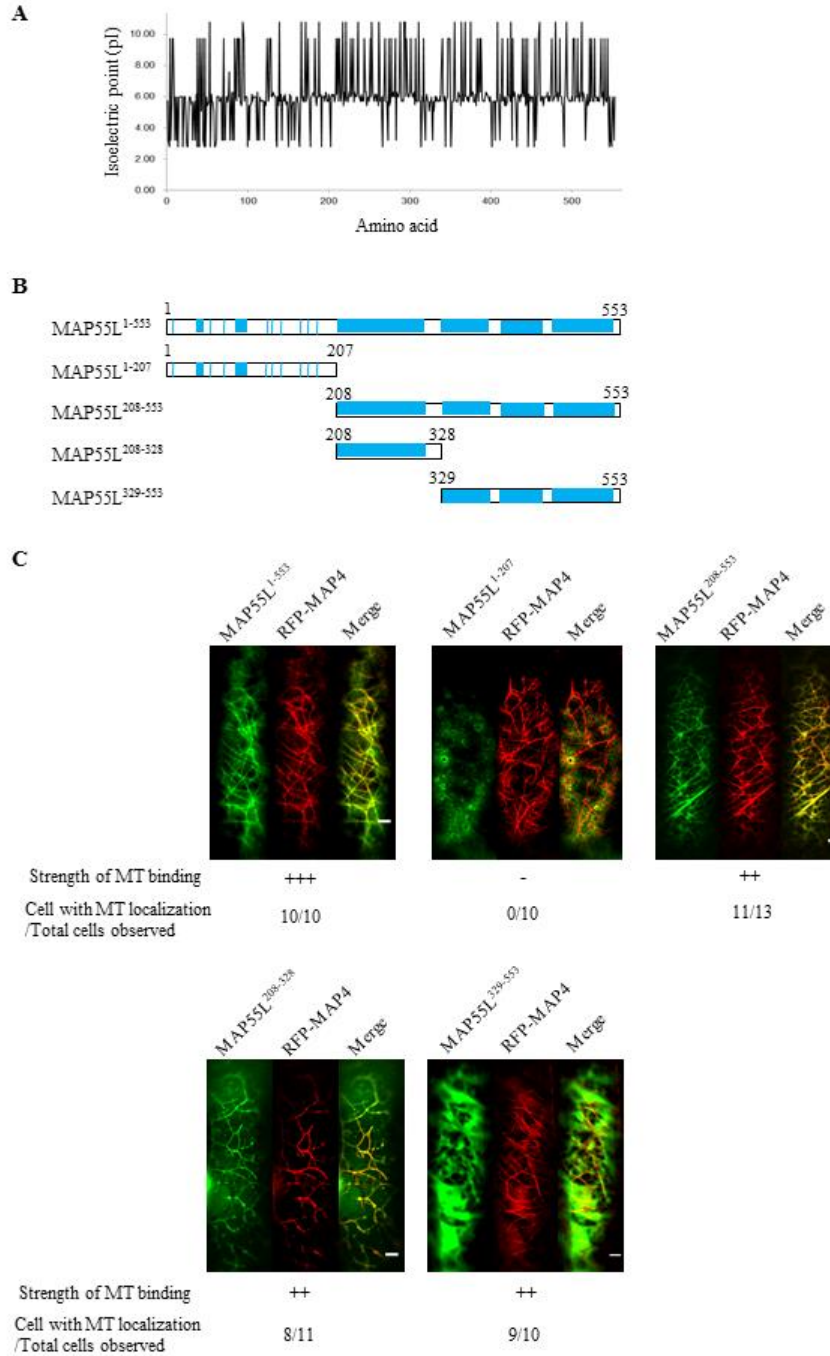


Fig. 37. MT-binding domain of MAP55L

(A) Charge plot of MAP55L showing the isoelectric point (pI) of individual amino acid.

(B) Schematic diagram of full-length or truncated MAP55L with basic domains (blue color).

(C) Transient subcellular co-localization of different variants of MAP55L-GFP with MT marker (RFP-MAP4) in onion pavement cells. Scale bar: 10 μ m

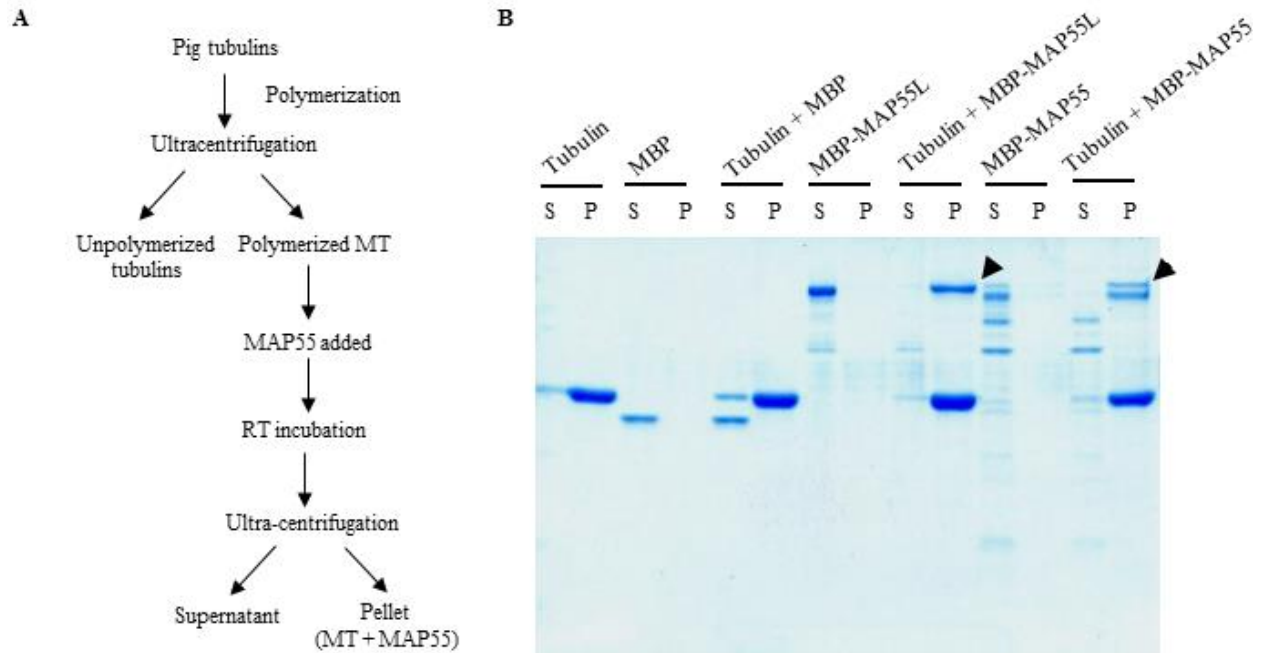


Fig. 38. MT co-sedimentation assay of MAP55 and MAP55L.

(A) Workflow of MT preparation and MT co-sedimentation of MAP55.

(B) Co-sedimentation of MBP, MBP-MAP55 and MBP-MAP55L with MTs respectively.

Arrowhead indicate band of MBP-MAP55 or MBP-MAP55L co-sediment together with MTs.

‘S’ indicates supernatant fraction whereas ‘P’ indicates pellet fraction.

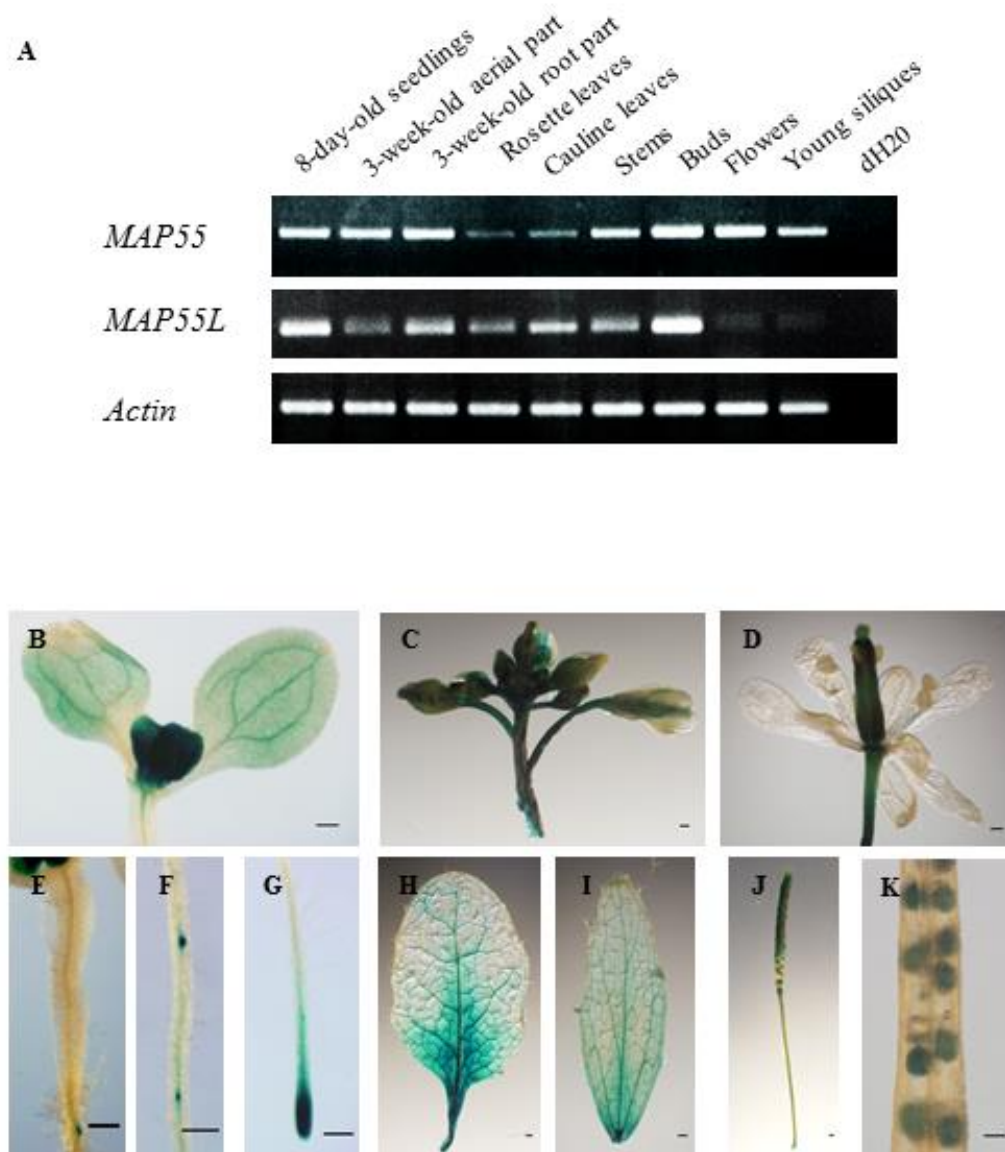


Fig. 39. Expression pattern studies

RT-PCR of *MAP55* and *MAP55L* cDNA in different WT tissues at specific developmental stages (A). *Actin* was used as control. Promoter-GUS staining of *MAP55L* in different tissues: 7-day-old cotyledons (B), buds (C), flower (D), hypocotyl (E), lateral root primordia (F), root tip (G), rosette leaf (H), cauline leaf (I), developing silique (J), seeds (K). Scale bar: 0.2 mm

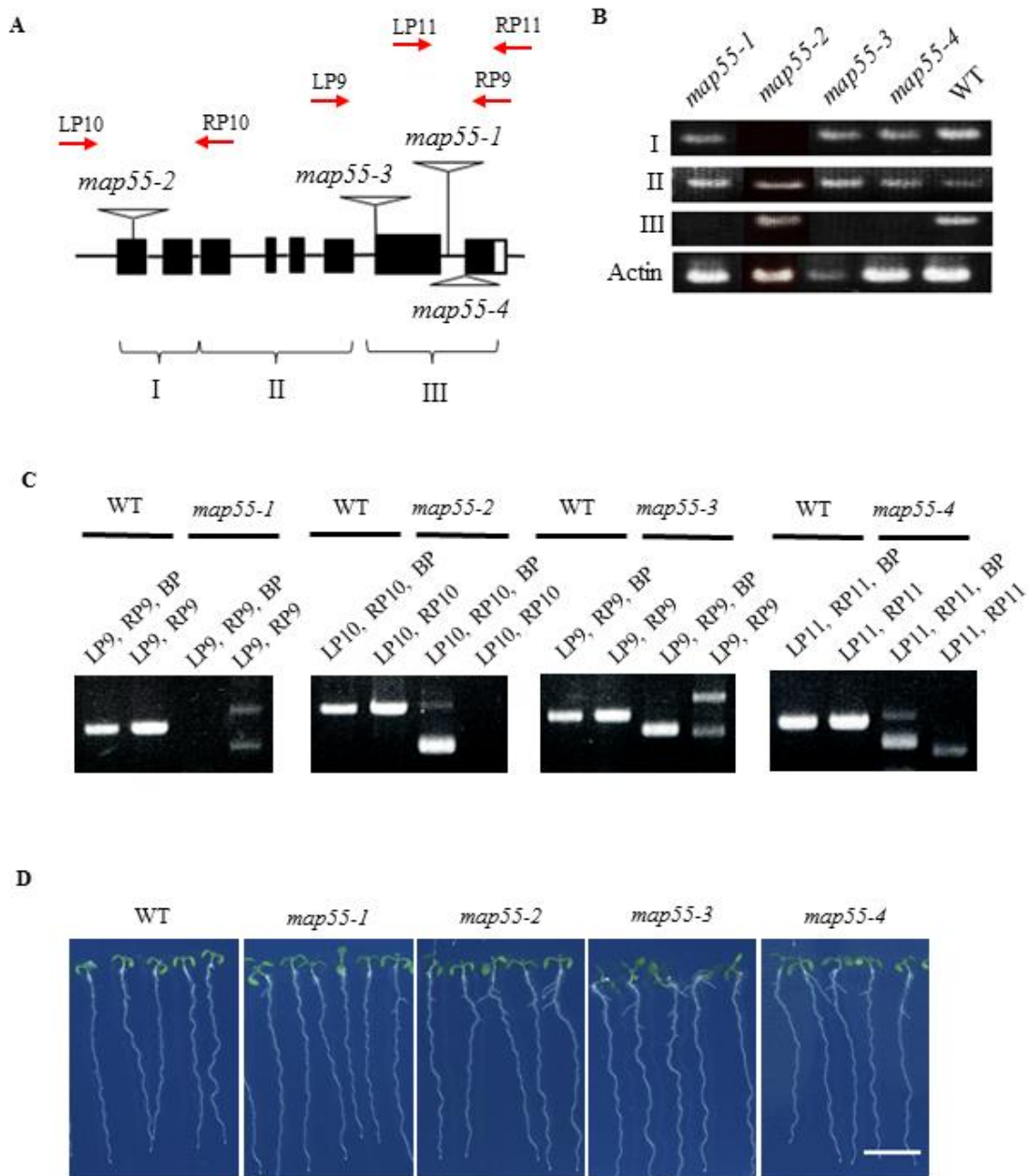


Fig. 40. T-DNA insertional allele screening of MAP55

- (A) Schematic diagram of T-DNA insertion in genomic MAP55.
- (B) RT-PCR of MAP55 cDNA from different T-DNA insertion mutants in (A).
- (C) PCR genome-typing of *map55* mutants using primer sets that flank each T-DNA site.
- (D) 7-day-old seedlings grown on Arabi media plate placed vertically. Scale bar: 1 cm.

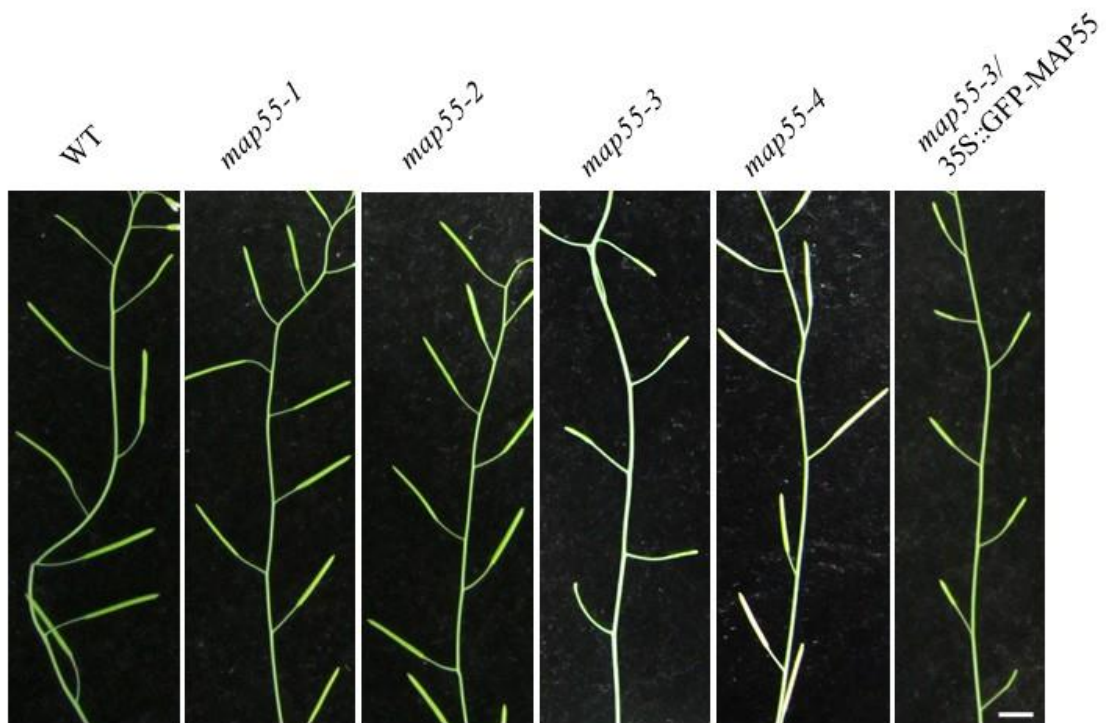


Fig. 41. Silique of *map55* mutants

The comparison of silique length between wild type and different *map55* mutants.

Complemented *map55-3* with 35S::GFP-MAP55 could not rescue the phenotype.

Scale bar: 1cm.

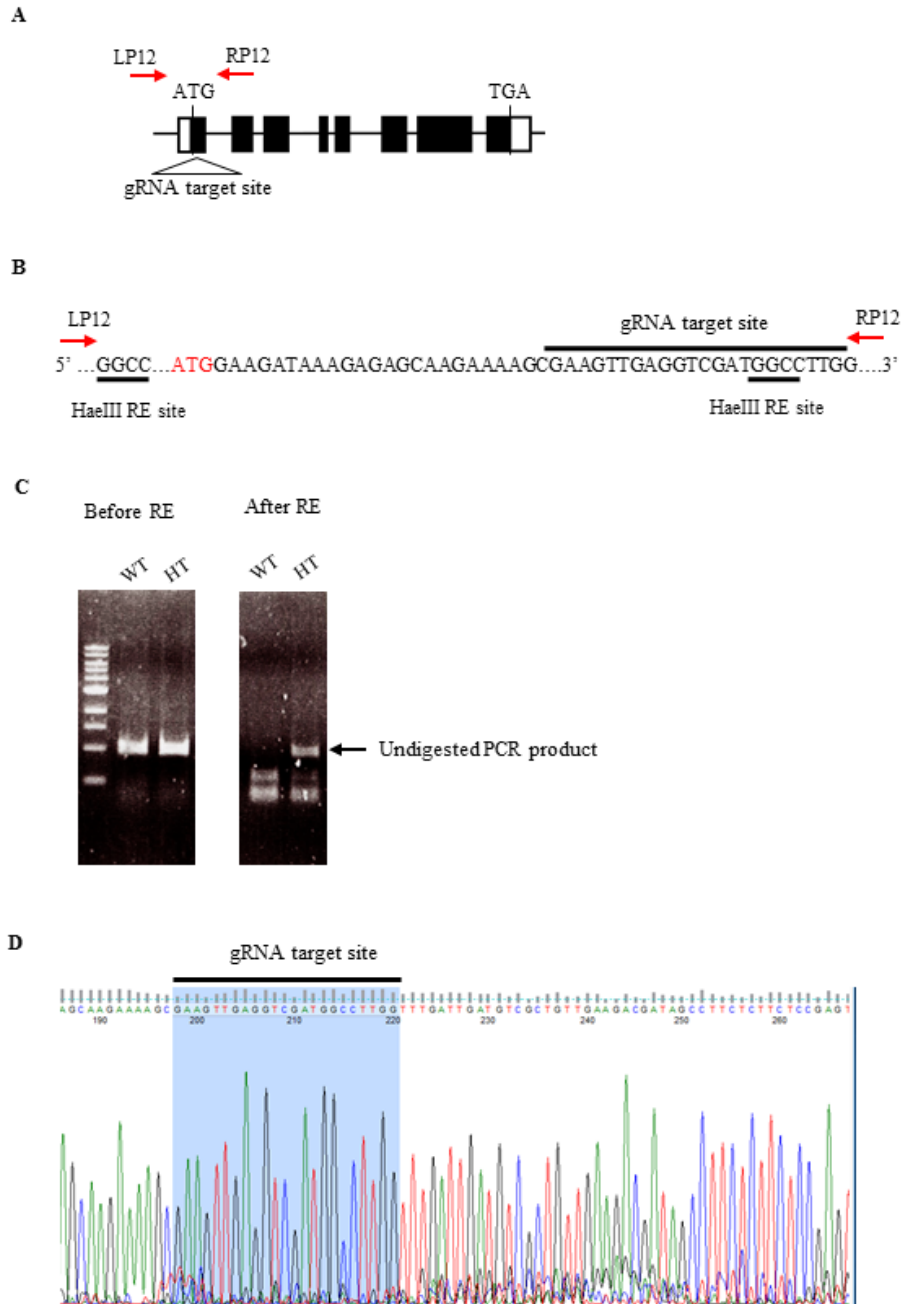


Fig. 42. Generation of CRISPR/Cas9-mediated *map55l* mutant

(A) Gene structure of MAP55L with gRNA target site.

(B) Location of HaeIII RE sites within PCR products of WT *MAP55L*.

(C) HaeIII RE analysis of PCR products amplified from F1 seedlings

(D) Sequencing analysis of heterozygous CRISPR-Cas9-mediated *map55l* mutant. Overlapping peaks appear after gRNA target site.

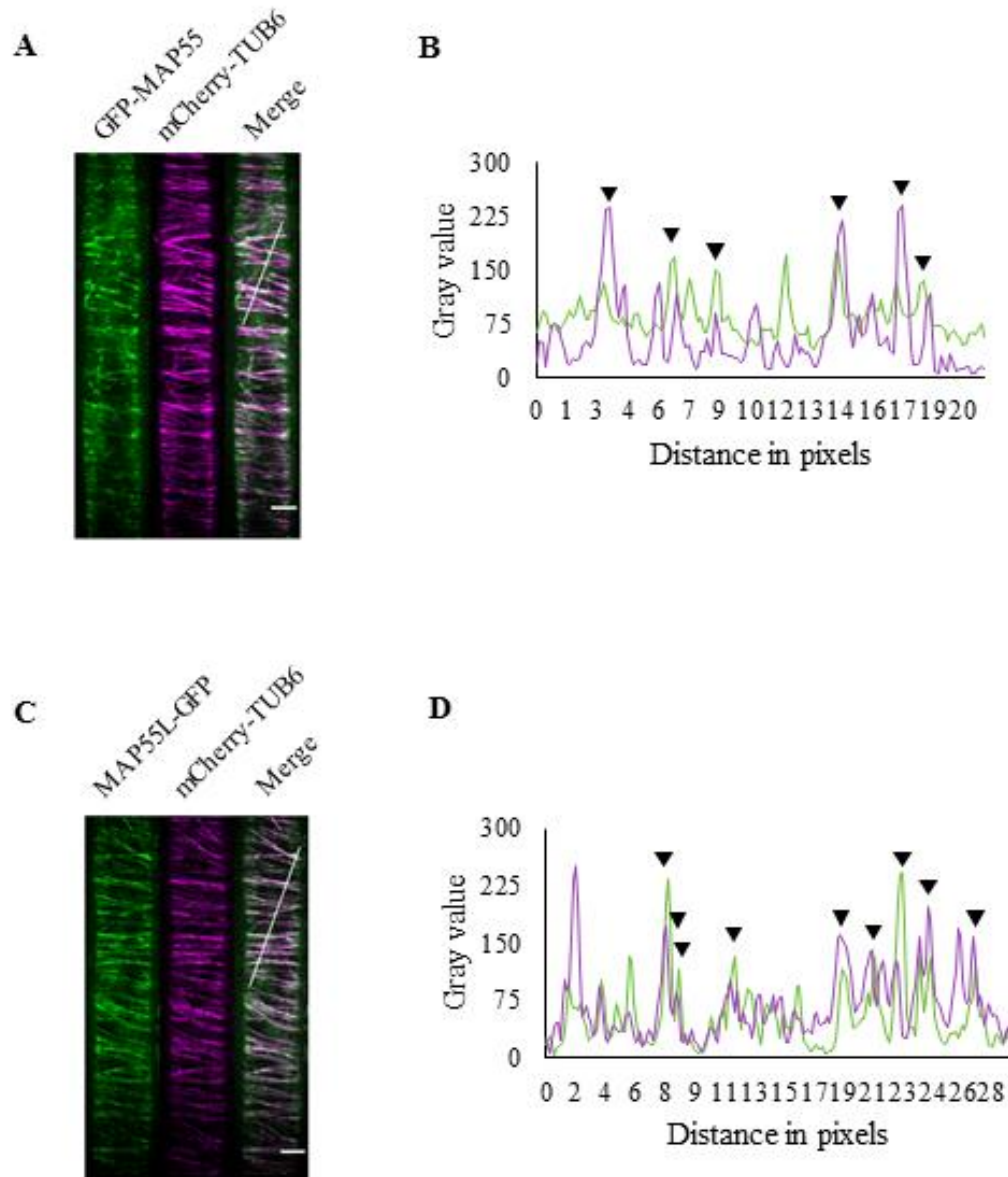


Fig. 43. Subcellular localization of GFP-MAP55 and MAP55L-GFP in interphase cells.

Confocal imaging of 35Spro::GFP-MAP55 (A) and own pro::MAP55L-GFP (C) in 8-day-old root epidermal cells. GFP-MAP55 (green color) co-localized with cortical MT labelled with mCherry-TUB6 (magenta color). Intensity plot of GFP-MAP55 (B) and MAP55L-GFP (D) based on the line drawn in (A) or (C) indicates overlapping peaks (arrowhead) of GFP-MAP55 or MAP55L-GFP (green line) and mCherry-TUB6 (magenta). Scale bar: 5 μ m.

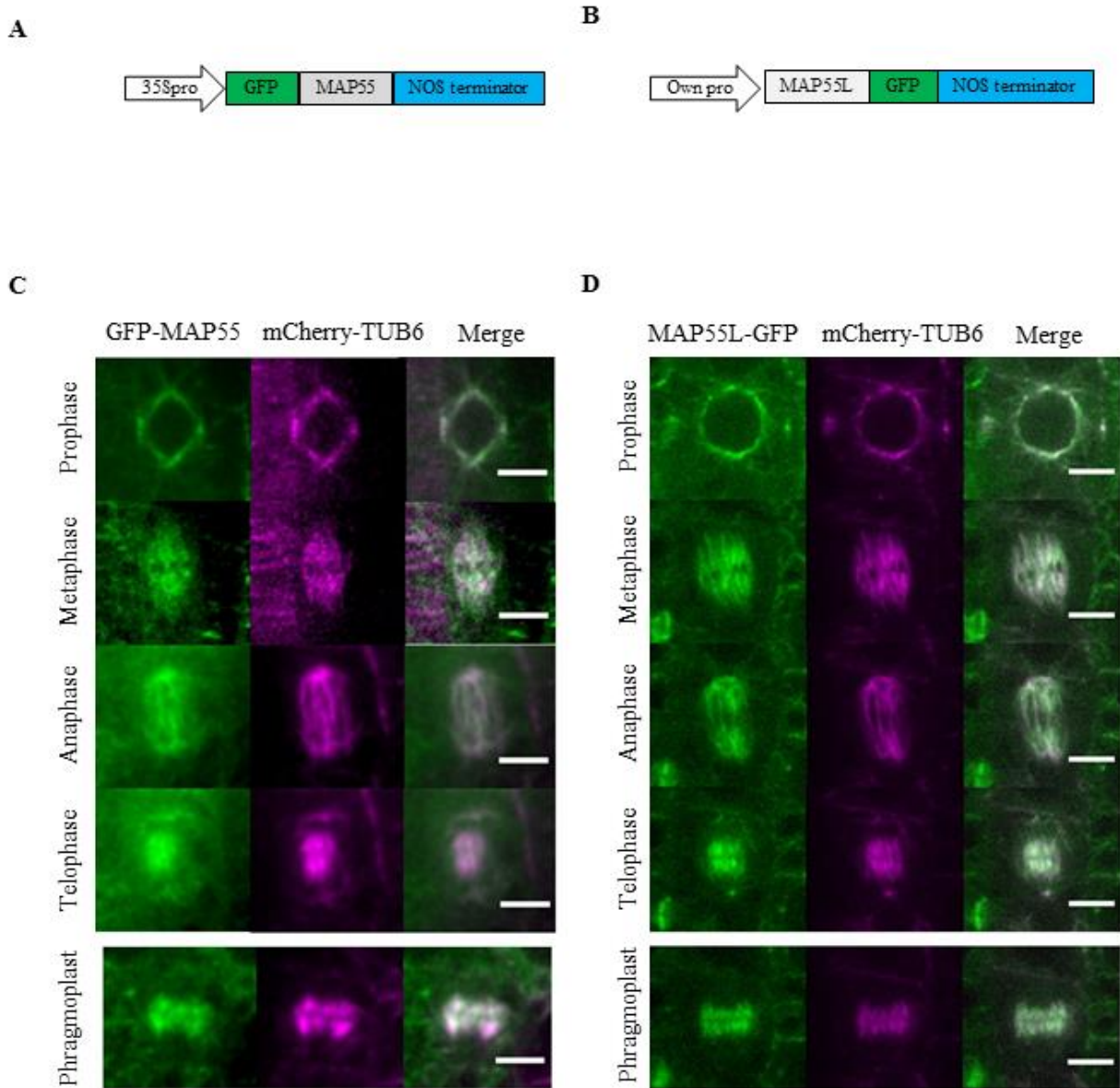


Fig. 44. Subcellular localization of GFP-MAP55 and MAP55L-GFP during mitotic division.

(A) Schematic diagram of GFP-MAP55 vector construction.

(B) Schematic diagram of MAP55L-GFP vector construction.

(C) Overexpression of GFP-MAP55 decorates spindle bundles in four different mitotic phases, including the plant specific phragmoplast structure. Scale bar: 5 μ m.

(D) Expression of own pro::gMAP55L-GFP decorates spindle bundles in each different mitotic phase. Scale bar: 5 μ m.

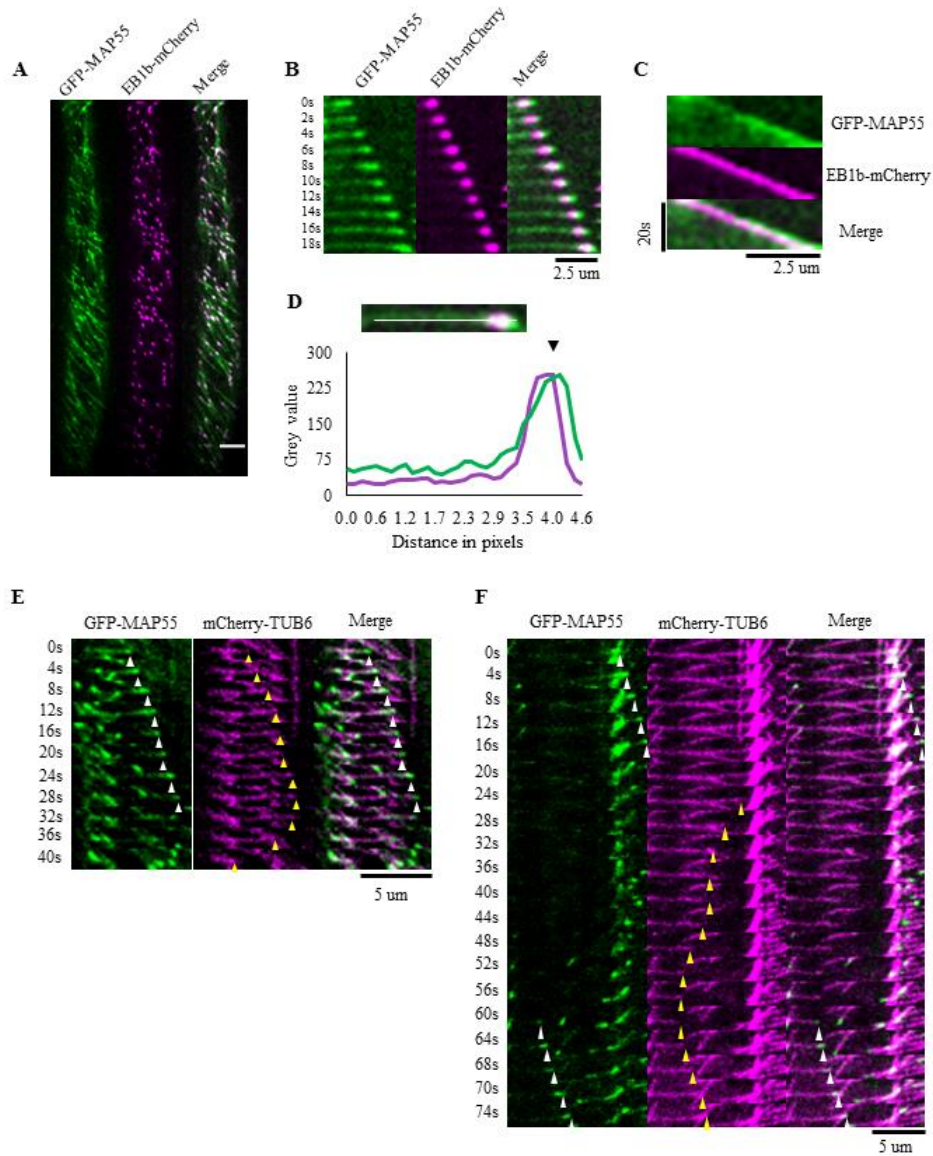


Fig. 45. MAP55 exhibits plus-end tracking behavior.

(A) Dual color visualization of GFP-MAP55 (green color) and EB1b-mCherry (magenta) in 8-day-old root epidermal cells. GFP-MAP55 tracks growing plus-end of cortical MTs. Scale bar: 5 μm.

(B) Montage of GFP-MAP55 and EB1b-mCherry during growth event.

(C) Kymograph of same particle in (B) during growth event.

(D) Intensity plot showing overlapping of GFP-MAP55 with EB1b-mCherry at growing plus-end.

(E) Montage of GFP-MAP55 and mCherry-TUB6 during catastrophe event of plus end.

(F) Montage of GFP-MAP55 and mCherry-TUB6 during rescue event of plus end.

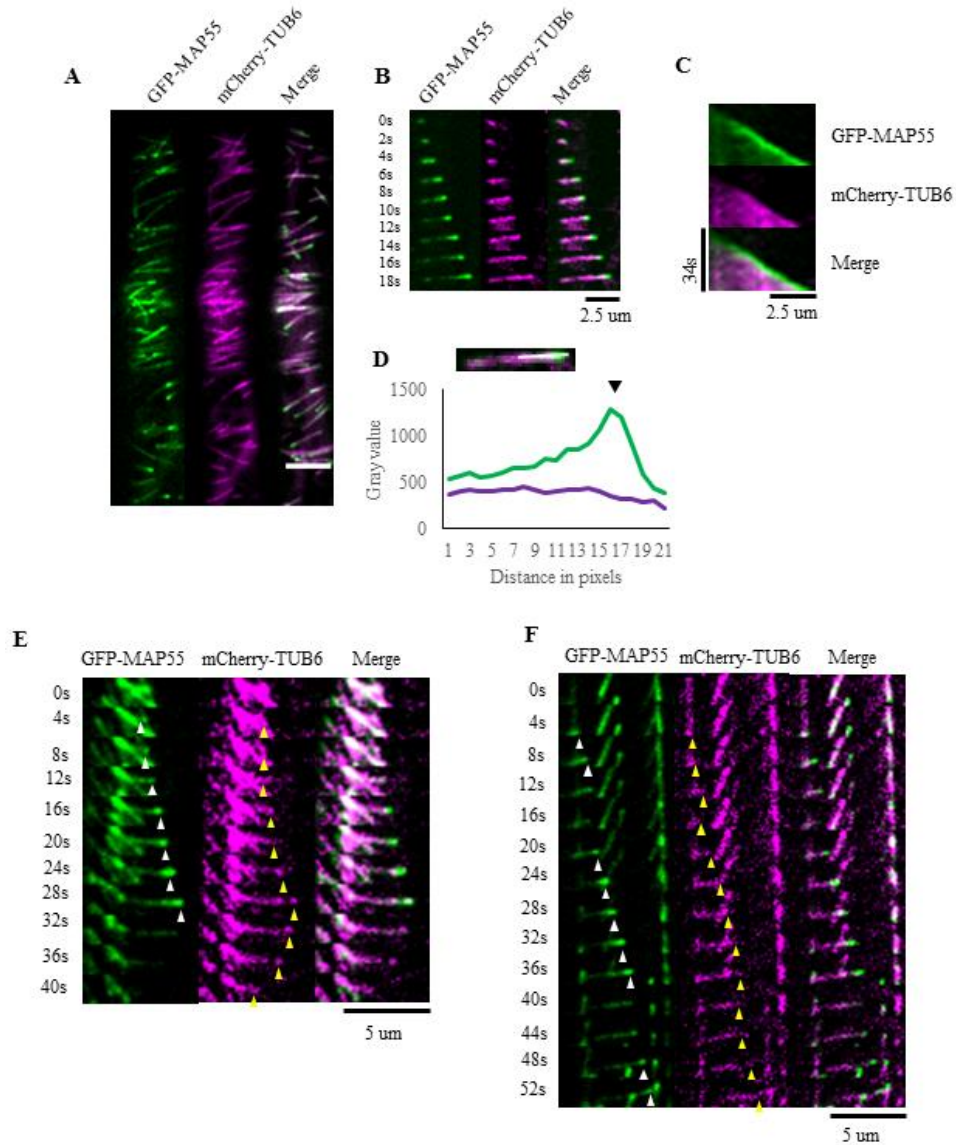


Fig. 46. MAP55 retains plus-end tracking behavior in *spr1-3* single mutant.

(A) Dual color visualization of GFP-MAP55 (green color) and mCherry-TUB6 (magenta) in 8-day-old root epidermal cells of *spr1-3* single mutant. GFP-MAP55 tracks growing plus-end of cortical MTs. Scale bar: 5 μm.

(B) Montage of GFP-MAP55 and mCherry-TUB6 during growth event.

(C) Kymograph of same particle in (B) during growth event.

(D) Intensity plot showing overlapping of GFP-MAP55 with mCherry-TUB6 at growing plus-end.

(E) Montage of GFP-MAP55 and mCherry-TUB6 during catastrophe event of plus end.

(F) Montage of GFP-MAP55 and mCherry-TUB6 during rescue event of plus end.

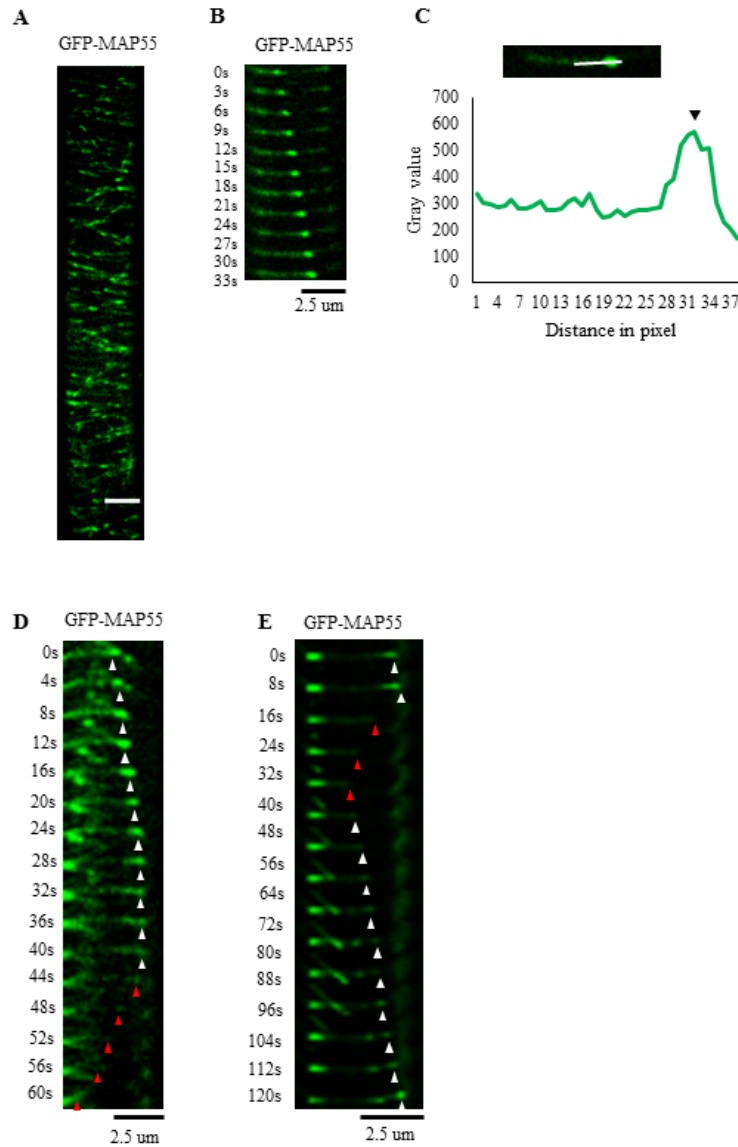


Fig. 47. MAP55 retains plus-end tracking behavior in *eb1a eb1b eb1c* triple mutant.

(A) Dual color visualization of GFP-MAP55 (green color) and mCherry-TUB6 (magenta) in 8-day-old root epidermal cells of *eb1a eb1b eb1c* triple mutant. GFP-MAP55 tracks growing plus-end of cortical MTs. Scale bar: 5 μ m.

(B) Montage of GFP-MAP55 and mCherry-TUB6 during growth event.

(C) Kymograph of same particle in (B) during growth event.

(D) Intensity plot showing overlapping of GFP-MAP55 with mCherry-TUB6 at growing plus-end.

(E) Montage of GFP-MAP55 and mCherry-TUB6 during catastrophe event of plus end.

(F) Montage of GFP-MAP55 and mCherry-TUB6 during rescue event of plus end.

Table 3. List of primers used in this study

Name	Sequence (5'-3')	Experiment
BP	CCCGTCTCACTGGTGAAAAG	Amplifying left-border of T-DNA
LP9	CCTAAATCATCTGGGGGTTAG	Genotyping of <i>map55-1</i> , <i>map55-3</i>
RP9	GCTTTGGTGAAGCCGAGAC	Genotyping of <i>map55-1</i> , <i>map55-3</i>
LP10	TCAACACCGGTCTAAAGAATGA	Genotyping of <i>map55-2</i>
RP10	AAGTCCTTACGCTTGTCAG	Genotyping of <i>map55-2</i>
LP11	CAAGATGACCCAAAGCCTTC	Genotyping of <i>map55-4</i>
RP11	TGCTGAAGAAAATTGGTGTGTT	Genotyping of <i>map55-4</i>
LP12	TGTGTTTGTGAAAAATAAGTCACG	Genotyping of <i>map55l</i>
RP12	TTCGTTCGAAATGAACTTACCA	Genotyping of <i>map55l</i>
MAP55L sgRNA_F	GTTGAGGTTCGATGGCCTGTTTTAGAGCTAGAAATAGCAAG	Mutagenesis of <i>MAP55L</i> gRNA
MAP55L sgRNA_R	GCCATCGACCTCAACTTCCAATCACTACTTCGACTCTAGC	Mutagenesis of <i>MAP55L</i> gRNA
MAP55_441	GCCGAGCTCGACGATATCAAT	RT-PCR of <i>MAP55</i> cDNA region I
MAP55_462	GCCCAAAGTCTCTTCATCACA	RT-PCR of <i>MAP55</i> cDNA region I
MAP55_485	CTAGCATGATGGGGAGGAAA	RT-PCR of <i>MAP55</i> cDNA region II
MAP55_486	GATGGCCTGTTGAGTCCAGT	RT-PCR of <i>MAP55</i> cDNA region II
MAP55_461	CAAGATGACCCAAAGCCTTC	RT-PCR of <i>MAP55</i> cDNA region III
MAP55_477	CAAGTTGTTCTCTGCACTG	RT-PCR of <i>MAP55</i> cDNA region III
MAP55_29F	GCGAGCTCGACGATATCAAT	RT-PCR of <i>MAP55</i> in expression pattern
MAP55_1209R	CCTCAGAGCTAGGGTCGTCT	RT-PCR of <i>MAP55</i> in expression pattern
MAP55L_373	CGGGATCCATGGAAGATAAAGAGAGCAAGAAAAG	RT-PCR of <i>MAP55L</i> in expression pattern
MAP55L_401	GGTCGGTAAAGCTTTCTTCC	RT-PCR of <i>MAP55L</i> in expression pattern

Table 3. (cont.)

Name	Sequence (5'-3')	Experiment
RTActin8F	ACATTGTGCTCAGTGGTGGT	RT-PCR of <i>Actin</i>
RTActin8R	CCTGGACCTGCTTCATCATA	RT-PCR of <i>Actin</i>
MAP55_For	CAAAAAAGCAGGCTTCATGGGAGAAGAGAAGGAGAAGCTGGA	Amplifying <i>MAP55</i> cDNA with half attB1 site
MAP55_Rev	CAAGAAAGCTGGGTCTCCAAGTTGTTCTCTGCACTGACT	Amplifying <i>MAP55</i> cDNA with half attB2 site
MAP55L_gene_F	CAAAAAAGCAGGCTTCATCTTGAAGTGTTAATGGTATTTG	Amplifying <i>MAP55L</i> gene with half attB1 site
MAP55L_gene_R	CAAGAAAGCTGGGTCTCCCTCAAGTTGATCTTCTGCATCG	Amplifying <i>MAP55L</i> gene with half attB2 site
attB1 adapter	GGGGACAAGTTTGTACAAAAAAGCAGGCT	Amplifying attB1 site
attB2 adapter	GGGGACCACTTTGTACAAGAAAGCTGGGT	Amplifying attB2 site
EcoRI_MAP55_F	GGCGAATTCATGGGAGAAGAGAAGGAGAAGCTGG	Amplifying <i>MAP55</i> cDNA with restriction site
MAP55_PstI_R	GCCCTGCAGTTATCCAAGTTGTTCTCTGCACT	Amplifying <i>MAP55</i> cDNA with restriction site
BamHI_MAP55L_F	GGCGGATCCATGGAAGATAAAGAGAGCAAGAAA	Amplifying <i>MAP55L</i> cDNA with restriction site
MAP55L_PstI_R	GCCCTGCAGTCATCCCTCAAGTTGATCTTCTGC	Amplifying <i>MAP55L</i> cDNA with restriction site

Discussion

In this study, MAP55 and its homolog MAP55L were found to be expressed in most tissues of different developmental stages. These proteins decorate cortical MTs in the interphase and mitotic MTs. They bind MTs directly as demonstrated by the *in vitro* MT co-sedimentation assay. Both MAP55 and MAP55L contain multiple MT-binding regions dispersed at the middle and C-terminal parts, which are characterized by high incidence of basic amino acids. Basic domains are often conserved in MAPs and potentially interact with acidic C-terminal tails of plant tubulins (Hamada *et al.*, 2013). Given the high similarity of protein sequences and expression patterns, MAP55 and MAP55L may be functionally redundant. Generation of *map55 map55l* double knockout mutants may be necessary to reveal their potential functions for plant development and physiology.

Interestingly, MAP55 exhibited growing plus-end tracking behavior. This defines MAP55 as a novel plant +TIP. EB1 is a conserved +TIP that recognizes the geometry of the GTP cap, and autonomously tracks the growing MT plus-end. In animal cells, EB1 recruits interacting MAPs to the growing ends and form plus-end protein complexes that regulate plus-end interactions with various cellular targets (Vaugh, 2005). Although Arabidopsis EB1 was proposed to interact with SPR1 (Galva *et al.*, 2015), it is not known whether plant EB1 and SPR1 have intrinsic properties to recognize and track the growing plus end. MAP55 still retains its plus-end tracking ability in absence of EB1 or SPR1, suggesting it does not require these known +TIP proteins to track the end. MAP55 and MAP55L do not contain the Ser-x-Ile-Pro (SxIP) motif shared by numerous animal +TIPs for interaction with EB1 (Honnappa *et al.*, 2009). *In vitro* tip tracking assay using recombinant MAP55 and total internal reflection fluorescence microscopy (TIRF) is required to demonstrate that the MAP55 autonomously tracks the growing plus end by itself. My attempt to purify sufficient amount of GFP-tagged MAP55 failed so far. Although physiological functions of MAP55 and MAP55L are unknown, they represent a unique class of plus-end tracking plant MAPs, whose biochemical characterization is anticipated.

Conclusion

The BPP family is important for the regulation of anisotropic cell growth that subsequently gives the proper organ architecture. Particularly, BPP1 and BPP5 are essential for generating the complex cell shapes of cotyledon pavement cells through the local organization of cortical MT without affecting the total MT density. The BPP-dependent radiating and transverse MT array are required for the convex lobe formation leading to the inter-digitated cell shape. These plant-specific MAPs are by far the most important in the lobe formation among the reported lobe regulators, and will be useful in connecting the local sensor and the signal amplifier involving ROPs and their RIC effectors to regional activation of MT regulators.

MAP55 and its homolog directly bind MTs, and track the MT plus ends *in vivo*. This +TIP behavior does not require EB1 and SPR1, known plant +TIP proteins. Thus, MAP55 might recognize the plus-end region of growing MTs autonomously, or might be recruited to the growing end by a piggy-back mechanism on unknown +TIPs. Physiological or morphological functions of MAP55 and MAP55L need to be investigated in their double mutants.

Acknowledgement

First and foremost, I would like to take this opportunity to express my gratitude to my academic advisor Prof. Takashi Hashimoto for the continuous support of my Ph.D study and related research. His patience, motivation and sharing of his immense scientific knowledge have greatly a debt that I owe him forever. His consistent guidance in research and my thesis writing have helped me a lot. I could not have imagined having a better advisor and mentor for my Ph.D study.

Besides my advisor, I would also like to thank the rest of my supervisory committee: Prof. Seiji Takayama and Prof. Masaaki Umeda, for showing their interest in my work. They have given me their insightful comments and encouragement in pursuing Ph.D degree. They also had constantly voiced their critical questions regarding my work, which incited me to widen my research from various perspectives.

Every result described in this thesis was accomplished with the assistance and support of fellow labmates and collaborators. Associate Prof. Tsubasa Shoji had assisted me during my initial work of transiently expressing fusion proteins in *Nicotiana benthamiana*. Assistant Prof. Takehide Kato had worked together with me in early stage of my Ph.D, teaching me efficient way of expressing transgenic in Arabidopsis and genome typing method of screening different kind of mutants. Special Assistant Prof. Takashi Hotta had taught me all the fundamental knowledge and technical skills in expression and purification of recombinant fusion protein in either plant or bacterial cultures. I also had gained a lot of skills involving *in vitro* MT assays with his guidance. He is an extremely reliable source of biochemical and proteomic knowledge.

My work could not have been completed without the scientific assistance provided by Project Assistant Prof. Takumi Higaki from Hasezawa Group in Tokyo University. His image processing expertise had helped the characterization of abnormal pavement cell shape and MT distribution. Another collaborator is Dr. Hirofumi Nakagami, the unit leader in RIKEN for the identification of phosphorylated amino acid in PHS1 during my initial work.

Ex-members such as Dr. Satoshi Fujita had been a great senior in guiding me throughout my initial PHS1 project and teaching me the immunoblotting technique. His scrutinized questions have helped shape me into a critical thinking researcher. Dr. Noriyoshi Yagi had taught me the

principles and hands on operation of spinning disc confocal microscope. He had also shared his knowledge on microscopic image processing, which helped to interpret most of my scientific data presented in this thesis. Dr. Nahoko Nagasaki-Takeuchi had helped me in getting used to the working environment in NAIST, and also demonstrating some of the shared equipment in the common rooms.

I would like to thank various members of the Nakajima Group with whom I had the opportunity to share my scientific opinions with: Prof. Keiji Nakajima, Assistant Prof. Shunsuke Miyashima, Dr. Kaori Furuta and Dr. Tetsuya Hisanaga. They kindly shared their Nikon D-ECLIPSE C2 confocal microscope with me for the visualization of fluorescence tagged MT and MAPs. They provided a friendly and cooperative atmosphere for me and also insightful comments on my work. I would be remiss if I did not thank Mrs. Satomi Yamashita who deserves credit for providing much needed assistance with administrative tasks, reminding me of impending deadlines, and keeping our work running smoothly.

I am grateful for the funding source that allowed me to pursue my graduate studies: Japanese Government (Monbukagakusho: MEXT) Scholarship for Research Student. This scholarship had enabled me to concentrate on my doctoral project for four years without the concern of financial statement.

Last but not least, I would like to acknowledge friends and family who supported me spiritually throughout my doctoral study and my life in general.

Wong Jeh Haur

References

- Akhmanova, A., and Steinmetz, M.O. (2008). Tracking the ends: a dynamic network controls the fate of microtubule tips. *Nat. Rev. Mol. Cell Biol.* 9: 309-322
- Alushin, G.M., Lander, G.C., Kellogg, E.H., Zhang, R., Baker, D., and Nogales, E. (2014). High-resolution microtubule structures reveal the structural transitions in $\alpha\beta$ -tubulin upon GTP hydrolysis. *Cell* 157: 1117-1129
- Ambrose, C., Allard, J.F., Cytrynbaum, E.N., and Wasteneys, G.O. (2011). A CLASP-modulated cell edge barrier mechanism drives cell-wide cortical microtubule organization in Arabidopsis. *Nat. Commun.* 2: 430
- Ambrose, J.C., Shoji, T., Kotzer, A.M., Pighin, J.A., and Wasteneys, G.O. (2007). The Arabidopsis CLASP gene encodes a microtubule-associated protein involved in cell expansion and division. *Plant Cell* 19: 2763-2775
- Armour, W.J., Barton, D.A., Law, A.M.K., and Overall, R.L. (2015). Differential growth in periclinal and anticlinal walls during lobe formation in Arabidopsis cotyledon pavement cells. *Plant Cell* 27: 2484-2500
- Baskin, T.I. (2001). On the alignment of cellulose microfibrils by cortical microtubules: a review and model. *Protoplasma* 215: 150-171
- Baskin, T.I., Meekes, H.T.H.M., Liang, B.M., and Sharp, R.E. (1999). Regulation of growth anisotropy in well-watered and water-stressed maize roots. II. Role of cortical microtubules and cellulose microfibrils. *Plant Physiol.* 119: 681-692
- Burk, D.H., Liu, B., Zhng, R., Morrison, W.H., and Ye, Z. (2001). A katanin-like protein regulates normal cell wall biosynthesis and cell elongation. *Plant Cell* 13: 807-827
- Chang-Jie, J., and Sonobe, S. (1993). Identification and preliminary characterization of a 65 kDa higher-plant microtubule-associated protein. *J. Cell Sci.* 105: 891-901

- Clough, S.J., and Bent, A.F. (1998). Floral dip: a simplified method for *Agrobacterium*-mediated transformation of *Arabidopsis thaliana*. *Plant J.* 16: 735-743
- Daga, R.R., Lee, K.G., Bratman, S., Salas-Pino, S., and Chang, F. (2006). Self-organization of microtubule bundles in anucleate fission yeast cells. *Nat. Cell Biol.* 8: 1108-1113
- Duelberg, C., Fourniol, F.J., Maurer, S.P., Roostalu, J., and Surrey, T. (2013). End-binding proteins and Ase1/PRC1 define local functionality of structurally distinct parts of the microtubule cytoskeleton. *Trends Cell Biol.* 23: 54-63
- Ehrhardt, D.W. (2008). Straighten up and fly right: Microtubule dynamics and organization of non-centrosomal arrays in higher plants. *Curr. Opin. Cell Biol.* 20: 107-116
- Fu, Y., Gu, Y., Zheng, A., Wasteneys, G., and Yang, Z. (2005). *Arabidopsis* interdigitating cell growth requires two antagonistic pathways with opposing action on cell morphogenesis. *Cell* 120: 687-700
- Fu, Y., Li, H., and Yang, Z. (2002). The ROP2 GTPase controls the formation of cortical fine F-actin and the early phase of directional cell expansion during *Arabidopsis* organogenesis. *Plant Cell* 14: 777-794
- Fu, Y., Xu, T., Zhu, L., Wen, M., and Yang, Z. (2009). A ROP GTPase signaling pathway controls cortical microtubule ordering and cell expansion in *Arabidopsis*. *Curr. Biol.* 19: 1827-1832
- Galva, C., Kirik, V., Lindeboom, J.J., Kaloriti, D., Rancour, D.M., Hussey, P.J., Bednarek, S.Y., Ehrhardt, D.W., and Sedbrook, J.C. (2014). The microtubule plus-end tracking proteins SPR1 and EB1b interact to maintain polar cell elongation and directional organ growth in *Arabidopsis*. *Plant Cell* 26: 4409-4425
- Gao, Y., Zhang, Y., Zhang, D., Dai, X., Estelle, M., and Zhao, Y. (2015). Auxin binding protein 1 (ABP1) is not required for either auxin signaling or *Arabidopsis* development. *Roc. Natl. Acad. Sci. USA* 112: 2275-2280
- Gardiner, J., and Marc, J. (2011). *Arabidopsis thaliana*, a plant model organism for the neuronal microtubule cytoskeleton? *J. Exp. Bot.*, 62: 89-97

Gardiner, J., and Overall, R., and Marc, J. (2012). Distant plant homologues: don't throw out the baby. *Trends Plant Sci.* 17: 126-128

Guerriero, G., Hausman, J., Cai, G. (2014). No stress! Relax! Mechanisms governing growth and shape in plant cells. *Int. J. Mol. Sci.* 15: 5094-5114

Hamada, T., Igarashi, H., Yao, M., Hashimoto, T., Shimmen, T., Sonobe, S. (2006). Purification and characterization of plant dynamin from tobacco BY-2 cells. *Plant Cell Physiol.* 47: 1175-1181

Hamada, T., Nagasaki-Takeuchi, N., Kato, T., Fujiwara, M., Sonobe, S., Fukao, Y., and Hashimoto, T. (2013). Purification and characterization of novel microtubule-associated proteins from *Arabidopsis* cell suspension cultures. *Plant Physiol.* 163: 1804-1816

Hashimoto, T. (2003). Dynamics and regulation of plant interphase microtubules: a comparative review. *Curr. Opin. Plant Biol.* 6: 568-576

Hashimoto, T. (2015). Microtubules in plants. *The Arabidopsis Book* 13: e0179. doi: 10.1199/tab.0179

Hayashi, K., and Kojima, C. (2010). Efficient protein purification method for NMR using soluble protein tags with cold shock expression vector. *J. Biomol. NMR* 48: 147-155

Ho, C.M., Hotta, T., Guo, F., Roberson, R.W., Lee, Y.R., and Liu, B. (2011). Interaction of antiparallel microtubules in the phragmoplast is mediated by the microtubule-associated protein MAP65-3 in *Arabidopsis*. *Plant Cell* 23: 2909-2923

Honnappa, S., Gouveia, S.M., Weisbrich, A., Damberger, F.F., Bhavesh, N.S., Jawhari, H., Grigoriev, I., van Rijssel, F.J., Buey, R.M., Lawera, A., Jelesarov, I., Winkler, F.K., Wüthrich, K., Akhmanova, A., and Steinmetz, M.O. (2009). An EB1-binding motif acts as a microtubule tip localization signal. *Cell* 138: 366-376

Ishida, T., Kaneko, Y., Iwano, M., Hashimoto, T. (2007). Helical microtubule arrays in a collection of twisting tubulin mutants of *Arabidopsis thaliana*. *Proc. Natl. Acad. Sci. USA* 104: 8544-8549

Jefferson, R.A., Kavanagh, T.A., and Bevan, M.W. (1987). GUS fusion: β -glucuronidase as a sensitive and versatile gene fusion marker in higher plants. *EMBO J.* 6: 3901-3907

- Jiang, K., Toedt, G., Gouveia, S.M. Davey, N.E., Hua, S., van der Vaart, B., Grigoriev, I., Larsen, J., Pedersen, L.B., Bezstarosti, K., Lince-Faria, M., Dmmers, J., Steinmetz, M.O., Gibson, T.J., and Akhmanova, A. (2012). A proteome-wide screen for mammalian SxIP motif-containing microtubule plus-end tracking proteins. *Curr. Biol.* 22: 1800-1807
- Kim, G.-T., Shoda, K., Tsuge, T., Cho, K.-H., Uchimiya, H., Yokoyama, R., Nishitani, K., and Tsukaya, H. (2002). The *ANGUSTIFOLIA* GENE of *Arabidopsis*, a plant *CtBP* gene, regulates leaf-cell expansion, the arrangement of cortical microtubules in leaf cells and expression of a gene involved in cell-wall formation. *EMBO J.* 21: 1267-1279
- Komaki, S., Abe, T., Coutuer, S., Inzé, D., Russinova, E., and Hashimoto, T. (2009). Nuclear-localized subtype of end-binding 1 protein regulates spindle organization in *Arabidopsis*. *J. Cell Sci.* 123: 451-459
- Kumar, P., and Wittman, T. (2012). +TIPs: SxIPping along microtubule ends. *Trends Cell Biol.* 22: 418-428
- Ledbetter, M.C., and Porter, K.R. (1963). A “microtubule” in plant cell fine structure. *J. Cell Biol.* 19: 239-250
- Lin, D., Cao, L., Zhou, Z., Zhu, L., Ehrhardt, D., Yang, Z., and Fu, Y. (2013). Rho GTPase signaling activates microtubule severing to promote microtubule ordering in *Arabidopsis*. *Curr. Biol.* 23: 290-297
- Lloyd, C., and Hussey, P. (2001). Microtubule-associated proteins in plants: why we need a MAP. *Nat. Rev. Mol. Cell Biol.* 2: 40-47
- Lucas, J.R., Courtney, S., Hassfurder, M., Dhingra, S., Bryant, A., and Shaw, S.L. (2011). Microtubule-associated proteins MAP65-1 and MAP65-2 positively regulate axial cell growth in etiolated *Arabidopsis* hypocotyls. *Plant Cell* 23: 1889-1903
- Maurer, S.P. Fourniol, F.J., Bohner, G., Moores, C.A., Surrey, T. (2012). EBs recognize a nucleotide-dependent structural cap at growing microtubule ends. *Cell* 149:371-382

- Mitchison, T., and Kirschner, M. (1984). Dynamic instability of microtubule growth. *Nature* 312: 237-242
- Nakajima, K., Furutani, I., Tachimoto, H., Matsubara, H., and Hashimoto, T. (2004). *SPIRAL1* encodes a plant-specific microtubule-associated protein required for directional control of rapidly expanding *Arabidopsis* cells. *Plant Cell* 16: 1178-1190
- Nakajima, K., Kawamura, T., and Hashimoto, T. (2006). Role of the *SPIRAL1* gene family in anisotropic growth of *Arabidopsis thaliana*. *Plant Cell Physiol.* 47: 513-522
- Nakamura, M., Ehrhardt, D.W., and Hashimoto, T. (2010). Microtubule and katanin-dependent dynamics of microtubule nucleation complexes in the acentrosomal *Arabidopsis* cortical array. *Nat. Cell Biol.* 12: 1064-1070
- Nakamura, M., Naoi, K., Shoji, T., and Hashimoto, T. (2004). Low concentrations of propyzamide and oryzalin alter microtubule dynamics in *Arabidopsis* epidermal cells. *Plant Cell Physiol.* 45: 1330-1334
- Nogales, E., Wolf, S.G., and Downing, K.H. (1998). Structure of the $\alpha\beta$ -tubulin dimer by electron crystallography. *Nature* 391: 199-203
- Okada, K., and Shimura, Y. (1992). Mutational analysis of gravitropism and phototropism of *Arabidopsis thaliana* seedlings. *Functional Plant Biol.* 19: 439-448
- Panteris, E., and Galatis, B. (2005). The morphogenesis of lobed plant cells in the mesophyll and epidermis: Organization and distinct roles of cortical microtubules and actin filaments. *New Phytol.* 167: 721-732
- Sedbrook, J.C., Ehrhardt, d.W., Fisher, S.E., Scheible, W.R., and Somerville, C.R. (2004). The *Arabidopsis* *sku6/spiral1* gene encodes a plus end-localized microtubule-interacting protein involved in directional cell expansion. *Plant Cell* 16: 1506-1520
- Shaw, S.L., Kamyar, R., and Ehrhardt, D.W. (2003). Sustained microtubule treadmilling in *Arabidopsis* cortical arrays. *Science* 300: 1715-1718

Vaughan, K.T. (2005). TIP marker and TIP marker: EB1 as a master controller of microtubule plus ends. *J. Cell Biol.* 171: 197-200

Vineyard, L., Elliot, A., Dhingra, S., Lucas, J.R., and Shaw, S.L. (2013). Progressive transverse microtubule array organization in hormone-induced *Arabidopsis* hypocotyl cells. *Plant Cell* 25: 662-676

Wang, X., Zhu, L., Liu, B., Wang, C., Jin, L., Zhao, Q., and Yuan, M. (2007). Arabidopsis MICROTUBULE-ASSOCIATED PROTEIN18 functions in directional cell growth by destabilizing cortical microtubule. *Plant Cell* 19: 877-889

Wasteneys, G.O. (2002). Microtubule organization in the green kingdom: Chaos or self-order? *J. Cell Sci.* 115, 1345-1354

Whittington, A.T., Vugrek, O., Wei, K.J., Hasenbein, N.G., Sugimoto, K., Rashbrooke, M.C., and Wasteneys, O. (2001). MOR1 is essential for organizing cortical microtubules in plants. *Nature* 411: 610-613

Wu, G., Gu, Y., Li, S., and Yang, Z. (2001). A genome-wide analysis of Arabidopsis Rop-interactive CRIB motif-containing proteins that act as Rop GTPase targets. *Plant Cell* 13: 2841-2856

Young, D.H., and Lewandowski, V.T. (2000). Covalent binding of the benzamide RH-4032 to tubulin in suspension-cultured tobacco cells and its application in a cell-based competitive-binding assay. *Plant Physiol.* 124: 115-124